The background of the entire page is a complex, abstract fractal pattern in shades of blue. It consists of numerous fine, interconnected lines and shapes that resemble a dense, organic network or a highly detailed, swirling pattern. The colors range from deep navy blue to lighter, almost cyan tones, creating a sense of depth and movement. The overall effect is that of a turbulent, fluid-like structure, which directly relates to the title text.

**Efficiently generated  
turbulence  
for an  
increased  
flame speed**

**A.A. Verbeek**



# Efficiently generated turbulence for an increased flame speed

A.A. Verbeek

Samenstelling van de promotiecommissie:

*Voorzitter:*

Prof. dr. G.P.M.R. Dewulf                      Universiteit Twente

*1<sup>ste</sup> Promotor:*

Prof. dr. ir. T.H. van der Meer              Universiteit Twente

*2<sup>de</sup> Promotor:*

Prof. dr. ir. B.J. Geurts                      Universiteit Twente

*Leden:*

Prof. dr. D. Lohse                              Universiteit Twente

Prof. dr. ir. G. Brem                          Universiteit Twente

Dr. ir. R.J.M. Bastiaans                      Technische Universiteit Eindhoven

Prof. dr. H.B. Levinsky                      Rijksuniversiteit Groningen

Prof. dr. ir. B.J. Boersma                      Technische Universiteit Delft


## UNIVERSITY OF TWENTE.

Faculty of Engineering Technology  
Laboratory of Thermal Engineering

The research in this thesis was supported by the Dutch Technology Foundation (STW) and was part of the MoST project within the Clean Combustion Concepts program (Project nr. 10425).



Copyright © 2014 A.A. Verbeek

This thesis was typeset using L<sup>A</sup>T<sub>E</sub>X and  LyX  
Cover image was generated using Apophysis 2.09

Printed by Ipskamp Drukkers, Enschede



ISBN 978-90-365-3716-2

DOI 10.3990/1.9789036537162



# EFFICIENTLY GENERATED TURBULENCE FOR AN INCREASED FLAME SPEED

## PROEFSCHRIFT

ter verkrijging van  
de graad van doctor aan de Universiteit Twente,  
op gezag van de rector magnificus,  
prof. dr. H. Brinksma  
volgens besluit van het College voor Promoties  
in het openbaar te verdedigen  
op woensdag 1 oktober 2014 om 14:45 uur

door

Antonie Alex Verbeek

geboren op 12 juni 1985  
te Zutphen

Dit proefschrift is goedgekeurd door:

Prof. dr. ir. T.H. van der Meer	1 <sup>ste</sup> promotor
Prof. dr. ir. B.J. Geurts	2 <sup>de</sup> promotor

# Summary

The rate of combustion in premixed flames is to a large extent controlled by the level of turbulence. Fluctuations in the flow field deform the flame front that exists between the premixed reactants and the fully combusted products. The surface area of this flame front is increased as it becomes more wrinkled by the turbulent flow, which increases the turbulent flame speed.

In this thesis two different methods to generate turbulence in an efficient way are studied. This turbulence is used to increase the flame speed of a low-swirl burner. In turn, this increases its power density and makes it more suitable for gas turbine application. The term efficient can be interpreted two-fold. The turbulence can either be increased at specific scales beneficial for the generation of flame surface. Or, alternatively, the turbulence can be intensified over the whole range of turbulence scales, but at a less than proportional increase of the energy input.

The first approach adopts an active grid that is composed of a stationary and a rotating disk with characteristic hole patterns. Upon rotation it forms a time-dependent arrangement of pulsating jets. By changing the set of disks and the rotational frequency a wide variety of flow-forcing is possible. Hot-wire measurements performed in the flow downstream of the active grid show an energy spectrum with distinct and controllable peaks. The response, defined as the amount of energy contained in these peaks, is high (up to 25%) when the introduced perturbations have a timescale in the energy-containing range and decreases when these timescales are shorter and lie in the inertial range. However, there is no frequency identified for the current design and parameter range where the turbulent kinetic energy or the dissipation rate is maximized. The effect on the low-swirl flame is characterized by means of OH-LIF. The variation in turbulent flame speed, measured by the amount of flame surface, is of the same order as the measurement uncertainty. Therefore, it cannot be concluded that the specific fluctuations introduced by the active grid are directly causing additional wrinkling of the flame front. The amount of energy in these specific scales is too low to induce a significant change in the combustion rate.

In the second approach so-called fractal grids are used to generate turbulence. These grids are obtained by truncating a self-similar fractal pattern at some level of refinement. A parametric study of fractal-grid-generated turbulence containing 24 different grids with variation in grid patterns, solidity and range of embedded scales was conducted. This identifies the parameters of the fractal grid that affect the level of turbulence and the turbulent flame speed. Here, a rod-stabilized, V-shaped flame is used as such stabilization mechanism allows for considerable more variation in upstream fractal grid geometry compared to low-swirl stabilization. The fractal grids provide much more intense turbulence compared to classical grids and therefore

an increased turbulent flame speed. By increasing the range of embedded scales the turbulence is intensified. With respect to the reference case of a classical grid the turbulence intensity can be more than quadrupled while for the turbulent flame speed more than a doubling is observed. From the energy spectrum of the velocity it becomes clear that not only the largest scales are more energetic; also smaller scales are introduced as the spectrum is further extended into the high-frequency range.

When the standard blockage grid in a low-swirl burner is replaced by fractal grids a similar increase in turbulence and combustion rate is observed as for a V-shaped flame. The turbulence is intensified when comparing the flow behind the multi-scale grid to the reference situation. This increase is expressed by more than doubling of the r.m.s. of the velocity fluctuations, while only marginal changes in pressure drop are observed. The OH-LIF experiments show an increase in flame surface density and widening of the flame brush as well as much finer wrinkling of the flame front for the cases involving a multi-scale blocking grid. The grid parameters that were varied are the range of embedded scales and the blockage ratio. The fact that the range of embedded scales mainly controls the turbulence intensity and the blockage ratio the low-swirl stabilization, engineering fractal grids for low-swirl combustion can be done with relative ease. In addition to the effect on the turbulent flame speed, it has also been verified that the low  $\text{NO}_x$  emission levels, a key feature of low-swirl burners, are not affected when using fractal grids.

This thesis presents a clear affirmative answer to the question whether it is possible to increase the turbulent flame speed of a low-swirl flame by efficiently generated turbulence. It is shown that with fractal grids it is possible to elevate the turbulence intensity significantly and, moreover, that these grids are a feasible option for implementation in real low-swirl burners. The active grid approach is considered to be of limited value for combustion applications as it does not introduce sufficient additional perturbations at the right scales.

# Samenvatting

De verbrandingssnelheid van voorgemengde vlammen wordt voor een groot deel bepaald door het turbulentieniveau. Fluctuaties in het stromingveld vervormen het vlamfront dat zich bevindt tussen enerzijds het mengsel van brandstof en lucht en anderzijds de volledige verbrandde productgassen. Het totale oppervlakte van het vlamfront wordt verhoogd doordat het meer opgevouwen wordt door de turbulentie. Dit heeft tot gevolg dat de vlamsnelheid toeneemt.

In dit proefschrift worden twee verschillende methoden bestudeerd om op een efficiënte manier turbulentie in een stroming aan te brengen. Deze turbulentie wordt gebruikt om de vlamsnelheid van een zogeheten ‘low-swirl’ brander te verhogen. De toepasbaarheid van deze brander in gasturbines kan daarmee worden vergroot. De term efficiënt kan hier op twee manieren worden uitgelegd. Enerzijds kan de turbulentie worden verhevigd door alleen specifieke schalen te introduceren die gunstig zijn voor het creëren van meer vlamfront. Anderzijds kan de turbulentie geïntensiveerd worden over het gehele bereik aan turbulentieschalen, zei het voor een minder dan proportionele toename in benodigde energie.

De eerste methode maakt gebruik van een actief rooster dat bestaat uit een stationaire en een roterende schijf met karakteristieke gatenpatronen. Tijdens rotatie wordt een tijdsafhankelijke matrix van pulserende jets gevormd. Door verschillende gatenpatronen te gebruiken kan een scala aan verschillende stromingsexcitaties gerealiseerd worden. Hot-wire metingen, die zijn uitgevoerd stroomafwaarts van het actieve rooster, laten een energiespectrum zien met duidelijke, controleerbare pieken. De respons gedefinieerd als de hoeveelheid energie in deze pieken, is hoog (tot maximaal 25%) wanneer de geïntroduceerde verstoringen een tijdschaal hebben die in de ‘energy containing range’ ligt. Als de tijdschaal korter wordt en in de ‘inertial range’ ligt neemt de respons af. Er is echter geen aandrijffrequentie vastgesteld voor het huidige ontwerp en het gebruikte parameterbereik waarbij de turbulente kinetische energie of de dissipatiesnelheid maximaal is. Het effect op de low-swirl vlam is gekarakteriseerd door middel van OH-LIF metingen. De variatie in turbulente vlamsnelheid, berekend op basis van de hoeveelheid waargenomen vlamoppervlak, is van dezelfde orde grootte als de meetonauwkeurigheid. Er kan daarom niet geconcludeerd worden dat de specifieke verstoringen, aangebracht door het actieve rooster, extra vervorming van het vlamoppervlak veroorzaken. De hoeveelheid energie in deze specifieke schalen is te laag om een significante verandering van de verbrandingssnelheid te bewerkstelligen.

Voor de tweede methode worden zogeheten fractale roosters gebruikt om turbulentie op te wekken. Een fractaal rooster wordt verkregen door een eindig aantal iteraties te gebruiken van een zelfgelijkend patroon. Een parameterstudie is uitgevoerd bestaande uit 24 verschillende roosters met variatie in fractaal patroon, doorlaatbaar-



heid en het bereik aan lengteschalen om te bepalen welke parameters effect hebben op de turbulentie en de turbulente vlamsnelheid. Er is gebruik gemaakt van een draadgestabiliseerde V-vlam aangezien een dergelijk stabilisatiemethode meer variatie in fractale roosters toelaat vergeleken met low-swirl stabilisatie. Stroomafwaarts van de fractale roosters wordt een veel heviger turbulentie gemeten dan achter klassieke roosters. Dit leidt direct tot een toename in vlamsnelheid. Een groter bereik aan lengteschalen in een fractaal rooster resulteert in een toename in turbulentie. Vergeleken met de referentiesituatie waar een klassiek rooster wordt gebruikt, kan de intensiteit van de turbulentie verviervoudigd worden. Voor de turbulente vlamsnelheid werd een verdubbeling waargenomen. Uit het energiespectrum van het snelheidssignaal valt af te leiden dat niet alleen de grootste schalen meer energie bevatten; er worden ook kleinere schalen geïntroduceerd aangezien het spectrum zich verder uitstrekt in het hoogfrequente gebied.

Wanneer het standaard rooster uit een low-swirl brander wordt vervangen door een fractaal rooster wordt een vergelijkbare toename in turbulentie en verbrandingsnelheid waargenomen als voor de V-vlam. De turbulentie is heviger stroomafwaarts van de low-swirl brander met fractale roosters dan wanneer een standaard rooster gebruikt wordt. Dit uit zich in een meer dan verdubbeling van de standaardafwijking van snelheidsfluctuaties, terwijl de drukval nauwelijks beïnvloed wordt. De OH-LIF experimenten laten een verhoging van de vlamdichtheid zien evenals een verwijding van de vlam. Dit gaat gepaard met fijnere lokale structuren van het vlamfront. Het feit dat het bereik aan lengteschalen in het fractale rooster voornamelijk de toename in turbulentie bepaald en de doorlaatbaarheid voornamelijk het low-swirl stabilisatiemechanisme, maakt het ontwerpen van fractale roosters voor low-swirl verbranding relatief eenvoudig. Naast het effect op turbulentie en vlamsnelheid is ook gekeken naar het effect op  $\text{NO}_x$  emissies. Er is aangetoond dat het lage emissieniveau, dat kenmerkend is voor low-swirl verbranding, niet beïnvloed wordt door het toepassen van fractale roosters.

In dit proefschrift is een duidelijk bevestigend antwoord gegeven op de vraag of het mogelijk is om de turbulente vlamsnelheid te verhogen met efficiënt gegenereerde turbulentie. Er is laten zien dat met fractale roosters een sterke toename in turbulentie mogelijk is en dat bovendien deze roosters een goed uitvoerbare optie vormen voor implementatie in echte low-swirl branders. Het actieve rooster wordt van beperkte waarde geacht voor verbrandingsdoeleinden aangezien er niet voldoende extra verstoringen van de juiste schaal worden geïntroduceerd.

# Contents

<b>1</b>	<b>Introduction</b>	<b>1</b>
<b>2</b>	<b>A compact active grid</b>	<b>7</b>
2.1	Introduction . . . . .	7
2.2	Compact active grid based on a rotating disk . . . . .	9
2.3	Construction of active grid and experimental set up . . . . .	13
2.4	Turbulence behind the active grid . . . . .	15
2.5	Application in premixed combustion . . . . .	28
2.6	Conclusion . . . . .	40
<b>3</b>	<b>Fractal grids and premixed combustion</b>	<b>43</b>
3.1	Introduction in fractal-grid-generated turbulence . . . . .	43
3.2	Measuring turbulent flame speed of a V-shaped flame . . . . .	47
3.3	Fractal-grid patterns . . . . .	52
3.4	Flow response to fractal-grid-generated turbulence . . . . .	55
3.5	Flame response to fractal-grid-generated turbulence . . . . .	62
3.6	Conclusions . . . . .	67
<b>4</b>	<b>Fractal grids enhancing low-swirl combustion</b>	<b>69</b>
4.1	Introduction . . . . .	70
4.2	Fractal grid suitable for low-swirl burner . . . . .	71
4.3	Turbulent pipe flow with fractal perturbation . . . . .	75
4.4	Combustion enhancement due to fractal perturbations . . . . .	84
4.5	Conclusions . . . . .	96
<b>5</b>	<b>Conclusions</b>	<b>99</b>
5.1	Methods to efficiently generate turbulence . . . . .	99
5.2	Enhancement of the turbulent flame speed . . . . .	101
5.3	Outlook . . . . .	103
	<b>Bibliography</b>	<b>104</b>
	<b>Acknowledgement</b>	<b>113</b>
	<b>Curriculum vitae</b>	<b>115</b>



# Chapter 1

## Introduction

The combustion of various fuels in gas turbines is an important way of generating heat and power. These installations are responsible for a major part of the global energy conversion and therefore it is essential that the combustion process inside is as environmentally friendly as possible. Especially the clean combustion of natural gas requires attention since this forms an attractive energy source with a number of environmental benefits over other fossil fuels, such as lower emissions of  $\text{CO}_2$ ,  $\text{NO}_x$  and particulates [1].

A very effective method to decrease  $\text{NO}_x$  emissions in gas turbines, as well as in other combustion applications, is to operate in the lean premixed regime. Although this way of combustion is hampered by issues of flame stabilization, the excess of air results in relatively low flame temperature which reduces the  $\text{NO}_x$  emissions dramatically. The flame stabilization issues have traditionally been solved by the high-swirl concept, where the premixed fresh gases enter the combustion chamber with a swirling motion. This strong swirling motion results in a toroidal shaped recirculation zone that transports hot products back to the inlet where it continuously ignites the fresh mixture.  $\text{NO}_x$  emissions have been reduced by a factor of ten, compared to older non-premixed flames, when this concept was introduced in the 70's [26]. However, it is possible to reduce  $\text{NO}_x$  emissions further by stepping away from the high-swirl concept. The relatively high residence time caused by the recirculation in high-swirl burners is responsible for the remaining  $\text{NO}_x$  formation. A more recent and promising development is low-swirl stabilization, which is based on flow divergence instead of recirculation, resulting in a further reduction of  $\text{NO}_x$  emissions by 60% [40].

The diverging flow field is constructed by a vane swirler with a central passage, like depicted in Figure 1.1. The swirling annular flow and the central axial flow are balanced by a grid with a certain porosity to control the amount of swirl of the combined flow. When the flow emerges from the burner the swirl creates an outward motion, though the central axial flow is preventing the formation of a recirculation zone. In the diverging flow the axial velocity is decreasing and with a proper design conditions can be created such that in a certain region the turbulent flame speed equals the local flow velocity. It is this region where the flame can stabilize, resulting in a distinct bowl shaped lifted flame as shown in Figure 1.2.

While the low-swirl concept provides low  $\text{NO}_x$  emissions, the mixing near the flame is limited resulting in limited flame surface area and therefore a limited conversion



**Figure 1.1:** Schematic cross section of a low-swirl burner. The diverging flow field is illustrated by the streamlines at the burner exit.

rate. As this conversion rate or turbulent flame speed can be increased by adding more turbulent fluctuations [40], methods to efficiently create turbulence are pursued in this study. Here, the term efficient can be interpreted two-fold. The turbulence can be intensified over the whole range of turbulence scales at a less-than-proportional increase of the energy input. Or alternatively, only energy can be invested to create primarily very specific turbulence scales that are beneficial for the generation of flame surface. For example, the more energetic scales with a lengthscale in the order of the integral lengthscale wrinkle the flame more effectively compared to smallest scales that are rapidly dissipated, especially in the vicinity of the flame surface [27].

The low-swirl burner was originally designed as a research tool to examine the interaction between turbulence and premixed flames [5]. The combustion takes place in mid-air and the wrinkling of the central part of the flame is mainly dictated by the upstream turbulence, rather than by the swirling motion and shear with the stagnant ambient air. Hence, it could be considered as a freely propagating flame, which makes the low-swirl burner ideal to study the effect of turbulence on the combustion rate of premixed flames.





**Figure 1.2:** Photograph of a typical low-swirl flame. The inner tube diameter is 44 mm and the mean axial velocity is 8.4 m/s. As fuel Dutch natural gas is used at a thermal power of 33 kW. The photograph is taken using a shutter time of 1/100 s.

## Methods for efficient turbulence

**Modulated turbulence** A turbulent flow can contain more turbulent kinetic energy for a similar energy input rate when the energy is supplied at a specific (length and time) scale. Various numerical and experimental studies have been performed on this, so called, modulated turbulence [12, 15, 48, 49]. Of particular interest is the work of Cardoso de Souza [14], who investigated numerically the effect of modulating the kinetic energy input at the inflow plane of a premixed Bunsen burner setup. His results show that the burning rate is increased, as quantified in terms of an increased total flame surface wrinkling and a decreased average flame height, when the flow is forced at scales close to the integral length- and timescale. Cardoso de Souza used a forcing scheme inside a transversal plane, like a grid in a wind-tunnel, and unlike other numerical studies where a forcing inside a three-dimensional volume is applied [48, 49]. His results are qualitatively quite comparable to those obtained by using a volumetric forcing concerning at which scales the maximum response is obtained. Therefore, these results provide perspective to apply such forcing in real-life com-

bustion applications. It is, however, not trivial how a forcing scheme as applied by Cardoso de Souza should physically be obtained.

Several forcing strategies to introduce specific length- and timescales can be thought of. One example is an active grid as introduced by Makita [66]. Such a grid consists of horizontal and vertical rotating bars with flaps attached to it. By controlling each bar individually a rich variety of forcing patterns can be realized, including a large-scale modulated forcing as demonstrated in a wind-tunnel by Cekli et al. [15]. A different approach could be the use of synthetic jets, which are cavities with an oscillating diaphragm that produce a pulsating jet without a net mass flux [31]. Typical applications of these devices are found in flow control along surfaces. By adapting the size and operating frequency of the synthetic jet a wide range in length- and timescales may be introduced. A third example to obtain a specific forcing is to use a modulated movement of the boundary. This is demonstrated by Cadot et al. [12] who use a ‘French washing machine’, i.e., a closed cylindrical volume with counter-rotating disks at the top and bottom [12, 84]. When the rotational speed of the disks is modulated at a frequency close to the inverse of the integral timescale of the turbulence it was observed that the flow contained more turbulent kinetic energy while the same amount of energy was dissipated as in the unmodulated case.

**Fractal-grid-generated turbulence** Opposed to the time-dependent forcing strategy as described above, a static approach to elevate the turbulence levels is the use of a fractal-like object that excites the flow at different scales simultaneously. In this context a fractal-like object is obtained by truncating a self-similar pattern, such that it contains identical geometrical structures at different lengthscales. Hurst and Vassilicos [38] reported significantly higher turbulence levels downstream fractal grids, generated from three different patterns, compared to downstream classical single-scale grids. A more than doubling of the r.m.s. of the velocity fluctuations was measured during wind-tunnel experiments. Also downstream fractal flanges [75, 70], which are in fact plates with a single opening but with a fractal shaped perimeter (e.g., like a Koch snowflake), the flow exhibits an intensified turbulence compared to flows downstream standard circular orifices. For both these fractal approaches the intensified turbulence does not come at the expense of a significant additional pressure drop.

## Scope of the thesis

From the different options to elevate the turbulence levels the active grid and fractal grid approaches are studied in this thesis. Both these grids are positioned perpendicular to the flow and influence the complete cross-section of the flow, which makes them straight-forwardly compatible with the low-swirl burner, i.e., they can be placed at the position of the standard blocking grid. Therefore, they can be used to address the limited turbulence and combustion in the center of the flame. On the other hand, the synthetic jets and the modulated boundary movement approaches are considered unsuitable for the use in combination with a low-swirl burner. This can be illustrated by the practical implementation of these concepts. The synthetic jets would be positioned along the inner surface of the burner tube and affect only the boundary layer while the inner core, where most enhancement of the turbulence is needed, remains unaffected. The modulated boundary movement approach could be implemented by

letting the outer tube rotate with a modulated rotational speed, creating both swirl and turbulence. However, this will also mainly affect the outer annular part of the flow instead of the inner core. The latter two methods are therefore not further studied in this thesis.

To evaluate whether it is possible to increase the turbulent flame speed in a low-swirl burner by efficiently generated turbulence two separate questions are addressed. First it is assessed whether it is possible to efficiently generate turbulence inside the low-swirl flow field. By using hot-wire anemometry the mean velocity and turbulence intensity are evaluated and, moreover, the energy spectra are obtained to provide information at which scales the turbulence is modified [10]. This information tells which specific turbulence scales are introduced. To monitor the energy input, also the pressure drop over the burner is measured. The combination of these data provides an answer to the question whether it is possible to efficiently generate turbulence. Secondly, it is determined whether the turbulent flame speed is increased when the low-swirl flame is exposed to the modified turbulence. To this end laser-induced fluorescence (LIF) measurement are employed providing two-dimensional cross sections of the instantaneous flame front [28]. A dedicated image-processing algorithm [100] is used to accurately extract the flame front geometry and to allow for calculation of the turbulent flame speed, based on the amount of flame surface.

## Layout of the thesis

The study of the different turbulence generating methods and their effect on a pre-mixed flame is presented in three separate chapters. A compact active grid is presented in chapter 2. The flow downstream of the compact active grid in a pipe flow configuration is investigated as well as in combination with the low-swirl burner. In chapter 3 a parametric study of fractal-grid-generated turbulence is presented which identifies the parameters of the fractal grid patterns that affect the level of turbulence and the turbulent flame speed. This is done in combination with a rod-stabilized, V-shaped flame. Such stabilization mechanism allows for considerable variation in upstream fractal grid geometry. Therefore, trends are obtained, which are also applicable to other premixed flames, over a wider range than would be possible when using a low-swirl flame. The combination of a low-swirl flame and fractal grids is presented in chapter 4. In chapter 5 the conclusions obtained in the separate chapters are summarized.



# Chapter 2

## A compact active grid

### Abstract

A compact active grid is developed with which a pipe flow can be stirred in order to enhance the turbulence. The active grid is composed of a stationary and a rotating disk with characteristic hole patterns. This active grid is placed inside the pipe, allowing flow to pass through it. With only one moving part the design is much less complicated than current active grids. Several combinations of perforated disks are investigated and the resulting control over the turbulent intensity and spectral energy distribution is quantified over a wide range of rotation frequencies. We find that significant turbulent fluctuations are introduced mainly in the energy containing range and partially also in the inertial subrange. These additional fluctuations represent up to 25% of the total energy and are not caused by pulsations of the mean flow. The application of the compact active grid is investigated in a practical, industrial low-swirl burner. Also in this configuration significant peaks are observed in the energy spectrum of the velocity signal. While the turbulent flow upstream of the flame is altered by the compact active grid the low-swirl stabilization mechanism remains intact. However, there is no strong influence on the turbulent flame speed reported when the flame is exposed to the distinct scales introduced into the flow.

### 2.1 Introduction

The improvement of the mixing efficiency in various technological and natural flows is a major topic in the field of turbulence. It is relevant to many practical applications, e.g., in the field of process engineering and combustion. One way of improving mixing is through the use of active grids, increasing turbulence levels as well as the integral lengthscale significantly [41, 66, 71, 81]. However, active grids are technically quite involved and composed of many moving components which make them impractical for enhanced mixing in devices with a size of a few centimeters. The mixing of chemicals

---

Most of the contents of this chapter is based on publication:  
A compact active grid for stirring pipe flow, A.A. Verbeek, R.C. Pos, G.G.M. Stoffels, B.J. Geurts and T.H. van der Meer (2013), in: *Experiments in Fluids*, 54:10(1594).



in a pipe or the combustion in a burner cannot benefit from currently available active grids with sizes in the order of a meter. In this paper a compact active grid is presented, which consists of two perforated disks; a static one and a rotating one. By characterizing the flow downstream of this active grid with hot-wire measurements we show that a significant amount of kinetic energy, up to 25%, is contained in a range of specific modes, introduced to the flow by the active grid. These modes may be controlled by the rotation frequency and the combination of disks used. This effect of enhanced modes is strongest in the larger, energy containing scales. We establish the extent to which the enhancement of modes penetrates into the inertial range.

Mixing is essential in many applications. As mentioned by Pope [82] this ranges from releasing pollutant streams into the atmosphere, to mixing chemical reactants in a combustor or a reactor. Usually, it is desired that the mixing takes place rapidly and in a limited space, requiring low energy input. The ability of manipulating or even controlling turbulence to improve mixing is a field of intense research [15, 21, 22, 47, 48]. In this chapter we pursue this by developing and characterizing a compact active grid mixer which is considerably simplified relative to existing active grids. This opens possibilities to apply such compact active stirrers in practice.

Several studies in the past were dedicated to intensify turbulence with non-classical grids. For example Gad-el Hak and Corrsin [29] used a grid structure that introduces high speed jets into the flow. When upwind jets are used the turbulence levels are increased at the expense of a higher pressure drop. The active grid with vibrating flaps by [61] also shows an increase in the turbulent intensity. But as noted by Larssen and Devenport [55] perhaps the most successful forcing strategy to enhance the turbulence is through the use of active grids as described by Makita [66]. However, all the grids mentioned are composed of many different moving parts or are required to allow for internal flow (for the jet-grids), which makes them not suitable for pipe flows with a diameter of only a few centimeters. Here, we present a compact active grid to stir a turbulent pipe flow. It is composed of a set of two disks of which one is stationary and one is rotating. These disks have characteristic hole patterns that upon rotation create a space and time dependent perturbation of the flow, with only one moving part. The jets that are introduced show similarities with Gad-el Hak and Corrsin's jet grid, but since they are varying in time there is also an analogy with the grid proposed by Makita when used in a deterministically forced way such as adopted by Cekli et al. [15].

Research into flow control with an active grid is also stimulated by the phenomenon of 'resonant' turbulence. As shown by Cekli et al. the dissipation rate of a flow can be significantly increased (up to 50%) when the forcing frequency of an active grid mode is close to the 'internal frequency' of the flow. In literature this 'internal frequency' is always associated with an estimate of the large-eddy turn-over time [12, 15, 48, 49]. Lohse [64] showed using a mean-field analysis that the turbulence level may be increased by using a time-periodic forcing. In later direct numerical simulations [48, 49] this enhanced turbulence was investigated in more detail. The main turbulence enhancement at a frequency associated with the large-eddy turn-over time was established at several Reynolds numbers and for a range of flow properties. In these numerical studies a large-scale forcing was applied with an amplitude modulated in time at a specified frequency. This type of agitation resulted in a response maximum for the turbulent kinetic energy in the system when the modulation frequency is close to the internal frequency of the flow.

The phenomenon of resonant turbulence was observed experimentally in flow between two counter-rotating disks [12]. The rotational speed of the disks was modulated with specified amplitude and frequency. A resonant behavior was observed when the modulation frequency is close to the internal frequency of the flow. At these conditions the flow contained more turbulent kinetic energy while the same amount of energy was dissipated as in the unmodulated case. Another experimental observation of resonant turbulence is presented by Cekli et al. [15] where an active grid is placed upstream in a wind tunnel. Although no energy input rate was measured in these experiments, there is a significant response maximum present in the dissipation rate.

What all the studies on ‘resonant’ turbulence have in common is the observation that a more intense turbulent state can be achieved when a large-scale time-dependent forcing is applied with a frequency close to the inverse of the large-eddy turn-over time. The compact active grid that is considered in this paper is designed such that it can be operated in this frequency range.

In this chapter a study is presented on the flow emerging from a compact active grid. This grid serves as a research tool to examine the possibility of creating a more intense turbulent flow. As a first step the turbulence is characterized. Moreover, by varying the rotation speed of the grid an optimal excitation frequency is sought. Moreover, the application of the compact active grid for premixed combustion is investigated in a low-swirl burner [17], which is known for its extremely low  $\text{NO}_x$  emissions. When increasing the conversions rates of these flame by efficiently enhancing the level of turbulence it is expected that the usable range of these burners can be extended to more power-dense applications like gas-turbine power stations.

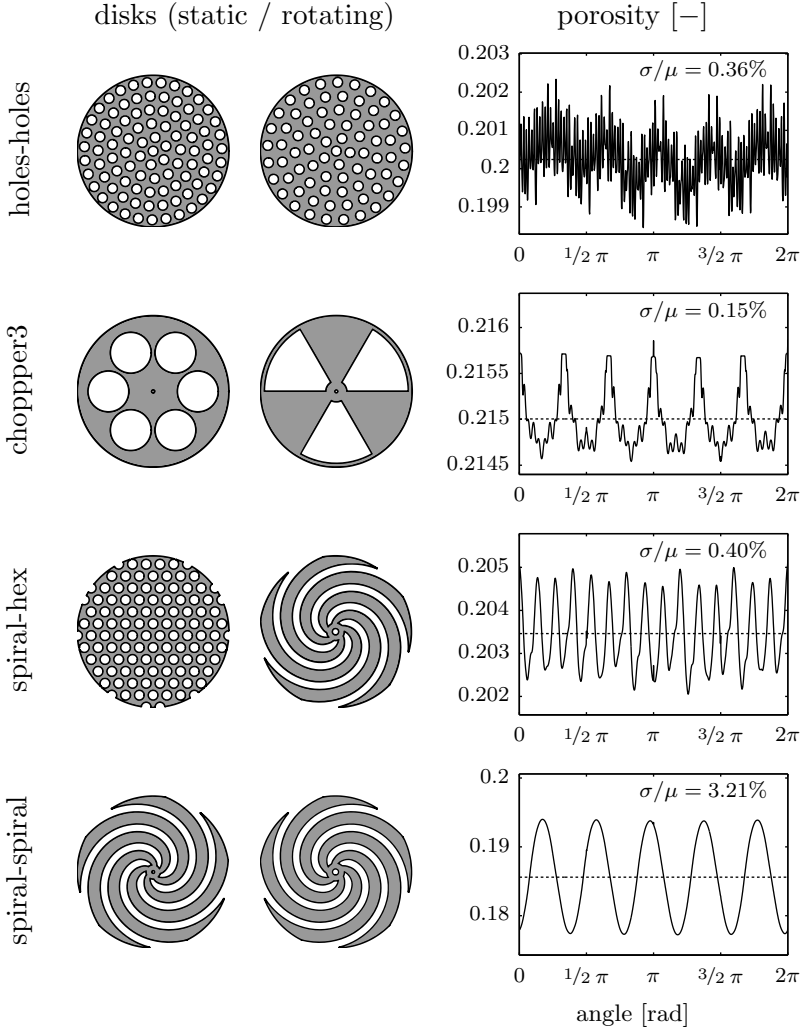
The organization of the paper is as follows. In the next section the compact active grid is described in more detail. In section 2.3 the design and its peripherals are discussed as well as the measurement equipment. In section 2.4 the properties of the turbulent flow behind the grid are presented in terms of mean turbulent quantities and the spectral distribution of the turbulent kinetic energy. In section 2.5 the application of the compact active grid for low-swirl combustion is examined. Concluding remarks are made in section 4.5.

## 2.2 Compact active grid based on a rotating disk

In this section the design of the compact active grid is discussed. First the concept is discussed and subsequently, main features, perturbed scale range and a variety of geometrical ‘hole’ patterns for the disks are described.

### 2.2.1 Concept of two perforated disks

The active grids as first described in [66] are composed of a mesh with horizontal and vertical rotating rods with vanes attached to it. Depending on the rotation of each rod, its vanes can be positioned anywhere from perpendicular to the flow, i.e., blocking the flow, to aligned with the flow, representing low local blockage. Such a grid can create a wide variety of time-dependent patterns, see for example [15]. To realize a time-dependent forcing which offers a similar control over local blockage and passage of the fluid, but with a construction that is significantly simplified, we use



**Figure 2.1:** Different active grid configurations. The two disks together form a time-dependent arrangement of pulsating jets upon rotation of the (right) upstream disk relative to the stationary, downstream (left) disk. In the graphs the open area fraction (porosity) as function of the rotation angle is plotted. The dashed line indicates the mean porosity. The level of variation in porosity is indicated by the ratio of the standard deviation,  $\sigma$ , and the mean,  $\mu$ , of the porosity signal.

a set of two perforated disks of which one is rotating. This concept of two adjacent perforated disks can be made much more compact.

The movement of one perforated disk in front of another will cause the perforations to create an intricate, controllable pattern of periodically opening and closing local streams. The time-dependent array of pulsating jets that is created in this way can be controlled by changing the rotation speed of the moving disk. In Figure 2.1 four different examples are shown that were used to create an active grid in this paper. The list of combinations of perforated disks that can be used to create the active grid is endless. We would like to point out that the current work is intended as a first step to explore the possibilities of the presented compact active grid. Therefore multiple grid parameters were varied to study a wide range of flow conditions, while employing only a few grid patterns. These all have specific roles with respect to the resulting flow manipulation, which will be presented later. Here four combinations are used to explore the possibilities. These four are intrinsically different from each other although the induced jet-frequencies lie in the same range and the porosity of the grids are comparable.

Since the active grid contains a rotating disk it might induce a secondary, tangential flow. In order to minimize this effect the rotating grid was placed upstream of the stationary one. By means of flow visualization with smoke it was verified that no detectable amount of swirl is created by the active grid in the adopted configuration when operated at maximum rotation frequency.

## 2.2.2 Dimensions

Dimensions of the pipe are chosen such that they are compatible with a lab scale burner and compatible with large scale forcing of the flow. This resulted in a 44 mm diameter tube with a grid placed 116 mm upstream as can be seen in Figure 2.2. The measurements are mainly performed 20 mm downstream of the exit of the pipe.

In Figure 2.1 we show the porosity-variations as a function of the rotation angle of the rotating disk. All the grids are designed such that their variation of total open area is small. In this way it is investigated if turbulence can be enhanced by an active grid without creating a pulsation of the mean flow rate. As a measure for the porosity-variations we consider  $\sigma/\mu$  in terms of the standard deviation,  $\sigma$ , and mean,  $\mu$ , defined as:

$$\sigma = \sqrt{\frac{1}{2\pi} \int_0^{2\pi} (A(\phi) - \mu)^2 d\phi} \text{ and } \mu = \frac{1}{2\pi} \int_0^{2\pi} A(\phi) d\phi \quad (2.1)$$

where  $A(\phi)$  denotes the open area available for the fluid to flow through at rotation angle  $\phi$ . For all the grids the porosity-variations are very low, with the relative variation in open area  $\sigma/\mu$  well below 0.5% apart from the spiral-spiral configurations, for which  $\sigma/\mu = 3.2\%$ .

**Large-eddy turn-over frequency** The typical velocity fluctuations achievable in our experimental set-up are expected around 0.7 m/s. In addition, in the available geometry the order of the integral length-scale is around 1 cm. In total this leads to an expected integral timescale of 0.014 s, implying a 70 Hz large-eddy turn-over frequency. The design of the grids is such that a forcing with a frequency around

70 Hz can be generated, within a maximum rotation frequency of 35 Hz for the disk itself. It must be pointed out that  $\tau^{-1}$  can be varied by changing the volumetric flow-rate; here we limit ourselves to one specific case.

### 2.2.3 Variety of geometric patterns

#### Holes-holes

The static disk contains holes of 3 mm diameter that are placed at different radii. These holes are opened and closed by the movement of the holes of the rotating disk in front. Since the number of holes on the rotating disk changes with the radius, also the frequencies of the jets that are formed differ. The six perforations at the innermost circle of the static disk will pulsate at five times the rotation frequency, i.e.,  $5f_r$ , since there are five perforations at the innermost circle of the rotating disk. For the perforations located at each subsequent radius the induced jet frequency will increase with  $5f_r$  up to  $25f_r$  for the perforations at the outer ring. An optimization was performed to obtain a low variation of the porosity. In fact, the angle offset between the five rings of perforations on both disk was randomly varied for 100 times. The configuration that yielded the lowest variation in porosity was selected.

#### Chopper3

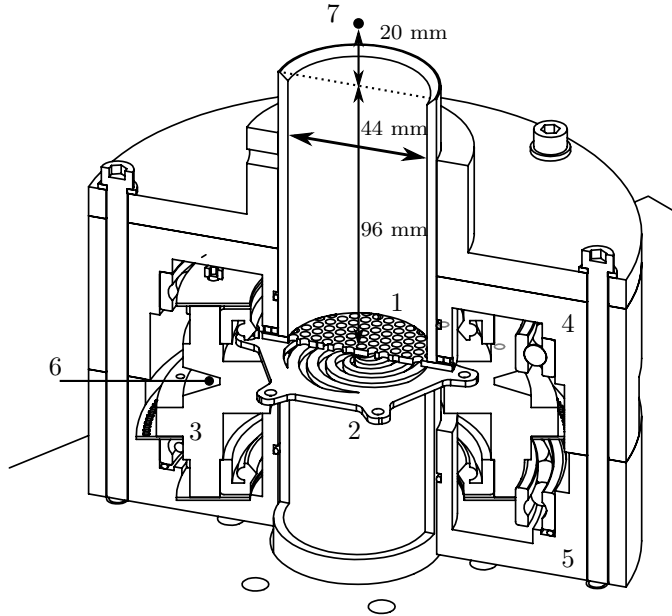
The chopper3 configuration contains six holes of 12 mm of which at any time effectively three are open and three are closed. These are continuously alternating by the openings in the rotating disk and will create a forcing with only a single frequency contrary to the range of frequencies generated by the holes-holes configuration. Since each hole is opened and closed three times in one rotation, jets with a frequency of  $3f_r$  are created. Compared to the holes-holes configuration, the forcing will apply at a larger scale due to the larger diameter of the holes.

#### Hex-Spiral

To create pulsating jets with a single frequency all over the grid, the perforated rotating disk is replaced by a disk with spiral shaped slots of 3 mm width. As this disk is rotating, the spiral shaped slot is moving either outward or inward depending on the rotation direction. The slots move across all perforations of the static disk with a constant velocity, due to the arithmetic or Archimedean spiral shape, where the radius of the center of the slot linearly increases with the rotation angle. This causes a single jet frequency of five times the rotation frequency for all jets of the static disk, equal to the number of spiral slots multiplied with the rotation frequency.

#### Spiral-Spiral

By using two spiral shaped disks, a pattern of moving non-pulsating streams is created, meandering all over the opening. These streams are either moving inward or outward depending on the rotation direction. This configuration results in a higher level of variation in the open area with a clear period five oscillation as can be seen in the bottom graph of Figure 2.1. It is therefore to be expected that this will force the flow at five times the rotation frequency.



**Figure 2.2:** Construction of the driving mechanism of the active grid. 1 - static disk. 2 - rotating disk. 3 - rotor that is externally driven. 4,5 - housing. 6 - V-groove for external drive. 7 - measurement location.

## 2.3 Construction of active grid and experimental set up

Details of the experimental facility are presented in this section. In subsection 2.3.1 the compact active grid construction is described. Subsection 2.3.2 is dedicated to the hot-wire technique, the data acquisition and the data processing to measure the turbulent velocity fluctuations in the flow downstream of the active grid.

### 2.3.1 Construction

To place the active grid in a pipe flow a special construction is created. It is designed such that only the active grid will obstruct the flow and no other (moving) parts will influence the flow. The rotating disk is externally driven and therefore the disk extends through the pipe dividing it into two parts. In Figure 2.2 a cross section is presented where the different parts are labeled. The rotating disk is attached to a rotor that is mounted with bearings in the specially developed housing. The combination is externally driven by an AC motor that is connected by a V-belt. This motor is connected to a frequency controller to regulate the rotation speed. The actual speed of the grid is measured by an optical encoder that detects the holes of an encoder ring attached to the rotor. With a closed loop control system the grid is rotating at the desired set-point with a precision better than 0.1 Hz. The maximal rotation frequency is 35 Hz, limited by mechanical restrictions of the bearings and sealing. This maximum frequency is sufficient to perform a frequency scan with the

induced jet frequencies of the different grids in the range of the flow's large-eddy turn-over frequency and beyond. The lowest jet frequency is generated by the chopper3 configuration, which is  $3f_r$ . This will be maximally 105 Hz, which is higher than the expected large-eddy turn-over frequency of 70 Hz. The induced frequencies of the other configuration are higher and are therefore also capable of exciting the flow at even shorter timescales. For investigating the phenomenon of resonant turbulence this should cover the relevant frequency range.

Besides an optical encoder for the measurement of the rotation speed there is a second optical encoder that provides a single pulse per rotation to be able to calculate the absolute position of the grid. In this way it is possible to obtain statistics that are conditioned on the grid position.

The flow through the grid is regulated by a mass-flow controller and is set for all experiments described here to  $30 \text{ m}^3/\text{hr}$ . This corresponds to a bulk velocity of  $5.5 \text{ m/s}$ . A mass-flow controller is used to ensure good repeatability of the experiments, with an error below 1% of the set-point value. The air is supplied to the grid through a one meter long tube with a restriction installed upstream which cancels upstream curvature effects and results in a symmetrical and axial flow profile.

### 2.3.2 Experimental methods

At 20 mm downstream of the exit of the tube, on the central axis (see Figure 2.2) a locally manufactured single hot-wire probe of  $5 \text{ }\mu\text{m}$  diameter platinum coated tungsten wire with a length of 0.73 mm is placed. This probe is used in combination with a Dantec 90C10 Constant Temperature Anemometer (CTA) module. The overheat ratio is set to the typical value of 0.8. This results in a sensor temperature of approximately  $230^\circ\text{C}$ . To determine the frequency response of the hot-wire, the CTA's internal square wave test is used. This indicates a bandwidth of 75 kHz which is sufficient to capture the Kolmogorov scales that have a frequency,  $f = U/2\pi\eta$ , between 10 and 25 kHz for the different grids, based on the mean bulk velocity  $U$  and Kolmogorov lengthscale  $\eta$ . The data is captured with a NI 9215A BNC at 50 kHz with 16 bit resolution. The internal low-pass filter of the CTA was used with a cut-off frequency of 30 kHz to suppress noise and avoid aliasing.

To convert the voltage to velocity a calibration is performed. Velocities between 0.1 and 1 m/s are obtained by applying a calibrated volumetric flow rate through a straight pipe such that a laminar velocity profile develops of which the central velocity is known, similar to the method described in [59]. The high velocity range, between 3 and 15 m/s is calibrated by the commonly used calibration nozzle [10]. The largest uncertainty originates from the limited accuracy of the manometer, measuring the pressure difference over the calibration nozzle, which has a resolution of 1 Pa. At a velocity of 4 m/s with an uncertainty of 0.5 Pa, the error in the velocity is 5%. Such accuracy in absolute value is quite acceptable and appears adequate to obtain the trends in mean velocity and turbulent intensity with changing rotation frequency. It also allows an accurate evaluation of the dissipation rate and turbulent lengthscales.

The sealing between the rotor and the housing is lubricated to reduce external heat production. In the current setting the heat production causes the flow to heat up a few degrees, measured just downstream of the hot-wire probe. For the measurements presented in this paper the maximum temperature rise is about eight degrees. This rise in temperature needs to be corrected for. The most commonly used correction,

as presented by Bruun [10], breaks down at temperature changes of more than two or three degrees and is therefore not applicable. However, the method proposed by Hultmark and Smits [37] incorporates the changes in fluid properties with temperature and works very well for changes up to 15 degrees. The benefit of applying this correction method is that only a single calibration is needed at a known temperature.

Since the heat is generated at the wall of the tube, this will induce some non-isothermal flow field, resulting in not only a rise in mean temperature, but also in some turbulent fluctuations in fluid temperature, which may slightly bias the observed level of velocity fluctuations. By employing the multiple overheat ratio method [10] the standard deviation in fluid temperature is estimated to be 1°C at maximum  $f_r$ . The resulting bias in the standard deviation of the measured velocity is below 5% for our measurement conditions. This is considered acceptable to identify the dependency of turbulence properties on the operating frequency of the active grid.

In order to measure the pressure difference across the grid, which is a measure for the energy input, a differential pressure sensor is mounted 10 cm upstream of the grid. The pressure drop can be measured in a range of 0-2000 Pa with an error of 1%. Measurements show that the time averaged pressure drop over the active grid remains fairly constant. It is invariant of  $f_r$  within 2% and does not reveal a frequency where turbulence is generated at lower expense of energy; it is therefore not shown in this paper.

## 2.4 Turbulence behind the active grid

The turbulence that emerges from the active grid is analyzed in this section. The main purpose is to characterize the turbulence to identify a possible optimal operating frequency. This characterization is based on the r.m.s. of the fluctuating part of the velocity, spectral distribution of the fluctuations and response of grid related velocity fluctuations. The dependence of these quantities on the rotation frequency is well estimated by studying only the axial component of the velocity. For a more accurate quantification cross-wires could be used. Especially, to identify the degree of validity of the isotropy assumption.

First, time-averaged quantities such as mean velocity and turbulent intensity are presented as function of the rotation frequency. It is found that there is only a limited effect of the rotation frequency on the mean quantities. The dependence of the response due to changing the grids is more prominent. The fluctuating velocity, that can be split in two parts, i.e., a deterministic and a turbulent one, are illustrated by the phaselock averaged velocity and the probability density function (PDF) of the velocity. Subsequently, energy spectra are presented which show a strong effect of the active grid on the fluctuations. A range of definite peaks was observed on top of the turbulent background spectrum, arising from the rotating disk perturbations. The strength of the additional peaks is quantified in terms of their contribution to the kinetic energy. Finally, the spatial structure of the fluctuations is presented, displaying a low level of flow pulsation.



### 2.4.1 Effect of rotating grid on mean quantities

#### Mean and turbulent velocity

For the different grids five-minute long velocity traces were recorded. These time-traces contain about  $1 \times 10^5$  integral lengthscales, which is sufficient to obtain converged statistics. The rotation frequency,  $f_r$ , was varied in integer steps between 1 and 25 Hz. Unless stated otherwise the rotation direction was clockwise when looking from downstream. Basic properties such as the mean velocity,  $\bar{U}$ , and turbulent intensity,  $I = u'/\bar{U}$ , with  $u'$  being the standard deviation of the velocity at the measurement location, are plotted in Figure 2.3 for the four grids. Here, the averages are taken over the entire time-trace of length  $T = 5$  min, i.e.,

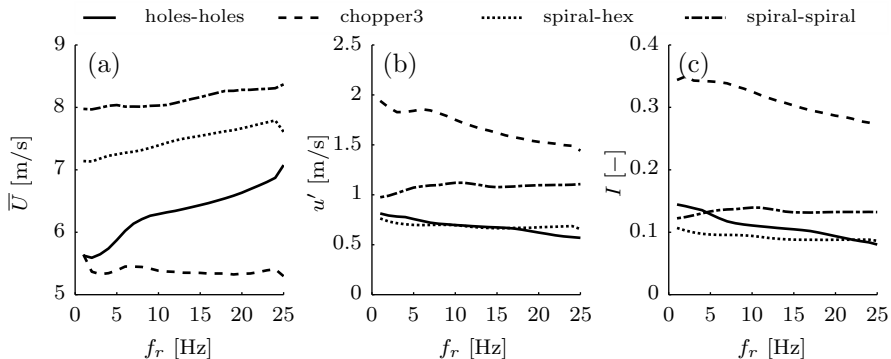
$$\bar{U} = \frac{1}{T} \int_0^T U(t) dt ; u' = \sqrt{\frac{1}{T} \int_0^T (U - \bar{U})^2 dt} \quad (2.2)$$

where  $U(t)$  denotes the recorded signal at the measuring point. The point at which the signals were obtained is on the centerline of the pipe, 116 mm downstream of the grid (Figure 2.2). It can be seen that there is a dependence of  $\bar{U}$  on  $f_r$ . With the exception of the chopper3 case the mean velocity is increasing with increasing rotation frequency. Since the volumetric flow rate is kept constant, the effect of rotation is expressed as a changing radial profile of the velocity, or more specifically an increased velocity at the centerline. For the two grids involving a rotating spiral disk a secondary flow is induced by the inward motion of the spiral slots, resulting in a higher flow at the centerline, with increasing rotation rate. When the rotation direction is set counterclockwise the opposite effect was observed. For the holes-holes case for both rotation directions an increasing trend for the velocity at the centerline is observed. This can be understood by the argument that every time a hole opens, the flow needs to accelerate to pass through it; this induces a resistance. For the holes further from the centerline the acceleration, and hence the pressure drop will be larger compared to the value at the centerline. This results in a relatively higher flow at the centerline with increasing rotation rate, avoiding the higher flow resistance near the edge of the rotating disk. The fact that  $\bar{U}$  in the chopper3 case is independent of  $f_r$  can also be understood by this argument, since all the holes are at the same radius and will have the same pressure drop contribution.

All the grids have a similar blockage percentage. Still, the turbulence level of chopper3 is significantly higher than that obtained with the other three configurations. Due to the larger scales that are introduced by the holes of the chopper3 grid it is expected that these fluctuations will decay more slowly than for the other grids, hence resulting in a higher signal at the measuring location 20 mm downstream of the pipe exit. This is followed by the spiral-spiral case which has slightly larger openings than the holes-holes and spiral-hex configurations. Besides the differences in the average level of turbulence associated with the different grids, there is only a small dependence on  $f_r$ , which in all cases is decreasing with  $f_r$ . No response maxima are observed in this parameter range.

#### Phaselock averaged velocity and PDF

The phaselock averaged velocity,  $\bar{U}_\alpha$ , for different frequencies, i.e., 2, 15 and 25 Hz is shown in Figure 2.4. At low  $f_r$  the flow more closely follows the periodic forcing



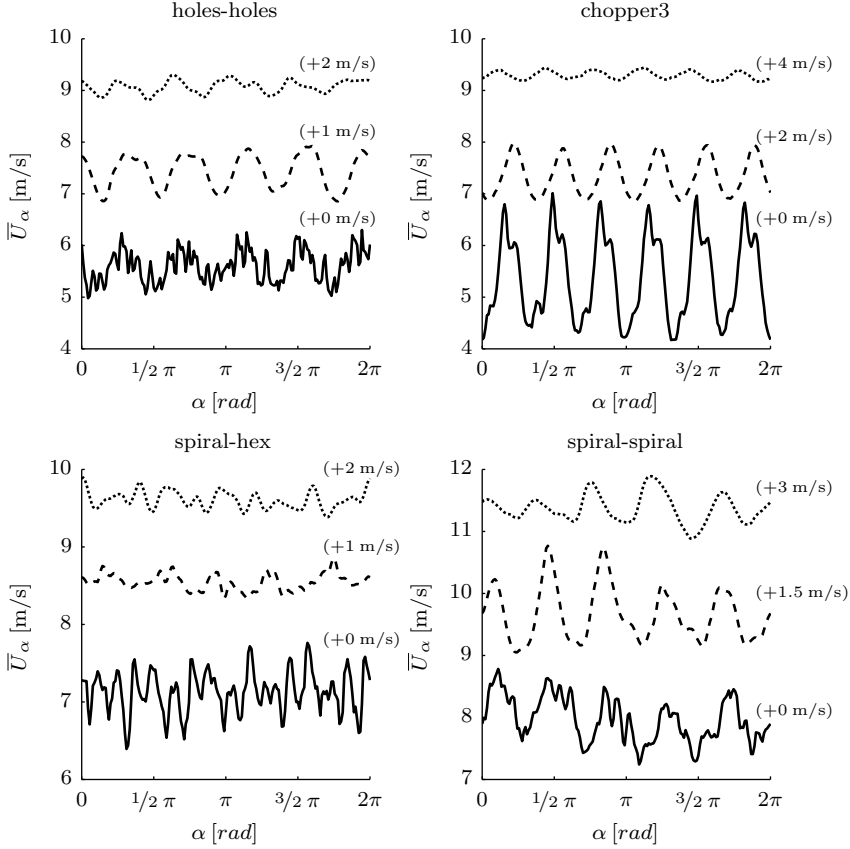
**Figure 2.3:** (a) Mean velocity. (b) Turbulent velocity. (c) Turbulent intensity. Measured on the centerline 116 mm downstream of the grid.

of the grid than at higher  $f_r$ . The fine scale fluctuations introduced by the grid are detected at the measurement location primarily when  $f_r$  is low as can be seen by the fluctuations in  $\bar{U}_\alpha$ . When  $f_r$  is increased  $\bar{U}_\alpha$  tends to be more smooth and of smaller amplitude.

PDF's of the velocity signal are shown in Figure 2.5. These are shown for a single rotation frequency ( $f_r = 12$  Hz), since the shape of the distribution was found not to change significantly when changing  $f_r$ . The turbulence for the chopper3 grid renders a non-Gaussian distribution. For the other cases the graph of the PDF closely follows a parabolic shape on a log-scale corresponding with a Gaussian distribution. For all cases the PDF's indicate that  $U$  consists of turbulent fluctuations. Part of the fluctuations in  $U$  are of deterministic nature as was established by the non-constant periodicity in  $\bar{U}_\alpha$ . To quantitatively compare the deterministic and random part of the fluctuations, the energy spectrum is computed, analogously to [15]. The fraction of energy represented by the peaks in the energy spectrum introduced by the active grid is identical to the ratio of variances of  $\bar{U}_\alpha$  and  $U$ .

## Homogeneity

Although the upstream velocity profile is axisymmetric, it is not uniform due to the nature of pipe flow. Within the inner region of the flow, defined as  $r \leq 10$  mm, the level of inhomogeneity downstream (116 mm) of the grid is assessed. Measured by the maximum deviation of  $\bar{U}$  from the average value of  $\bar{U}$  in the inner region the level of inhomogeneity is below 6.7% for all grids with the exception of the spiral-spiral case where a level of 14% is observed. In this case a velocity profile closer to a top-hat shape is created. The heterogeneity in  $u'$  measured in the same way is below 8.7%, but here the exception is the spiral-hex grid with 24%. The level of inhomogeneity remains fairly constant with varying  $f_r$ . Therefore, we present only measurements taken on the centerline for a characterization of the turbulence created by the active grid and in particular its dependence on  $f_r$ . This centerline information is a concise and representative characterization for the turbulent flow in the entire inner region.

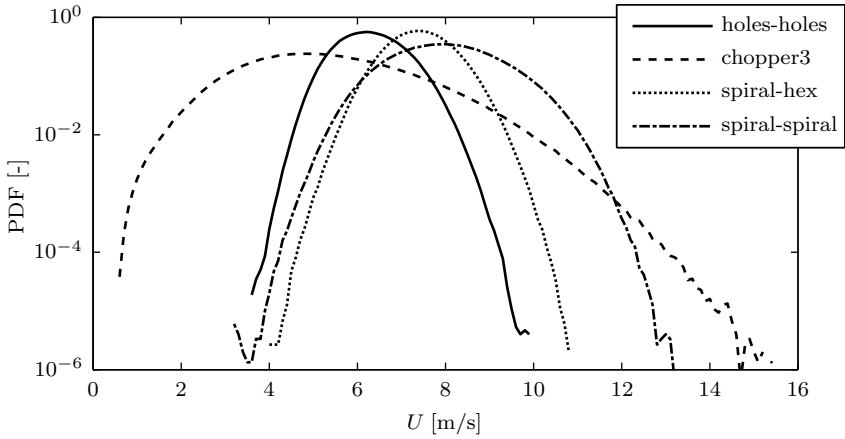


**Figure 2.4:** Phase averaged velocity for different  $f_r$ . For the sake of clarity the consecutive graphs are vertically shifted by an offset as indicated between. Solid line:  $f_r = 2$  Hz, dashed line:  $f_r = 15$  Hz, dotted line:  $f_r = 25$  Hz Measured on the centerline 116 mm downstream of the grid.

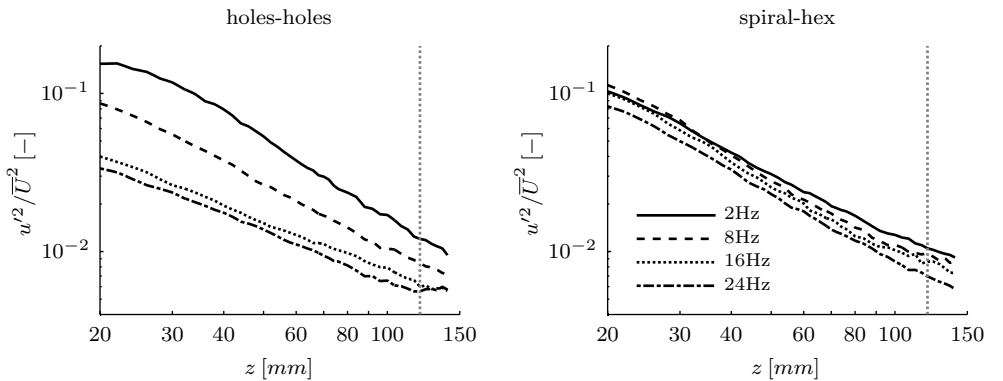
## Axial dependence

In this first step we focus on a single point of interest where we search for enhanced turbulence. Obviously, the results obtained in this single point cannot be used to make quantitative claims in the rest of the domain. To avoid expensive and possibly unnecessary measurement campaigns quantitative results were obtained for a single point to quantify the possible turbulence enhancement.

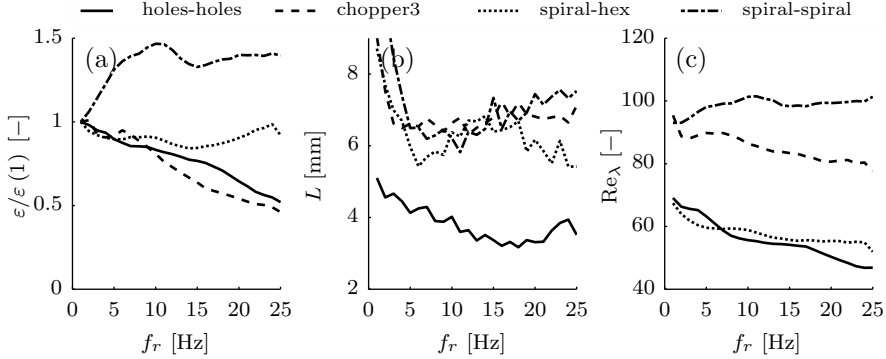
The selected measurement location is in the decaying region as can be inferred from the mesh-size normalized downstream  $z/M$  distance. For the mesh-size  $M$  the center-to-center distance of the static holes is used, which is 5 mm in the holes-holes grid and spiral-hex grid and 13 mm for the chopper3 grid. For the spiral-spiral the mesh size is less trivial to define. The width of the openings is 3 mm while the length



**Figure 2.5:** Probability density function of the velocity signal for different grids. The operating frequency is  $f_r = 12$  Hz. Measured on the centerline 116 mm downstream of the grid.



**Figure 2.6:** Decay of  $\frac{u'^2}{U^2}$  along centerline. The vertical dotted line indicates the measurement location used for majority of the measurements presented in the paper.



**Figure 2.7:** (a) Normalized dissipation rate. The values of  $\varepsilon(1)$ , the dissipation rate at a rotation frequency of 1 Hz, are 91.5, 1556, 74.6, 104.5  $\text{m}^2/\text{s}^3$  for holes-holes, chopper3, spiral-hex and spiral-spiral resp. (b) Integral lengthscale. (c) Taylor-scale Reynolds number as function of the rotation frequency. Measured on the centerline 116 mm downstream of the grid.

of an opening is up to 10 mm. We use an average value of 5 mm.

For all grids expect the chopper3  $z/M$  is in the order of 20 which is in the decaying region [82]. For the chopper3 it is about 10, due to the much larger hole size. To confirm this behavior the decay of turbulence is measured for two grids (holes-holes and spiral-hex) and shown in Figure 2.6. The straight lines on the logarithmic scale confirm the power law decay, especially at the location indicated by the vertical dotted line where the majority of the measurements were taken.

### Scales of turbulence

To quantify the turbulent scales present in the flow and the way they are affected by the active grid, the dissipation rate,  $\varepsilon$ , the integral lengthscale,  $L$ , and the Taylor-Reynolds number,  $Re_\lambda$ , are determined. The dissipation rate, characterizing the smallest scales of the turbulence, is under the assumption of isotropy defined by  $\varepsilon = 15\nu \overline{(\partial u/\partial x)^2}$ . We estimate  $\overline{(\partial u/\partial x)^2}$ , by integrating the dissipation spectrum, i.e.,  $\overline{(\partial u/\partial x)^2} = \frac{4\pi^2}{U^2} \int f^2 E(f) df$ . To avoid the high frequency noise from biasing  $\varepsilon$ , the method described by [3] is used, where the high frequency range of the measured spectrum is replaced by a fitted model. Necessary correction for the finite wire length and sample time are made according to [11]. It was observed that these two corrections yield relative changes in the estimates for  $\varepsilon$  in the order of 3% and 40-70% for Antonia's and Burattini's correction respectively. The significantly stronger turbulence for the chopper3 case requires a higher correction factor for Burattini's correction; up to a factor of three.

We use as kinematic viscosity of air the value from [8] for a temperature of 20 °C, i.e.,  $\nu = 1.5 \times 10^{-5} \text{ m}^2/\text{s}$ .

The integral lengthscale,  $L$ , which is a measure of the largest structures present in the flow, is defined by  $L = E(0) \bar{U}/4u'^2$  [82], where  $E(0)$  is determined from the lowest wavenumber value of the filtered energy spectrum ( $E_b$ ) as defined in section 4.2.

This approach is used to avoid biasing of  $L$  due to deterministic fluctuations induced by the grid. Also the averaging involved in the Welch method to determine the spectrum avoids biasing of the lowest wavenumber value due to drift or low frequency unsteadiness. We averaged over 228 samples, and independently verified that this amount of samples in the Welch method reduced the relative error to below 3% for  $E(0)$ .

A more common definition of the integral lengthscale would require integration over the normalized autocorrelation of the turbulent velocity. In view of the periodic forcing this formally equivalent approach is less suited here [77]. Finally,  $Re_\lambda$  is defined as  $Re_\lambda = u'\lambda/\nu$ , with the Taylor length scale,  $\lambda = \sqrt{u'^2/(\partial u/\partial x)^2}$ .

To obtain these quantities from the recorded time traces spatial information is extracted using Taylor's frozen turbulence hypothesis. Although it is common practice to use Taylor's hypothesis, one should be aware of the fact that it is accompanied with inaccuracies. [24] report an overview of error assessments when applying Taylor's hypothesis. A relatively reliable estimate of  $(\partial u_1/\partial x_1)^2$  can be obtained with a single wire using Taylor's hypothesis, but the isotropy approximation is unlikely to be adequate as stated by [3]. Absolute values in  $\varepsilon$  and other quantities derived from it, like  $\lambda$  or  $\eta$  are likely to contain similar inaccuracies. However, a good correlation between the estimate and the exact value of the dissipation rate was reported by [24], which indicates that the described method is well suited to identify trends in various characteristic turbulence quantities like  $\varepsilon$  and  $Re_\lambda$  with changing  $f_r$ . This is the way we use the estimates for the dissipation rate, i.e., indicative more of trends when changing the forcing frequency than of absolute values for this quantity.

Isotropy is assumed in the calculation of  $\varepsilon$ . This was not directly assessed. Based on the observed power law decay of the turbulent intensity and on the fact that the measurement location is more than two integral scale downstream of the grid ( $x/\bar{U} > 2L/u'$ ), we expect a reasonable level of isotropy, as reported for other active-grid experiments [41, 66] at similar conditions. Specifically, an isotropy level of 1.2 is expected to apply.

In the graph of Figure 2.7a  $\varepsilon/\varepsilon(1)$  is plotted as function of  $f_r$ . Since the compact active grid is not uniquely defined for the non-rotating case, the dissipation rate at a rotation frequency of 1 Hz is used as a reference to be able to compare the dependency of  $\varepsilon$  on  $f_r$  for the different grids in a single graph. In the normalized representation of  $\varepsilon$  different responses of  $\varepsilon$  on  $f_r$  are obtained for the different grids. Only in case of the spiral-spiral grid  $\varepsilon$  is increasing. This increase is up to 45% at 10 Hz where a maximum is located. For the three other configurations only a decrease in  $\varepsilon$  is observed. For the holes-holes and the chopper3 a monotonically decrease is measured down to 50%. The response of  $\varepsilon$  is most invariant for the spiral-hex grid, where it changes between 1 and 0.85. Although there is a modest maximum in  $\varepsilon$  for the spiral-spiral grid it is believed that this is not directly related with a 'resonance' as observed in the work of Cekli et al. [15]. The main contradictory fact is the lack of a decreasing response at frequencies beyond the maximum, which would be expected based on 'resonant' turbulence [12, 15, 48, 49]. The absolute value of  $\varepsilon$  for the chopper3 grid is an order of magnitude larger than for the other three grids. This is related to the much stronger turbulence.

The value of  $L$  is between 3 and 8 mm for all the grids. The holes-holes grid, which has the smallest openings, corresponds with the lowest value of  $L$ .

The other grids that involve larger openings, albeit only for the rotating disk for the spiral-hex grid, results in larger  $L$ . For the grids involving a spiral, the graphs of  $L$  roughly coincide up to  $f_r = 12$  Hz. For higher rotation frequencies the spiral-hex case was found to have a lower integral lengthscale than the spiral-spiral case. It was seen that the frequency dependence is stronger for active grids composed of two very different disks. In fact, at high frequency the effect of the rotating disk appears less important for the large scales in the flow. Apparently, the flow cannot follow this rapid agitation. This would suggest that the integral lengthscale is mainly determined by the properties of the static disk at these high frequencies.

With  $L$  being closely related to the typical size of an opening in the grid, our rotating active grid acts very differently from the original active grid of [66], for which  $L$  is found to increase an order of magnitude up to four times the mesh size. However, in the work of [15], where similar to our case and unlike Makita’s study a deterministic forcing pattern was used, the integral lengthscale is found to remain of the size of the openings created by the active grid independent of the forcing frequency.

The Taylor-scale Reynolds number,  $Re_\lambda$ , shows a significant difference between the grids with small holes (holes-holes, hex-spiral) and the grids with larger openings (chopper3 and spiral-spiral). The cases with larger holes have a higher overall  $Re_\lambda$ , indicating a larger separation between the smallest scales and the largest scales [82]. Although there is variation in the integral lengthscale between these grids, with a factor of two difference in  $Re_\lambda$  there is more turbulence in the smaller scales for the grid with large  $Re_\lambda$ . This can be stressed by the fact that the separation of scales,  $\eta/L$  with  $\eta$  being Kolmogorov lengthscale, is proportional with  $Re_\lambda^{-3/2}$  [82]. Hence, if there is not much variation in the integral lengthscale, but a factor of two difference in  $Re_\lambda$ , this implies more mixing on smaller scales.

The time-averaged quantities that were presented show differences between the various grids. Especially the chopper3 grid creates a much stronger turbulence compared to the other grids for all  $f_r$ . This is expressed by the significantly higher values of  $I$ ,  $\varepsilon$  and  $Re_\lambda$ . For all grids the dependence of the various quantities on the rotation frequency does not reveal a specific frequency where the turbulence is maximized. A maximum enhancement could have been expected based on other experimental studies on ‘resonant’ turbulence from Cekli et al. [12, 15]. However, there are differences in  $Re_\lambda$  and the level of fluctuation in the porosity of the grid. In [15]  $Re_\lambda$  is about 500 and the level of porosity fluctuation, defined as  $\sigma/\mu$ , is about 7%. These differences might explain the absence of a pronounced optimal frequency to operate the grid as far as dissipation rate and integral scales are concerned.

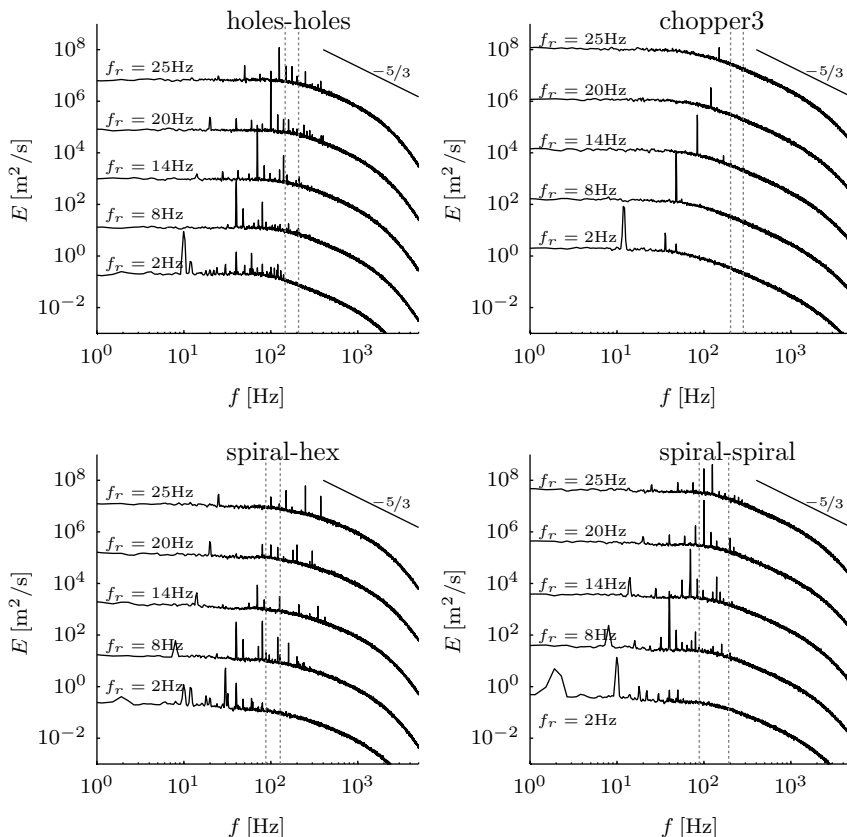
## 2.4.2 Spectral distribution of energy

The active grid forms pulsating jets with frequencies that are integer multiples of the rotation frequency. It is expected that this set of frequencies will be dominant in the flow. The distribution of the turbulent fluctuations that are present in the flow can be visualized in the energy spectrum. In this way it is investigated in which frequency range the fluctuations were introduced and what their relative strength is with respect to the total turbulence level.

The spectra are calculated according to the method introduced by [105] which consists of the following steps. The spectrum is defined as  $E = \frac{1}{n} \sum_i |\mathcal{F}(u_i)|^2$ , where

the turbulent velocity signal  $u = U - \bar{U}$  is divided in  $n$  blocks with 50% overlap. The spectrum of each of these parts is determined using FFT,  $\mathcal{F}(u_i)$ . These individual spectra are subsequently averaged over the  $n$  blocks. In order to acquire sufficient resolution to capture the low frequency fluctuations at the slowest operating point of the active grid at 1 Hz, the resolution should be well below 1 Hz. Therefore a block size of  $n_{\text{FFT}} = 2^{17}$  is used, which results in a resolution of  $df = f_s/n_{\text{FFT}} = 0.38$  Hz.  $E$  is normalized such that  $\int E(f) df = k = \overline{u'u'}$ . The spectra as shown in Figure 2.8 are shifted vertically such that they have a distance of a factor 100 to enhance the readability of the figure.

In the energy spectra clear and distinct peaks appear in the energy containing range. This shows that the periodically opening and closing holes of the active grid introduces large-scale perturbations. The peaks appear at frequencies which are in-



**Figure 2.8:** Energy spectra for the different grids. The spectra are vertically shifted by a factor of 100 for subsequent higher rotation frequencies to enhance the readability of the graphs. The vertical dotted lines indicate the range of the large-eddy turn-over frequency,  $\tau^{-1}$ , measured for the corresponding grid. Measured on the centerline 116 mm downstream of the grid.



teger multiples of  $f_r$ . With increasing  $f_r$  we observe that the peaks shift from below the large-eddy turn-over frequency,  $\tau^{-1}$ , i.e., the energy containing range, to well above  $\tau^{-1}$ , i.e., the inertial subrange. The peaks tend to decrease in magnitude when penetrating further into the inertial subrange. The value of  $\tau^{-1}$  depends on  $f_r$ . In Figure 2.8 we also indicate the minimal and maximal observed  $\tau^{-1}$  for the studied frequency range by two vertical dashed lines.

For the holes-holes case multiple peaks appear as expected due to the different jet frequencies induced by this grid. The most pronounced peak emerges at  $5f_r$ . With the chopper3 grid fewer peaks are introduced. Only at  $6f_r$  a strong peak is observed and at  $12f_r$  a smaller one. In case of the spiral-hex configuration many more peaks are observed. Besides the peak at  $5f_r$ , which corresponds to the jet frequency, also at  $6f_r$ ,  $10f_r$  and  $15f_r$  large peaks are observed. For the spiral-spiral grid also several peaks are visible next to the main one at  $5f_r$ . The pulsating jets just behind the grid undergo a complex nonlinear interaction which results not only in higher harmonics of the jet frequency, but also several other modes due to mode-mode interactions.

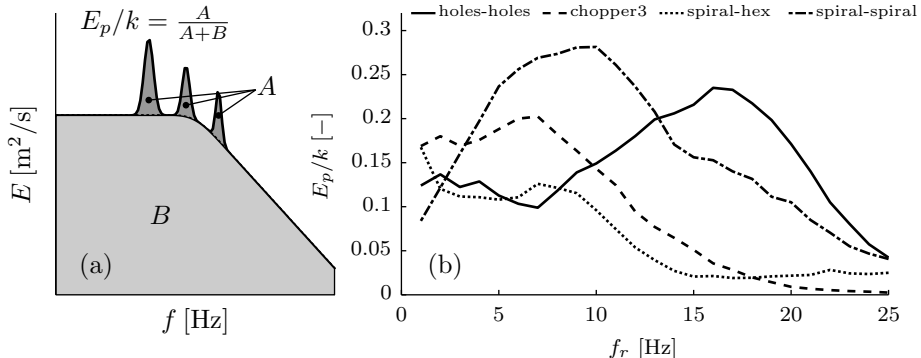
For all grids fluctuations are introduced mainly in the energy containing range. When  $f_r$  is increasing, the frequencies of the induced fluctuations move into the inertial subrange where their relative strength become lower. Besides the expected jet frequency also the frequency that corresponds with the oscillations in the porosity signal (Figure 2.1) appears in the spectrum.

### Energy contained in the peaks

To quantify the amount of energy that is contained in the fluctuations represented by the peaks, the approach of Cekli [15] is followed. The ‘frequency-selective’ part of the energy, denoted by  $E_p$ , is determined by the procedure graphically shown in Figure 2.9a. First, a base spectrum,  $E_b$ , without peaks is obtained that represents a filtered energy spectrum. This is done by median filtering the spectrum  $E$  with a filter width of 10 samples, which is larger than the typical width of a peak. Peaks with a value of at least 1.25 times the base spectrum are considered ( $E > 1.25E_b$ ) for  $E_p$ . This step is needed to select only significant peaks from  $E$  and to neglect the peaks in the noise-band present around  $E_b$ . A Gaussian curve fit is applied to the difference  $E - E_b$  to represent the sharp peaks in the spectrum. The integral of  $E - E_b$  for each peak is determined on the basis of the Gaussian fit. We also considered other numerical integration rules, e.g., based on a piecewise linear representation of the peaks. This gave rise to the same conclusions showing the robustness of the method.

In Figure 2.9b the energy contained in all peaks is plotted as function of  $f_r$  for the different grids. It can be seen that a significant fraction of the energy,  $k$ , is contained in the fluctuations introduced by all grids. For the chopper3 and spiral-hex cases a similar behavior is observed as in the experimental work of Cekli et al. [15] and the simulations of Kuczaj et al. [48]. At low frequency a high susceptibility to the forcing exists and at higher frequencies this susceptibility decreases. At low frequencies the flow is able to follow the time-dependent forcing, while at higher frequency this is no longer the case, due to the inertia of the flow, thereby filtering out the high-frequency forcing. For the holes-holes and spiral-spiral grids first a maximum is observed before the descending trend takes over.

The transition from high to low susceptibility to the forcing is expected when the forcing frequency is close to the inverse of the large-eddy turn-over time  $\tau^{-1}$  according



**Figure 2.9:** (a) Calculation of fraction of energy contained by the peaks graphically explained. (b) Fraction of energy contained by the peaks in the spectrum as function of the grid rotation frequency  $f_r$ .

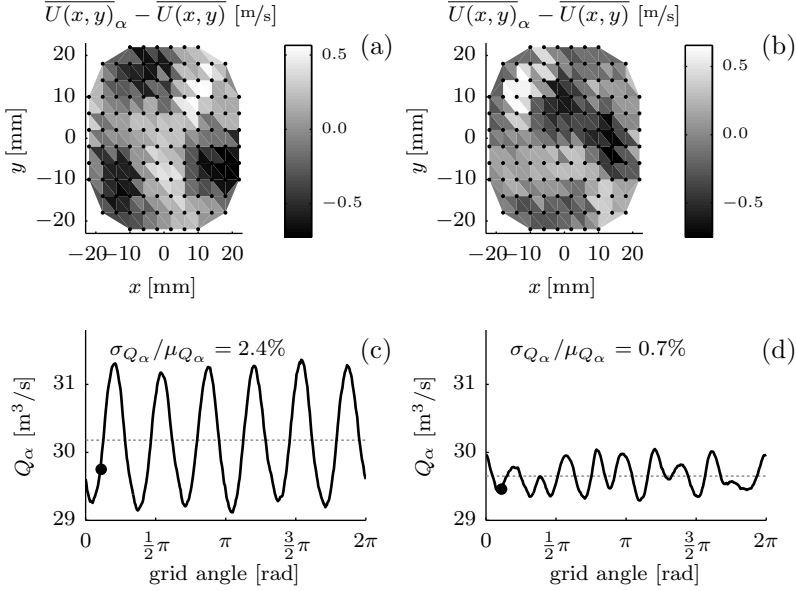
to literature [12, 15, 48, 49]. This is also observed in this work. When the frequencies of the main peaks are below  $\tau^{-1}$  a high  $E_p/k$  is observed and in the situation with peak frequencies above  $\tau^{-1}$ , the value of  $E_p/k$  is low. However, the precise onset of the transition cannot be quantified exactly as in [15]. This is most likely due to the presence of multiple peaks and the broad range of values for  $\tau^{-1}$ .

What becomes clear from the energy spectra and the quantification of the energy contained in the dominant peaks is that the frequency or the lengthscale of the introduced fluctuations can be tuned by setting  $f_r$ . A maximum response in  $E_p/k$  is found when the fluctuations are introduced in the energy containing range. When the fluctuations are introduced with a higher frequency, their contribution to the energy diminishes quickly with increasing frequency. This indicates that fluctuations in this frequency range get damped more quickly in the time it takes to travel from the grid to the measurement point.

Since this behaviour is observed in our experiments but also in the experiments of Cekli et al. even though scales are completely different, it is expected that this frequency dependent response can be scaled by a dimensionless number. An appropriate definition of the Strouhal number would be based on the rotation frequency of the grid,  $f_r$ , on the r.m.s. of the velocity,  $u'$  and on the integral lengthscale  $L$ . With  $L$  being determined by the mesh size of the grid it can be assumed to be constant.  $u'$  is expected to scale directly with the mean velocity,  $\bar{U}$ , so for similar  $St = f_r L / \bar{U}$  we expect similar frequency dependent response. Varying  $\bar{U}$  would be the first step for further research to test this hypothesis.

### 2.4.3 Structure of the fluctuations

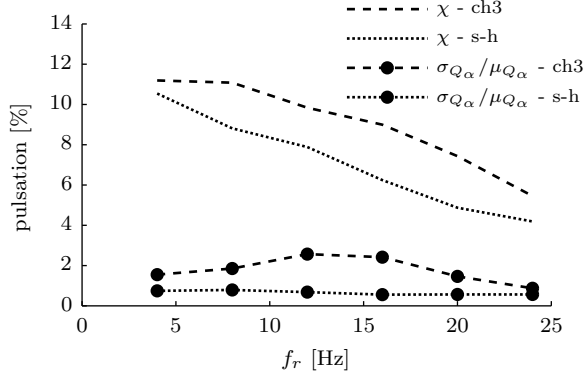
It is investigated to what extent the fluctuations discussed before are due to turbulent eddies or due to pulsation of the total volumetric flow rate. The volumetric flow rate is determined by obtaining the velocity field over the cross-section of the pipe as a function of the grid angle. Integrating over the cross-section yields the volumetric flow rate as a function of the grid angle, which ideally should be constant. We investigated the variation of this quantity to determine the level of pulsation induced by the active



**Figure 2.10:** (a,b) 2D plot of velocity deviation from the local mean,  $\overline{U(x,y)}_\alpha - \overline{U(x,y)}$ , at a grid angle of 0.35 rad for the chopper3 grid (a) and spiral-hex grid (b) @  $f_r = 16$  Hz. The locations where the measurements are taken are indicated by the grid of black dots. (c,d) Volumetric flow rate,  $Q_\alpha$ , as function of the grid angle,  $\alpha$ , for the (c) chopper3 grid and (d) spiral-hex grid @  $f_r = 16$  Hz obtained by integrating the grid-angle averaged velocity over the cross-section.

grid.

The signal of the optical encoder, as discussed in section 2.3.1, provides information about the position of the grid, through the rotation angle,  $\alpha$ . By using  $\alpha$  it is possible to calculate the mean velocity as function of the grid position. A traversing mechanism was used to scan the velocity in the plane 20 mm downstream of the tube exit. At the points indicated in Figure 2.10a and b the local conditionally averaged velocity,  $\overline{U(x,y)}_\alpha$ , is obtained for the chopper3 and spiral-hex grids at rotation frequencies 4, 8, 12, 16 and 24 Hz. Here, the averaging is over all values of the velocity recorded at instants at which the rotating disk was at an angle  $\alpha$ . Hence, the time-trace at position  $(x,y)$  was conditionally sampled and all occurrences at given  $\alpha$  were ensemble averaged. For the chopper3 case operated at 16 Hz the velocity distribution is shown in Figure 2.10a. Here the deviation from the local mean velocity,  $\overline{U(x,y)}_\alpha - \overline{U(x,y)}$ , at a particular grid angle is shown. This figure shows that there are mainly local fluctuations. The structure of the chopper3 grid is clearly present in the velocity distribution, where three regions with a positive value can be identified and three regions with a negative value. For the spiral-hex configuration operated at 16 Hz,  $\overline{U(x,y)}_\alpha - \overline{U(x,y)}$  is shown in Figure 2.10b. Also here regions with positive and negative value can be seen, but this pattern does not resemble the structure of the grid. The small-scale details of the grid are seen to be spread out and only the resulting large-scale structure is visible.



**Figure 2.11:** Pulsation of the volumetric flow rate (lines with marker) and the mean level of local pulsation (lines) as function of  $f_r$ . Here the level of pulsation is defined as the standard deviation divided by the mean of the phase-lock averaged signal.

To quantify the level of pulsation, the volumetric flow rate,  $Q_\alpha$ , is calculated by integrating  $\overline{U(x, y)}_\alpha$  over the cross-sectional area;  $Q_\alpha = \int_y \int_x \overline{U(x, y)}_\alpha dx dy$  by using the trapezoidal rule. In Figure 2.10c  $Q_\alpha$  is plotted for the chopper3 case operated at 16 Hz. The mean value of  $Q_\alpha$  of approximately  $30\text{m}^3/\text{hr}$  suggests that the flow is covered accurately by the number of measurement points used in traversing the domain. The clear period-six oscillation shows that there is a pulsation of the volumetric flow rate with a frequency that corresponds to the porosity as function of the grid position. This is not the case for the spiral-hex grid of which  $Q_\alpha$  is plotted in Figure 2.10d. Here at low  $f_r$  a period-ten oscillation and at higher  $f_r$  a period-five oscillation is observed in the volumetric flow rate, while a dominant period-fifteen oscillation is present in the porosity signal. This indicates that the measured pulsation is not directly caused by the low level of variation in porosity of the grid during a rotation.

In Figure 2.11 the level of the flow pulsation is shown as function of  $f_r$ . It is defined as the ratio of the standard deviation,  $\sigma_{Q_\alpha}$ , and the mean,  $\mu_{Q_\alpha}$ , of  $Q_\alpha$ , which are  $\mu_{Q_\alpha} = 1/2\pi \int Q_\alpha d\alpha$  and  $\sigma_{Q_\alpha}^2 = 1/2\pi \int (Q_\alpha - \mu_{Q_\alpha})^2 d\alpha$ . The maximum level is 2.5% for the chopper3 case and 0.8% for the spiral hex-case.

This level of pulsation of the volumetric flow-rate is small when compared to the mean level of fluctuation of the local conditionally averaged velocity, denoted as  $\chi$  and defined as:

$$\chi = \frac{1}{A} \int_y \int_x \frac{\sigma_{\overline{U_\alpha}}(x, y)}{\overline{U(x, y)}} dx dy, \text{ with} \quad (2.3)$$

$$\sigma_{\overline{U_\alpha}}^2(x, y) = \frac{1}{2\pi} \int \left( \overline{U(x, y)_\alpha} - \overline{U(x, y)} \right)^2 d\alpha$$

In Figure 2.11 both fluctuations of  $Q_\alpha$  and  $\chi$  are plotted as a function of  $f_r$  for the chopper3 and the spiral-hex configuration.

The fluctuation in the local mean velocity as function of the grid angle,  $\chi$ , is about ten times higher than the fluctuations in the volumetric flow rate,  $\sigma_{Q_\alpha}/\mu_{Q_\alpha}$ , in case

of the spiral-hex grid. For the chopper3 grid this ratio is about six. This underlines the fact that we have a flow with strong local fluctuations, while the total flow rate is virtual constant.

## 2.5 Application in premixed combustion

Distinct turbulent fluctuations can be introduced with control over their frequency, also into the inertial subrange, without creating a high level of pulsating flow. This gives rise to the question whether these scales could be of practical use. One application in which these fluctuations with specific scales could be exploited is the generation of flame surface in premixed combustion. According to Driscoll [27] the eddies that contribute to the wrinkling of the flame are in the order of 20-50% of the integral lengthscale and definitely not smaller than the flame front thickness, which is about 0.7 mm for atmospheric natural gas flames. The corresponding frequency can be estimated using  $\tau^{-1} = (l^2/\varepsilon)^{-1/3}$  assuming that these lengthscales are within the inertial subrange [82]. Based on the observed integral lengthscales and dissipation rates for the cold flow, the interesting frequency range for agitating the flow would be between 140-250 Hz, 160-400 Hz, 180-380 Hz and 280-550 Hz for resp. the spiral-hex, spiral-spiral, holes-holes and chopper3 grid. For all grids except the chopper3 it is possible to directly inject energy in this range, although most of the energy is in modes with lower frequency. For the chopper3 grid there is only a single dominant peak present in the spectrum at relatively low frequency. The fraction of the energy present in the different peaks decreases rapidly when a rotation frequency above, say, 20 Hz is used. Although there is limited energy present in the peaks for these operating frequencies, the specific modes are still over-represented when compared to regular turbulence, where a smooth spectrum is observed. It is therefore expected that the introduced fluctuations, even at higher operating frequency, will leave their mark on the turbulent flame front, since they are capable of directly wrinkling the flame. Furthermore, there is evidence that mixing can actually be enhanced when a narrow-banded forcing at scales in the inertial range is used [47]. Hence, the turbulence generated by the active grid appears a good candidate to be used to increase the mixing at appropriate scales and in that way the flame surface area to realize a more dense flame [79].

In this subsection the application of the compact active grid in a practical, industrial low-swirl burner [18] is investigated. The conventional turbulence generating blocking grid has been replaced by a compact active grid. The modifications of the active grid to make it compatible with a low-swirl burner are described in 2.5.1. Additional measurement methods to investigate the flame characteristics are described in 2.5.2. The properties of the flow and the flame under the influence of the active grid are presented in 2.5.3 and 2.5.4, respectively.

### 2.5.1 Adaptation of active grid for low-swirl burner

Low-swirl combustion has originally been introduced as an academic, freely propagating flame to investigate turbulent combustion [16]. Due to the low  $\text{NO}_x$ -emission characteristic and the simplicity of the design it has led to the development of a new type of burner [18]. The low-swirl stabilization mechanism is formed by a pipe

flow of premixed reactants with weak swirl created by either swirl vanes (fig 2.12b) or tangentially injected jets [16]. Upon exiting the tube the swirling flow creates a diverging flow pattern where the mean axial velocity decreases linearly with the downstream distance. This velocity decrease forms the stabilization mechanism for the freely propagating turbulent flame, which will be positioned at the location where the local flow velocity equals the turbulent flame speed. By using a low level of swirl the formation of a recirculation zone, which is characteristic for, more conventional, high-swirl stabilization, is avoided. This limits the residence time in the reaction zone and limits the formation of  $\text{NO}_x$  [40].

With a small alteration the active grid can be made compatible with a low-swirl burner. In Figure 2.12a an overview of the adapted configuration is shown. Inside the pipe a low-swirl generator is placed, which is depicted in more detail in Figure 2.12b. The dimensions of this low-swirl generator are set in accordance with the design rules of Cheng and Levinsky [17]. The swirl-number that characterizes the strength of the swirl is approximated to be 0.45 using [17]:

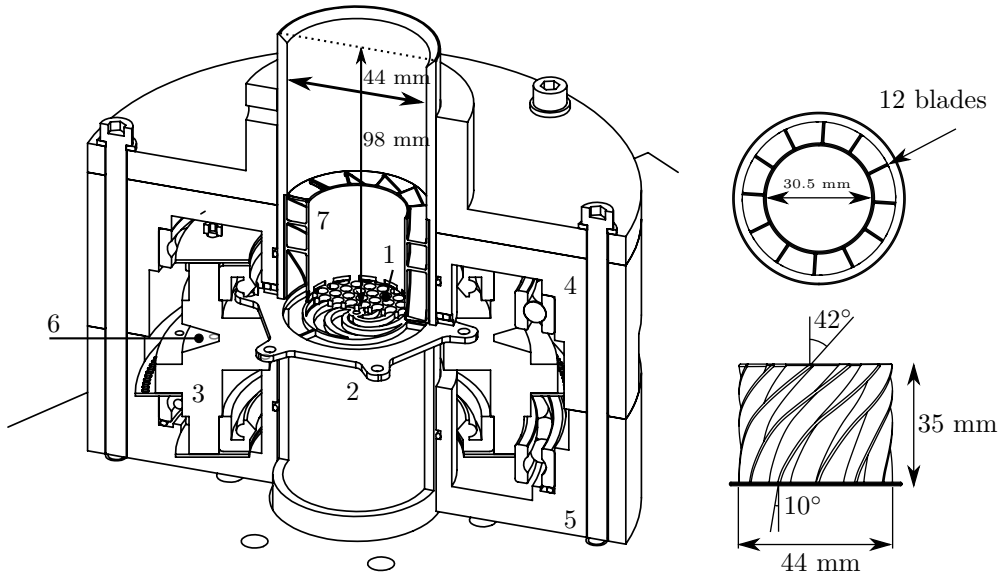
$$S = \frac{2}{3} \tan \alpha \frac{1 - R^3}{1 - R^2 + \left(m^2 (1/R^2 - 1)^2\right) R^2}.$$

Here  $R$  is the ratio between the radius of the central passage and the outer radius,  $\alpha$  is the exit angle and  $m$  is the ratio of the mass flows through the center and the swirling outer annulus, which is typically 0.8. The value of  $S$  is within the typical range of  $0.4 < S < 0.55$  needed for stable operation. The dimensions provided in Figure 2.12b completely define the geometry of the low-swirl generator. The same geometry is used for the experiments presented in chapter 4. The central passage normally contains a static perforated grid that balances the flow between the outer swirling flow and the central axial flow and produced turbulence in the central flow. In the current configuration this central blocking grid is replaced by the active grid. The active grid does not fill the entire cross-section of the pipe, but only covers the central passage. It is attached to the rotating construction by three 0.7 mm thick spokes. It is assumed that the effect of the spokes on the swirling flow is negligible as they are located upstream of the swirling vanes. The static disk is mounted inside the central passage by means of an interference fit.

### 2.5.1.1 Different grid patterns

Three different grid patterns have been used in combination with the low-swirl burner. In Figure 2.13 these are shown together with the porosity as function of the angular position of the grid. The spiral-spiral grid has been excluded from this set based on the high level of variation in open area, which will lead to pulsations of the mean flow.

The blockage ratio of the grid should be comparable with that of the conventional grid, which is typically between 0.6 and 0.81 [17]. The blockage ratio (1-porosity) is for all patterns in this range. Compared to the pipe-flow configuration some small changes were made in order to obtain a higher porosity for proper stabilization of a low-swirl flame. The holes-holes grid contains 3.5 mm diameter holes instead of 3.0 mm. The number of holes per circle also slightly differs. The chopper3 contains



(a) Construction of the driving mechanism of the active grid. 1 - static disk. 2 - rotating disk. 3 - rotor that is externally driven. 4,5 - housing. 6 - V-groove for external drive. 7 - low-swirl generator.

(b) Low-swirl generator with its dimensions.

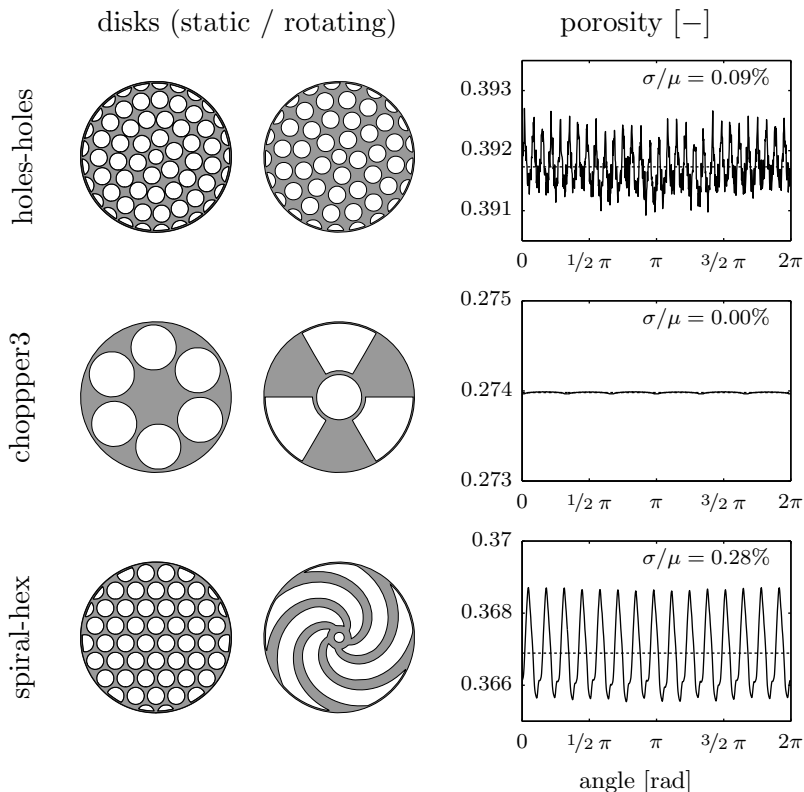
Figure 2.12

six 9.2 mm holes instead of 12 mm. For the spiral-hex pattern the diameter of holes and the width of the spiral-shaped slot is increased to 3.5 mm.

The induced jet frequencies remain the same for the chopper3 and the spiral-hex grid as there is no change in the number of openings. For the holes-holes grid the number of opening is changed. The jets formed by this grid will pulsate at  $5f_r$  for the inner circle of jets. This increases to  $11f_r$ ,  $16f_r$  and  $21f_r$  for each consecutive circle of jets. Note that this does not change the range of induced frequencies significantly.

## 2.5.2 Experimental methods for flame analysis

The flow downstream of the active grid is characterized by performing hot-wire measurements along the centerline downstream of the grid. This provides an evaluation of the mean velocity decrease, that forms the key for the low-swirl stabilization as well as a measure of the turbulent kinetic energy that the flame encounters. However, to characterize the flame itself additional experimental equipment is used. By means of OH-LIF the instantaneous flame front is captured. From these images statistical quantities like, mean reaction progress,  $\bar{c}$ , flame surface density,  $\Sigma$ , and the flame front curvature distribution can be obtained. In section 4.4.1 a detailed description is provided on the experimental procedure concerning OH-LIF. Settings that are specific for the experiments performed in combination with the active grid are mentioned here.



**Figure 2.13:** Different active grid configurations used in combination with the low-swirl burner. The level of variation in porosity is indicated by the ratio of the standard deviation,  $\sigma$ , and the mean,  $\mu$ , of the porosity signal.

First of all the operating frequency of the laser is different. The operating frequency of the laser is chosen such that the resulting images correspond with different grid angles of the grid. This means that the repetition rate of the laser should not be approximately the rotating frequency of the grid itself, since this results in OH-LIF images corresponding to one specific position of the grid, which is undesired. By using integer values (in Hz) for the laser repetition frequency,  $f_l$ , and the grid rotating frequency,  $f_r$ , that do not share a common factor (i.e.,  $\text{gcd}(f_l, f_r) = 1$ ), the OH-LIF images are samples at  $f_l$  different grid positions uniformly distributed over one rotation. Here  $f_l$  is set to 11 Hz, which satisfies the aforementioned condition for the investigated  $f_r = [2, 4, 6, \dots, 30]$  Hz, with the exception of 22 Hz. Since the laser is not actively synchronized with the rotation of the grid, the small inaccuracy in  $f_r$  leads to dispersion of the discrete grid positions over the measurement time. For each operating point 1000 frames are recorded, which is sufficient to obtain converged values of  $\bar{c}$  and a converged curvature distribution.

The data processing of the OH-LIF images requires a smoothing parameter,  $\sigma$ , to be set in order to suppress the influence of noise on the geometry of the detected



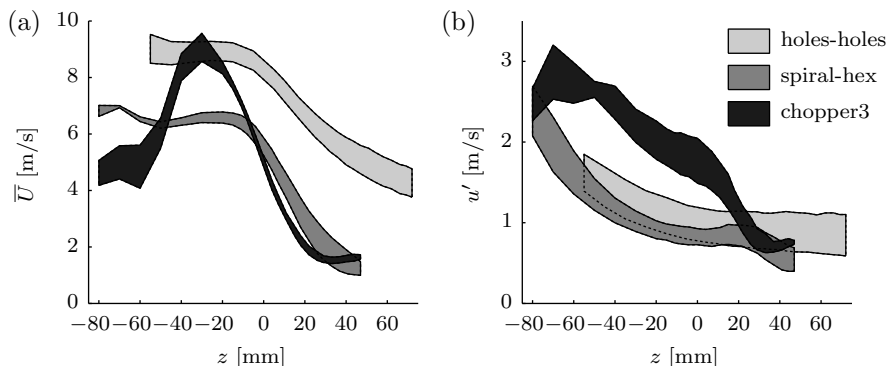
flame fronts. Here,  $\sigma$  is set to 6 px (or 0.63 mm) in the case of the full width measurements. For each operating point a zoomed measurement, centered around the centerline and the middle of the flame brush, is performed for a more detailed evaluation of the curvature distribution. For these measurements  $\sigma$  is set to 16 px (or 0.36 mm). The value of 16 px is needed for sufficient suppression of the noise in the images. By performing a spot-check of 500 samples from the final dataset the number of frames that contain unphysical edges is, with 95% certainty, below 1.3% and 2.1% for the zoomed and non-zoomed datasets, respectively. This is sufficient for determining the mean reaction progress and the flame surface density (FSD) since the errors introduced by the erroneous edges are certainly not greater than the percentage of erroneous frames. The effect of these frames on the curvature distribution is also very limited as demonstrated in [100].

Besides OH-LIF, also OH\*-chemiluminescence is employed to obtain more information about the time-dependent behavior of the flame. A photomultiplier tube (PMT, Thorlabs PMM01 with bandpass filter centered around 306 nm) is used to capture the chemiluminescence of the OH\*-radical, which is a measure for the heat release rate [58] and therefore related to the amount of flame surface. Although only a single volume integrated signal is obtained from the chemiluminescence of the flame, this signal captures fluctuations in time up to 20 kHz. The spectrum of a time trace of the PMT signal provides some qualitative insight at which frequencies the FSD is oscillating. The PMT is mounted perpendicular to the laser sheet and such that it captures the complete flame. The data is recorded at 50 kHz with the same data acquisition system as the hot-wire data. As the laser pulse itself is also detected by the PMT, removal of these spikes in the time trace is necessary. A median filtering operation with a width of 3 samples removes these spikes, while the shape of the frequency spectrum remains unaffected (in the interesting range).

The flow rate used for the experiments presented in this section is 46 m<sup>3</sup>/hr, resulting in a bulk velocity of 8.4 m/s. For the velocity measurements only air is used, while for the combusting case a mixture of air and Dutch natural gas is used at the same volumetric flow rate. The equivalence ratio,  $\phi$ , was set to 0.73, such that combustion takes place in the lean combustion regime and that the value is comparable with other atmospheric low-swirl flames, e.g., [20]. The thermal power of the flame is 33 kW based on the higher heating value of Dutch natural gas. The flow rate is higher compared to the pipe flow measurements. This higher flow rate affects the large-eddy turn-over time of the turbulence which determines at which frequency the flow should be forced in order to obtain a resonant-like behavior. However, this guideline is not ‘leading’ in these experiments. The focus here is to investigate the flame response on the turbulent flow with energy in distinct low-frequency modes, instead of the response to a flow with higher turbulent kinetic energy realized due to an optimal grid forcing.

### 2.5.3 Flow characteristics

The mean velocity and the standard deviation of the velocity along the centerline downstream of the grid are plotted in Figure 2.14. The values are obtained using an integration period of 10 s instead of 5 minutes as used in the pipe flow situation. The



**Figure 2.14:** The mean velocity,  $\bar{U}$ , (a) and the standard deviation of the turbulent velocity,  $u'$ , (b) as function of the downstream distance. The location where  $z = 0$  corresponds with the exit of the burner. Instead of drawing the lines for each  $f_r$ , the range of  $\bar{U}$  and  $u'$  is plotted for  $f_r = [2, 4, 6, \dots, 30]$  Hz.

value of  $\bar{U}$  does not deviate more than 0.5% from the mean velocity when recording for 5 minutes. For  $u'$  the deviation is less than 1%. These figures indicate that the integration time of 10 s is long enough for our purposes.

As the mean velocity is not affected much when varying  $f_r$ , only the range of  $\bar{U}$  is plotted. The figure clearly shows the typical linear decrease with downstream distance. The ‘steepness’ of the decrease is different for the various grids, with for the chopper3 case the most steep decrease and for the holes-holes case the least steep decrease. This results in a wider range in downstream distance where the linear decrease is located. Furthermore, the holes-holes case shows a higher value of  $\bar{U}$ . The stabilization of the flame for this grid will occur at a position further downstream compared to the other two grids. Besides differences in the dependence of  $\bar{U}$  on  $z$ , there is limited dependence on  $f_r$  as the bands are narrow. For all grids there is a consistent trend in which  $\bar{U}$  becomes lower when  $f_r$  increases. This can be explained by the same argument as presented in section 2.4.1, i.e., the opening and closing of the holes induces a flow resistance that increases with the frequency of this opening and closing. Even though there now is a bypass for the flow because of the presence of the low-swirl generator, the increased flow resistance results in a somewhat lower flow rate through the grid. However, this effect is small.

The standard deviation of the velocity signal,  $u'$ , is plotted in Figure 2.14b. Also here the range is plotted instead of each separate value to enhance the readability of the figure. It can be seen that there is more effect of  $f_r$  on  $u'$  than on  $\bar{U}$  as the bands are thicker. For all grids there is a trend whereby  $u'$  decreases with increasing  $f_r$ . The value of  $u'$  is similar for the holes-holes and spiral-hex grid, while for the chopper3 a significantly higher  $u'$  is observed, which is in accordance with the higher level of  $u'$  measured in the pipe flow situation. The difference in  $u'$  diminishes at the exit of the pipe.

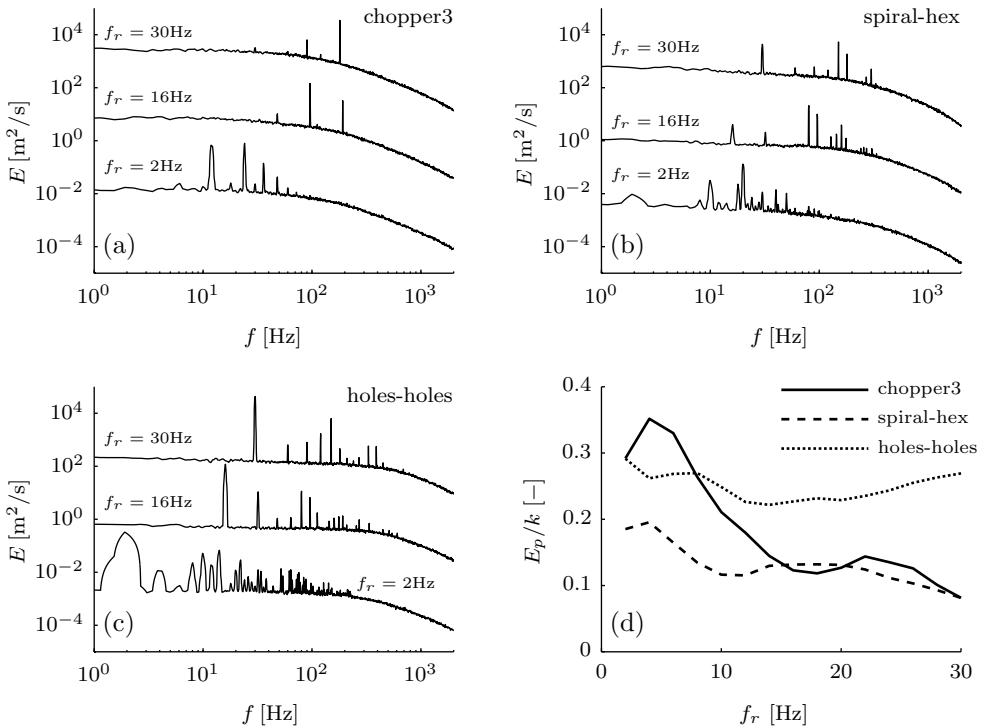
There is no indication that at a specific operating frequency the turbulence, measured by  $u'$ , is enhanced. The dissipation rate and other lengthscales are not evaluated since there is a high turbulent intensity in the interesting region close to the exit of

the pipe where the flame will stabilize. At such high intensities Taylor's hypothesis is not applicable and furthermore the assumption of isotropy in  $\varepsilon = 15\nu(\partial u/\partial x)^2$  is likely to be wrong due to the presence of swirl.

### 2.5.3.1 Energy spectra

At the exit of the burner and on the centerline the energy spectra of the velocity signals are obtained. For only three rotation frequencies the spectrum is plotted in Figure 2.15a-c for the different grid configurations. Similar peaks emerge from the base line spectrum at frequencies directly related to  $f_r$ . For the chopper3 grid strong peaks at  $3, 6$  and  $12f_r$  are visible. At  $5, 6$  and  $10f_r$  strong peaks are observed for the spiral-hex case. For the holes-holes grid a multitude of peaks can be identified. At almost all integer multiples of  $f_r$  in the range of 1 to 15 a peak is present.

For low  $f_r$  the peaks are again in the energy containing range of the spectrum and when  $f_r$  is increased and the peaks are located more into the inertial subrange, the height of these peaks is reduced. The holes-holes grids tend to have the onset of the



**Figure 2.15:** (a-c) Energy spectra for three grid rotation frequencies. For  $f_r = 16$  and  $30$  Hz the energy spectra are shifted vertically by a factor of  $500$  and  $500^2$  respectively to enhance the readability of the figure. (d) Energy in the peaks as function of the rotation frequency. All measurements are performed at the centerline at the burner exit ( $z = 0$ ).

inertial subrange at a higher frequency, which is a result of the higher mean velocity at the measurement location.

In Figure 2.15d the energy contained in the peaks is plotted versus  $f_r$ , which is of the same order as measured in the pipe flow configuration (see Figure 2.9). At low  $f_r$  the response is highest and is reduced for larger  $f_r$ , with the exception of the holes-holes case. Here,  $E_p/k$  is between 25-30% over the complete measured range. This might be due to the higher mean velocity. With a higher  $\bar{U}$  there is less time for the introduced fluctuations to decay or break up and as mentioned before the onset of the inertial subrange occurs at higher frequency, which renders the flow more susceptible to the introduced fluctuations.

## 2.5.4 Flame response due to active grid forcing

### 2.5.4.1 Shape of the flames

The shape of the low-swirl flame under the influence of the active-grid-generated turbulence can be seen in Figure 2.16 from the mean reaction progress,  $\bar{c}$ , for a limited number of rotation frequencies. Each grid appears to result in a different flame shape, while not much variation is observed as a function of the forcing frequency.

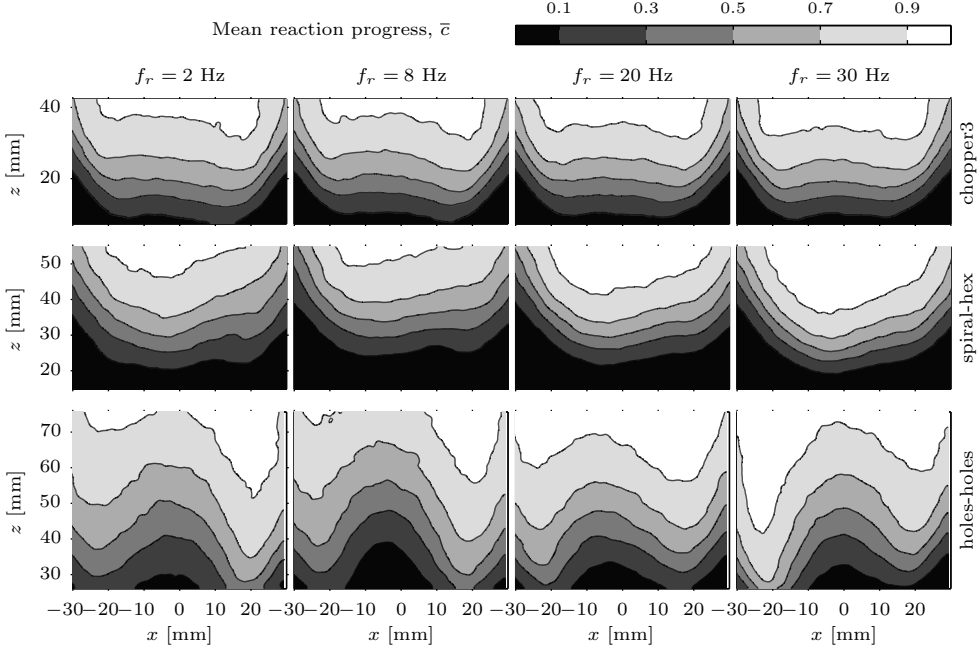
The flames corresponding with the holes-holes grid result in a poorly stabilized low-swirl flame. The high mean velocity on the centerline results in a ‘W’-shaped flame brush instead of a ‘cup’-shaped flame, which is more common for properly stabilized low-swirl flames. The cause of this improper stabilization is likely the non-uniform mean axial velocity profile in the center-section. A high velocity in the center, as confirmed by the hot-wire measurements, will be accompanied by a lower velocity at larger radius. According to the data presented in [20] the velocity profile is desired to be more like a slightly convex profile as function of the radial distance from the centerline.

Amongst the graphs with different  $f_r$  a closer inspection also reveals some variation. The flame brush in the center is made more compact when  $f_r$  is increased. The distance between the  $\bar{c} = 0.1$  and  $\bar{c} = 0.9$  isocontours is reduced from 28 to 24 mm for the chopper3 case and from 26 to 18 mm for the spiral-hex case. For the holes-holes case also a reduction in flame-brush thickness is observed along the centerline.

From the mean reaction progress it becomes clear that proper low-swirl stabilization is possible with the compact active grid as a central blocking grid. The holes-holes configuration renders a poor low-swirl flame due to the high velocity on the centerline, while the other two configurations provide properly stabilized low-swirl flames. The effect of  $f_r$  on the shape of the flame shows that the flame can be made more compact. To quantify whether the more compact flames are associated with an increased conversion rate, the amount of flame surface in the center region is assessed.

### 2.5.4.2 Turbulent flame speed

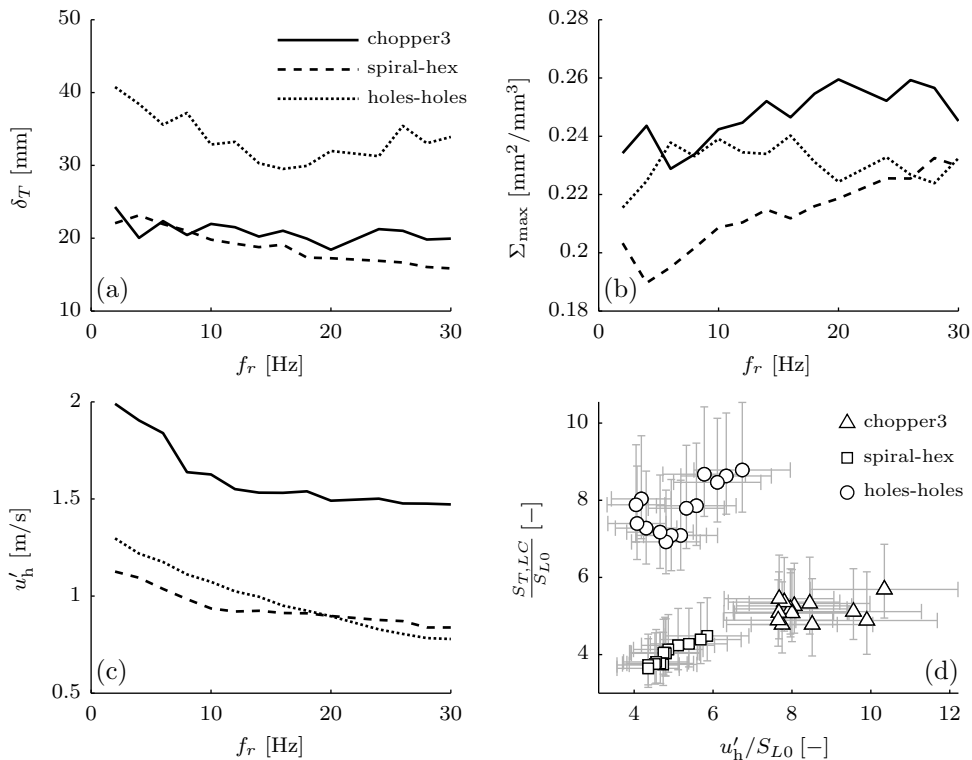
In order to assess the combustion rate at the center of the flame, the turbulent flame speed is determined based on the amount of flame surface. Here, the approach as discussed by Driscoll [27] is followed, where the local consumption speed,  $S_{T,LC}$  is used as definition for the turbulent flame speed.  $S_{T,LC}$  normalized by the laminar flame speed,  $S_{L0}$ , is given by  $S_{T,LC}/S_{L0} = I_0 \Sigma_{\max} \delta_T$ , where  $\Sigma_{\max}$  is the maximal flame surface density according to a fit  $\Sigma = 4 \Sigma_{\max} \bar{c} (1 - \bar{c})$  and  $\delta_T$  is the flame-brush



**Figure 2.16:** Mean reaction progress,  $\bar{c}$  of the low-swirl flames under influence of the active grid generated turbulence. Graphs in the same row correspond to the same grid configuration as indicated by the label on the right. Graphs forming a column corresponds to a single operating frequency,  $f_r$ , indicated at the top. The isocontours of  $\bar{c}$  correspond to the values 0.1 0.3, 0.5, 0.7 and 0.9.

thickness that follows from parameterizing  $\bar{c}$  as  $\bar{c} = \left[ 1 + \exp\left(\frac{-4(\eta - \eta_m)}{\delta_T}\right) \right]$ . In the latter expression  $\eta$  is the coordinate perpendicular to the flame brush and  $\eta_m$  is the value of  $\eta$  at which  $\bar{c} = 0.5$ . Both these fits are appropriate for flat flames [57, 87] as well as other premixed flames [27]. This fact is also expressed by the 95% confidence intervals for both fitted variables that are within 3.8% variation of the obtained value. For  $\delta_T$  it varies between 0.7% and 3.5% (2.2% on average) and for  $\Sigma_{\max}$  between 0.3% and 3.8% (1.0% on average). The region where the data for  $\Sigma$  and  $\bar{c}$  are extracted for the two fits is bounded by  $|x| < 5$  mm in order to study only that part of the flame that is solely affected by the grid turbulence.

In Figure 2.17 the quantities relevant for the turbulent flame speed are plotted as function of the grid rotation frequency for all three grid combinations. However, due to the poorly stabilized flame for the holes-holes grid, no conclusions can be drawn for this grid based on the quantities that are obtained in the center-section. For completeness the data itself is included in the graphs, but the following remarks do not apply to this grid. Figure 2.17a shows the dependency of  $\delta_T$  on  $f_r$ , which illustrates a similar trend as observed from the graphs of  $\bar{c}$ . The flame-brush thickness decreases with increasing grid rotation frequency. The maximum flame surface density,  $\Sigma_{\max}$ , plotted in Figure 2.17b, shows an increasing trend with increasing  $f_r$ . From both these quantities it follows that the flame brush is made more compact when  $f_r$  is increased,

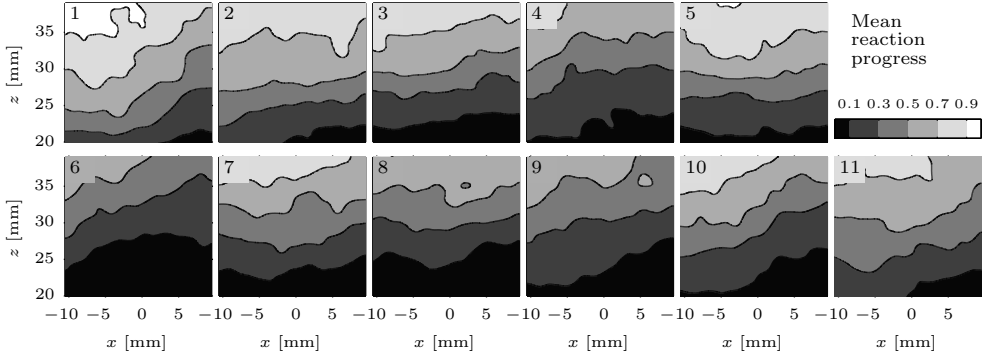


**Figure 2.17:** (a) Flame brush thickness,  $\delta_T$ , according to the fit  $\bar{c} = [1 + \exp(\frac{-4(\eta - \eta_m)}{\delta_T})]$ , (b) Maximal flame surface density,  $\Sigma_{\max}$ , according to the fit  $\Sigma = 4\Sigma_{\max}\bar{c}(1 - \bar{c})$ , (c) Estimated r.m.s. of the velocity fluctuations at the leading edge of the flame brush,  $u'_h$ . The leading edge of the flame brush is here defined where  $\bar{c} = 0.15$ . (d) The normalized consumption speed,  $S_{T,LC}/S_{L0}$  versus  $u'_h/S_{L0}$ . The errorbars indicate the uncertainty due to several factors, i.e., uncertainty in  $I_0$ ,  $u'_h$ ,  $\Sigma$  and  $\bar{c}$  and uncertainty as a result of the fitting of  $\Sigma_{\max}$  and  $\delta_T$  and also uncertainty in laminar flame speed,  $S_{L0}$ , due to the limited repeatability in the equivalence ratio, see section 4.4.4.

i.e., there is a higher flame surface density accompanied with a smaller space where the combustion takes place. To determine if also the combustion rate in the center is enhanced due to the active grid generated turbulence,  $S_{T,LC}/S_{L0}$  is plotted versus the level of turbulence at the leading edge of the flame front,  $u'_h$ , normalized by  $S_{L0}$ .

An estimate of the level of turbulence in the combusting flow from data obtained in the isothermal flow can be made by using the results from [20] where in both situations the velocity fluctuations are measured using PIV. Basically, the r.m.s. of the velocity fluctuations in the combusting flow,  $u'_h$ , is 16% higher than in the cold flow measured at the same location. Estimating  $u'_h$  from the isothermal flow data by an increase of 16%, results in no more than 11% deviation from their hot flow data in the region up to the flame.

Figure 2.17c shows  $u'_h$  versus  $f_r$ . It can be seen that in all cases  $u'_h$  decreases with increasing  $f_r$ , indicating that the flame encounters a lower level of turbulence for an increased operating frequency. In the graphs of Figure 2.17d the normalized



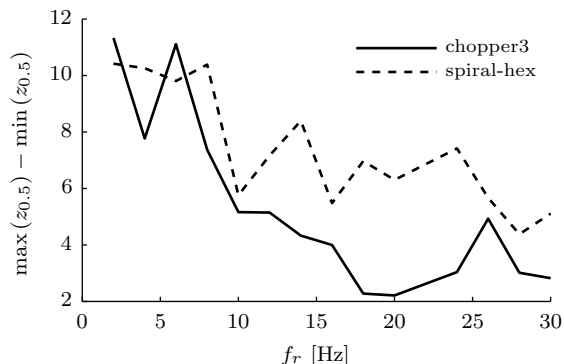
**Figure 2.18:** Phaselock averaged graphs of  $\bar{c}$  for the spiral-hex case operated at 6 Hz. Each graph displays  $\bar{c}$  obtained from OH-LIF images corresponding with a range of angular grid position,  $\alpha \in \left[\frac{2\pi}{11}(i-1), \frac{2\pi}{11}i\right]$ , where  $i$  is the number indicated in the top-left corner of the graph.

consumption speed is plotted versus  $u'_h/S_{L0}$ . The points corresponding to the spiral-hex configuration tend to form a linear relation between the increase in  $S_{T,LC}$  and the level of turbulence, which is characteristic for low-swirl combustion [20, 63, 87]. The points for the chopper3 grid form a plateau rather than a linear relation, suggesting a saturation in the increase of the consumption speed with increasing  $u'_h/S_{L0}$ . However, data of Cheng et al. [19] indicate that the characteristic linear trend persists up to  $u'_h/S_{L0} = 30$  in their low-swirl flames in isotropic turbulence.

In non of the cases an enhancement of the local consumption speed is realized by increasing the rotation frequency of the grid. The decreasing  $u'_h$  with increasing  $f_r$  is accompanied by a decrease in  $S_{T,LC}$ . Another observed effect is a more compact flame for increased  $f_r$  as indicated by the higher  $\Sigma_{\max}$  and smaller  $\delta_T$ . As this is in principal a desired property, it is worthwhile to investigate this more compact flame in more detail. A possible reason of the more compact flame at higher  $f_r$  can be the low-frequency transient behavior of the flame position, which is discussed in the next section.

### 2.5.4.3 Transient behavior of the flame

With the low operating frequency of the laser one is only able to obtain statistical information about the flame and no time resolved measurements can be performed. To gain some insight in the time-dependent behavior of the flame it is possible to use phaselock averaging. In Figure 2.18 the phaselock averaged results for  $\bar{c}$  for a single measurement (spiral-hex @ 6 Hz) is shown. There is considerable variation in the distribution of  $\bar{c}$  between the consecutive graphs. Although the number of OH-LIF images used to obtain a single phaselock-averaged graph is only 90, it was checked that the observed variation is not due to limited statistical convergence. Using half of the original 1000 OH-LIF images resulted in very similar variations of  $\bar{c}$  between the different phases. The isocontours are moving in the order of 10 mm, mainly vertically,



**Figure 2.19:** Variation in the phaselock averaged flame position measured by  $\max(z_{0.5}) - \min(z_{0.5})$ , where  $z_{0.5}$  represents the averaged value of  $z$  along the isocontour  $\bar{c} = 0.5$  in the center region of the flame, i.e.,  $|x| < 5$  mm.

within a single rotation of the grid for the illustrated case.

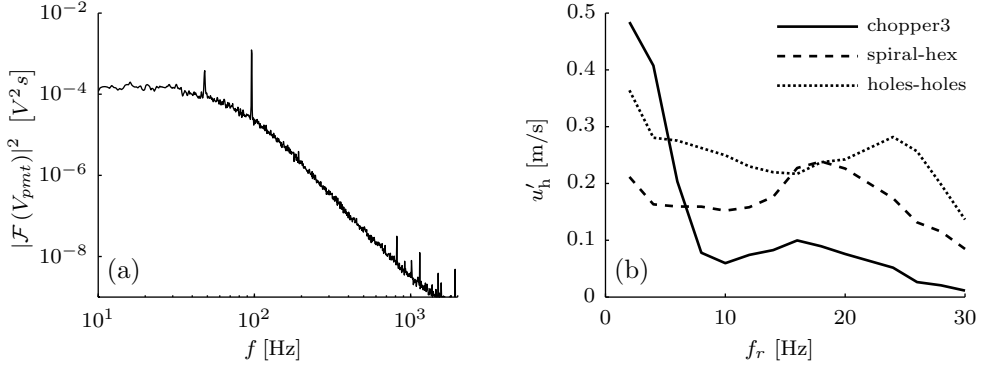
For the time-averaged mean, the transient variation of the flame position will cause a broadening of the flame brush and a lower flame surface density. The degree of variation in height of the flame brush is depending on the operating frequency of the grid. In Figure 2.19 this maximal variation is plotted versus  $f_r$ . At the lowest operating frequency the maximum variation in flame height is experienced, which is for both the spiral-hex and chopper3 case approximately 11 mm. For the spiral-hex grid it is reduced to 5 mm at 30 Hz and for the chopper3 grid to 3 mm.

The fluctuations introduced into the flow are designed to cause a limited pulsating mean flow. Nevertheless, the grid induced fluctuations are causing a deterministic variation in the height of the flame. The strength of this movement is related to the frequency of the velocity fluctuations. When the active grid is operated at the lowest frequency of 2 Hz, all peaks introduced into the energy spectrum are in the low-frequency, energy-containing range and a large movement of the flame brush is observed. When the velocity fluctuations are introduced more into the inertial subrange of the spectrum, which is the case for the chopper3 grid operated at 30 Hz, the flame is less capable to displace itself at these high frequencies. For the spiral-hex grid operated at 30 Hz there are still peaks in the energy containing range present, resulting in a larger movement of the flame brush compared to the chopper3 grid for the same  $f_r$ .

Using phaselock averaging to obtain time-dependent information provides only a limited frequency range. With 11 different ‘bins’ the maximal frequency that can be detected is  $5.5f_r$ , while the velocity fluctuations are introduced at frequencies ranging up to  $15f_r$ . For a more extensive investigation of the movement of the flame brush by phaselock averaging, the laser operating frequency should be set such that more angular grid positions are assessed and a higher number of total OH-LIF frames per operating frequency is required.

Variations in flame position will result in variations in the instantaneous heat release rate that is captured by the photo-multiplier tube. This time resolved, volume integrated heat release rate shows, similar to the spectra of the velocity signal, peaks





**Figure 2.20:** (a) Example energy spectrum of PMT voltage signal. (b) Ratio of energy in peaks to the total energy of the PMT voltage signal as function of the grid rotation frequency.

in its spectrum. The frequency of these peaks corresponds with frequency of peaks in the energy spectrum of the velocity signal. An example of such a spectrum is shown in Figure 2.20a for the chopper3 grid operated at 16 Hz. In Figure 2.20b the relative amount of ‘energy’ in the peaks for the PMT spectrum is shown as function of  $f_r$ . As the operating frequency of the grid is increased, the strength of the heat-release-rate fluctuations is reduced. This suggests that the trend of decreasing flame location oscillations with increasing  $f_r$  as observed in the phaselock averaged results remains valid also for higher frequencies than detectable with the phaselock method.

#### 2.5.4.4 Flame front curvature

We also studied the flame front curvature distribution and observed only a modest dependence on the rotation frequency. It does not reveal any preferential curvature that could have been induced by the specific turbulent fluctuations. The aspect of flame front curvature will therefore not be discussed in more detail.

## 2.6 Conclusion

The device that was presented in this chapter makes it possible to create an active grid in a small-size pipe flow. With only one moving part a grid with periodically opening perforations was created. By changing the set of disks that forms the grid a wide variety of flow-forcing is possible. This forcing could be used in small pipe flow of which a typical application could be premixed burners.

By using an active grid it is possible to create a large-scale time-dependent forcing which expresses itself by a range of peaks emerging in the energy spectrum. This forcing is realized without creating a large pulsation of the mean flow. The response, defined as the fraction of energy contained in these peaks, is high when the introduced scales have a timescale in the energy-containing range and decreases when these timescales are shorter and lie in the inertial regime. This observation is in agreement with literature. In between the two regions a maximum in this energy is observed for the holes-holes and spiral-spiral case, while for the other two configu-

rations no significant maximum can be distinguished. A resonant enhancement of the total turbulent kinetic energy or the mixing at the smallest scales expressed by the dissipation rate was not observed with any of the grids in the studied range of parameters. The velocity fluctuations  $u'$  are invariant or decreasing with increasing  $f_r$ , but in no case an increased  $u'$  was noticed. We also did not observe a minimum in the energy input rate, i.e., pressure drop, for the current design and parameter range.

A small modification makes the compact active grid compatible as a turbulence generator in a low-swirl burner. It has been verified that a proper low-swirl stabilization mechanism is realized based on the characteristic linear decrease of  $\bar{U}$  with downstream distance at the exit of the pipe. For the holes-holes grid a relatively high  $\bar{U}$  on the centerline resulted in a poorly stabilized flame, which illustrates the fact that a proper balance between the central axial flow and outer swirling flow is needed. The shape of the flames for the other two grids are in good agreement with conventional low-swirl flames. In the center of the flow for the swirling case the energy spectrum shows similar peaks indicating that turbulence here is dominated by the active grid. The amount of energy related to the grid is also in the same order as for the pipe flow. However, there is no enhancement of  $u'$  at any specific  $f_r$  and subsequently, there is no enhancement of the turbulent flame speed, as  $u'$  is the most dominant parameter in determining the turbulent flame speed. Using phaselock averaging it is shown that at low  $f_r$  there is substantial movement of the flame (in the order of 10 mm) and when  $f_r$  is increased the movement reduces. The fluctuations introduced by the compact active grid do not intensify the turbulence. It might be that part of these fluctuations are directly capable of wrinkling the flame front (as pointed out in the beginning of section 2.5) and increasing therefore the combustion rate, but this has not been confirmed by the experimental results. The relative amount of energy in these fluctuations is most likely too low to effectuate a significant change in the combustion rate.



# Chapter 3

## Fractal grids and premixed combustion

### Abstract

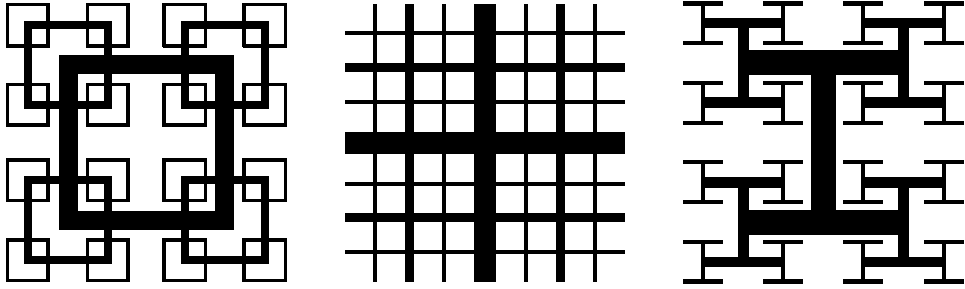
A variety of fractal grids is used to investigate how fractal-grid-generated turbulence affects the turbulent flame speed for premixed flames. The grids are placed inside a rectangular duct and a V-shaped flame is stabilized downstream of the duct, using a metal wire. This flame is characterized using OH-LIF. The turbulent flow is characterized by means of hot-wire anemometry. In total 24 grids containing variation in grid patterns, solidity and range of embedded scales were assessed. The results quantify in detail the relation between grid parameters and the turbulence downstream of the different grids. The increase in turbulent flame speed is found to be primarily related to the level of turbulent fluctuations and the time available for the turbulence to wrinkle the flame. The fractal grids provide efficiently much more intense turbulence compared to classical grids and therefore an increased turbulent flame speed. By increasing the range of embedded scales the turbulence is intensified. With respect to the reference case the turbulence intensity can be more than quadrupled and for the turbulent flame speed a more than doubling is observed. In practice the maximum usable increase in turbulence will be limited by the allowable transversal inhomogeneity in mean velocity that is accompanied with the inhomogeneous blockage of the fractal grid.

### 3.1 Introduction in fractal-grid-generated turbulence

There has been a lot of interest in fractal grids to generate turbulence. The extensive study on fractal-grid-generated turbulence of Hurst and Vassilicos [38] marks the

---

This chapter is based on publication:  
Enhancement of turbulent flame speed of V-shaped flames in fractal-grid-generated turbulence, A.A. Verbeek, P.A. Willems, G.G.M. Stoffels, B.J. Geurts and T.H. van der Meer, *submitted to Combustion and Flame*.



**Figure 3.1:** Three different families of fractal grids as introduced by Hurst and Vassilicos [38]. Left: ‘square’, middle: ‘cross’, right: ‘I’.

start of an intensification of interest in this field. However, already earlier, 3D fractal structures [94, 83] were placed in a flow to study whether the scaling behavior of the turbulence downstream of these object can be controlled by the lengthscales contained in of the objects. These experimental investigations led to simulation studies of flows with multi-scale forcing to resemble the flow downstream a fractal-object and to investigate how small-scale fluctuations are affected by the method of supplying energy [7, 50, 69].

In the work of Hurst and Vassilicos the flow downstream of a planar fractal object is investigated. They use two-dimensional grids to compare the decay and scaling characteristics against those of the well-established ‘classical’-grid turbulence. As the flow downstream of fractal grids is much more intense and scales differently with downstream distance, it has led to an increased interest from a physical point of view as well as from the point of practical applications.

Before going into detail about how fractal grids enhance the combustion rate of premixed flames, first we provide an overview of related previous work and some important observations. We briefly discuss the particular characteristics of fractal-grid-generated turbulence and possible applications that are reported in literature. Subsequently, we review the effect of fractal-grid-generated turbulence on combustion.

One of the main finding of Hurst and Vassilicos is the increase in turbulence intensity and Taylor-Reynolds number for the flow downstream of fractal grids compared to the situation using classical grids, but with the same blockage and effective mesh size. A more than doubling in turbulence intensity is reported for all three fractal patterns considered. These three different patterns are denoted as ‘square’, ‘cross’, and ‘I’. As an illustration Figure 3.1 shows these three patterns. The reported level of anisotropy for the cross and square grids is about  $u'/v' = 1.2$ , where  $u'$  and  $v'$  denote the standard deviation of the velocity fluctuations in longitudinal and transversal direction, respectively. This value is comparable to values found by others using active instead of static grids to elevate turbulence levels (Kang et al. [41] reports 1.16 and Makita [66]  $< 1.3$ ). With such level of anisotropy the turbulence is considered as ‘nearly isotropic’ as it is close to the values of  $0.95 < u'/v' < 1.05$  reported downstream classical grids [23]. The I-grid results in a higher level of anisotropy,  $u'/v' = 1.5$ . It should be noted that the values reported in [38] are obtained along the centerline.

The turbulence intensity along the centerline for fractal square grids develops rather differently compared to other grids. First the intensity builds up, reaches a

maximum and then starts to decay [38, 68]. Mazellier and Vassilicos [68] show that this dependence is self-similar for different realizations of the fractal-square pattern when the downstream distance is scaled by a ‘wake interaction’ length that is determined by the dimensions of the largest square, i.e.,  $L_0^2/t_0$  with  $L_0$  the length and  $t_0$  the thickness of the bars forming the square [68]. Experiments involving much smaller duct sizes show the universality of this scaling (e.g., [92, 93]). Gomes-Fernandes et al. [33] improved the ‘wake interaction’ theory by incorporating effects of the drag and free-stream turbulence.

Besides the increased turbulence intensity it was observed that the turbulence behind a fractal or multi-scale grid decays in a different fashion [38] when compared to regular grid turbulence. Especially, the flow downstream the square grids shows an interesting deviation from the dissipation anomaly, where the dissipation rate  $\varepsilon = C_\varepsilon u'^3/L$  with  $C_\varepsilon$  being a constant and  $L$  the integral lengthscale [82, 86]. Since the dissipation anomaly is seen as a cornerstone of homogeneous turbulence theory, the observed deviation has led to a series of papers, e.g., [45, 46, 98]. However, for practical applications the near field may be of greater importance, since the turbulent intensity is higher there. Valente and Vassilicos [99] investigated the decay close to the grid. The non-classical behavior ( $\varepsilon L/u'^3 = C_\varepsilon \neq \text{const.}$ ) for the fractal square grids is also observed for classical grids when looking close enough to the grid. In this previously unexplored region  $C_\varepsilon$  is not constant and turns out to be a function of  $\text{Re}_\lambda$ . Therefore, it was concluded that the ‘wake interaction theory’ is not restricted to multi-scale grids.

A reason why fractal grids result in higher turbulence levels can be found in the fact that the region where the turbulence is produced is elongated. A fractal grid acts as a ‘magnifying lens’ for the non-equilibrium region as stated by Valente and Vassilicos [99]. The production of turbulence is due to gradients in the mean flow, i.e.,  $\mathcal{P} = -\langle u_i u_j \rangle \frac{\partial \langle U_i \rangle}{\partial x_j}$  [82], where  $\mathcal{P}$  is the production term in the turbulent kinetic energy budget equation:  $\frac{Dk}{Dt} + \nabla \cdot \mathcal{T}' = \mathcal{P} - \varepsilon$  (here  $\frac{D}{Dt}$  is the mean flow  $\langle U_i \rangle$  material derivative). When using different lengthscales in the grid it is likely that gradients in the mean velocity are induced in a wider range compared to a regular grid. In [38]  $\mathcal{P}$  normalized by  $\varepsilon$  is shown along the centerline. The region before the decay of  $u'^2$  starts contains high values of  $\mathcal{P}/\varepsilon$  ( $> 5\%$ ) which is therefore denoted as the production region. Transverse inhomogeneities in the mean velocity just behind a grid result in the production of turbulence. For multi-scale grids these inhomogeneities persist for tens of integral lengthscales as shown by Nagata et al. [72]. The importance of the turbulence production due to transverse velocity gradients is further stressed by Nagata et al. [73] who assessed experimentally the turbulent kinetic energy budget of the flow behind a fractal square grid. Within the transversal plane at the downstream location where the turbulent intensity at the centerline is maximal and where the ‘decay’-region starts,  $\mathcal{P}/\varepsilon$  reaches values between 80-100%. This is much higher than the 10% reported at the centerline and indicates that there is still considerable turbulence production.

Especially the high level of turbulence in combination with a low pressure drop, implies that various applications can benefit from fractal-grid-generated turbulence. As fractal grids and also fractal orifices enhance the mixing downstream of these structures (shown for fractal grids in [53, 95] and for orifices in [70]) a wide range of application could benefit from this property: fractal fences to tailor boundary-layer

properties in environmental engineering [43], ventilation [104], fractal stirrers [22] and combustion [30, 32, 91, 93].

Flow metering that is often done by measuring the pressure drop over an inline orifice could efficiently use the low pressure drop associated with fractal structures. As shown by Abou El-Azm Aly et al. [2] for a given flow rate the pressure drop is lower when using fractal shaped orifices instead of standard circular orifices with the same cross-sectional area. This is further assessed by Nicolleau et al. [75] with more patterns. Numerical simulation of this kind of flow has been done by Van Melick and Geurts [70] and Zheng et al. [108].

Some other applications of fractal shapes in flows that can be found in literature are flows along fractal surfaces to resemble the flow over forests [42], noise reduction on air brakes of planes [54, 74] or effective flow conditioner before orifice flow metering device [67].

### 3.1.1 Fractal grids and combustion

In the field of combustion fractal grids have been used to increase turbulent intensities. Geipel et al. [30] use fractal cross grids in an opposed jet to increase the ratio of turbulent strain to mean flow strain. This solution is claimed to be preferable over using a larger separation between the two jets, since this introduces undesirable low frequency motion of the flow. Their fractal grids have a blockage in the range of 50-77% and an  $R_t$  between 0.5-0.74. Here,  $R_t$  is the ratio of the thickness of the bars used in consecutive iterations [38]. Only the fractal cross family was investigated. It is concluded that the blockage is primarily determining the level of turbulence and that the dimensions of the fractal grid can be used to ‘tailor’ the turbulence characteristics to some extent. An increase of more than 100% in turbulent intensity was observed compared to using only a perforated plate. However, it should be noted that the reference case contains only a perforated plate (45% blockage, 4 mm holes) while in the improved fractal case, the fractal grid is placed in addition to the perforated plate 10 mm downstream. The flow field is investigated in more detail by Goh et al. [32], showing that in fractal-grid-generated turbulence slightly larger structures are present. The effect on combustion is only assessed for the fractal case and this is not directly compared to the conventional situation.

A different study on the effect of fractal-grid-generated turbulence on combustion was performed by Soulopoulos et al. [92]. Here, a grid from the fractal square family (22% blockage,  $R_t = 0.4$ ) is used to generate turbulence upstream of a premixed V-shaped flame. An increase of 40% for the turbulent flame speed,  $S_T$ , is reported when using a fractal grid instead of a regular grid. This is accompanied with a wider flame angle and a thicker flame brush. Sponfeldner et al. [93] compared three other fractal square grids with a regular grid in the same V-shaped flame configuration. It is especially interesting to note that an increase in  $u'$  due to a decrease in  $R_t$  results in more increase of  $S_T$  than when a similar increase in  $u'$  is realized by an increase in the blockage ratio. This suggests that  $S_T$  is not solely a function of  $u'$ , but also of the structure of the turbulence. With only experiments for three fractal grids it can not be considered as a conclusive proof for this assertion.

Clearly, there is evidence that the combustion rate can be enhanced in premixed combustion by using fractal grids. It is also clear that turbulence is generated more efficiently (higher  $u'$  with similar pressure drop) [38]. However, it is not clear yet if the

enhancement is only due to an increase in  $u'$  or if fractal-grid-generated turbulence increases combustion even more.

In this work a wider range of grids is investigated to identify which parameters control the turbulent flame speed. A burner similar to the one used in Soulopoulos et al. [92], Sponfeldner et al. [93] is constructed in which a turbulent premixed V-shaped flame is stabilized. The turbulent flame speed is evaluated for two families of fractal grids, as well as classical grids for multiple blockage ratios. By incorporating similar grids as used by Sponfeldner et al. we confirm independently that the experimental results agree and increase thereby the reliability of the presented results. The range of blockage ratio is extended beyond values typical for wind-tunnel experiments and more toward the range used in, for example, low-swirl burners [102]. The results show that the flame speed is mainly related to the level of turbulence and the time available for the turbulence to wrinkle the flame. Furthermore, consistent trends are obtained that allow for prediction of the turbulent intensity downstream the various grids based on their design.

In the next section the experimental method to measure the turbulent flame speed is discussed. The different grids are presented in section 3.3. In section 3.4 measurement results concerning the flow are shown, whereas in section 3.5 the flame and its flame speed are discussed. Concluding remarks are made in section 3.6.

## 3.2 Measuring turbulent flame speed of a V-shaped flame

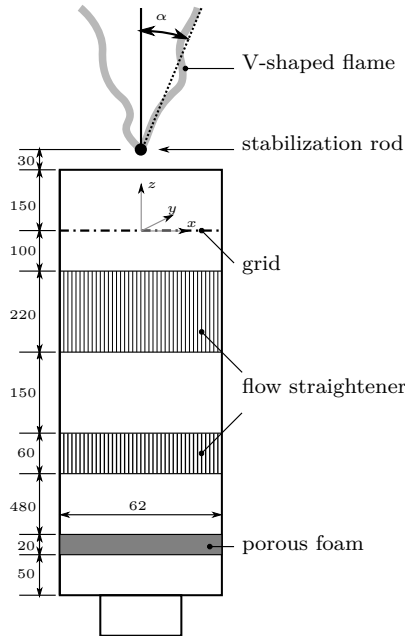
This section describes the experimental facility and the data reduction methods that are used to determine the turbulent flame speed in V-shaped flames.

### 3.2.1 Burner

The experimental facility that is adopted is similar to the one used by Sponfeldner et al. [93] and Soulopoulos et al. [92]. In Figure 3.2 a schematic view of the burner is shown. It consists of a square duct with an internal size of  $d = 62$  mm. There are several flow straightener sections to provide a uniform and axial flow upstream of the grid. The level of free-stream turbulence and the homogeneity was assessed at the position of the grid (with the grid not present) in the region  $-21 \text{ mm} \leq x, y \leq 21 \text{ mm}$ . The average turbulence intensity is 1.6% and the mean velocity varies by 2.8% as measured by the standard deviation of the local mean velocity across the assessed area. Although these figures are larger than typical for wind tunnel experiments (e.g.,  $< 0.1\%$  [23]) the free-stream turbulence is considered negligible compared to the turbulence levels that are generated by the different grids, including the classical ones. Furthermore, the level of free-stream turbulence is comparable with that of others [92, private communication with T. Sponfeldner].

The flow of air supplied to the setup is controlled by a mass-flow controller, while the natural gas flow is regulated by a proportional valve combined with a volume flow meter. In all experiments reported here the bulk velocity is set to  $U_0 = 4.4$  m/s, corresponding to a Reynolds number of  $\text{Re} = U_0 d / \nu = 1.8 \times 10^4$ . Here the kinematic viscosity is determined for air at  $20^\circ\text{C}$ , i.e.,  $\nu = 1.5 \times 10^{-5}$  m<sup>2</sup>/s [8]. For the measurements involving combustion the equivalence ratio is set to  $\phi = 0.72$ , which





**Figure 3.2:** Schematic view of the V-shaped flame burner. The dimensions provided are in mm. Note that the figure is not at scale.

corresponds to a power of 43 kW based on the higher heating value of Dutch natural gas. The accuracy of the flow rates is  $\pm 1.6\%$  for the air flow and  $\pm 2\%$  for the fuel supply. The fuel and air are mixed in a separate mixing section prior to the burner setup to ensure fully premixed conditions.

The (fractal) grid is located 150 mm upstream of the exit of the pipe. Its designs are discussed in detail in section 3.3. The flame is stabilized on a 2 mm rod positioned 180 mm downstream of the grid.

### 3.2.2 Measurement equipment

Characterization of the flow is done by means of hot-wire anemometry. A single straight probe of 0.9 mm length and 5  $\mu\text{m}$  diameter is used in combination with a DANTEC 90C10 CTA module. More details on the hot-wire equipment and the data processing can be found in [101]. A 2D traversing mechanism is used to position the wire in the  $xz$ -plane. Time traces are recorded for 10 s at 1000 Hz, which is sufficient to obtain statistically converged values of the mean,  $\bar{U}$ , and standard deviation,  $u'$  of the velocity. The values do not deviate more than 1% from values when measuring for five minutes.

The flame itself is characterized by OH-LIF measurements [28], which provide images of the instantaneous flame front. A laser-sheet with a height of 50 mm and a thickness below 0.2 mm is constructed in the  $xz$ -plane. The OH-fluorescence is captured using an 1024 $\times$ 1024 px ICCD camera. The laser system is operated at 10 Hz for 100 s which is sufficient to determine time-averaged statistics of the flame,

like mean reaction progress,  $\bar{c}$ , and flame surface density,  $\Sigma$ . The equipment and the flame front extraction procedure are identical as used in [102] and for a detailed description the reader is referred to this reference. However, certain details are specific for this work and will therefore be discussed briefly.

The flame front extraction procedure requires the user to provide a single parameter, which is the amount of Gaussian smoothing applied to the raw image. Here a compromise between detecting small features and suppressing noise is made. The value is set to 6 px (0.5 mm in physical space) for the experiments presented in section 3.5.1 and 3.5.2 where a large part of the flame is recorded. This setting provides edges properly resembling the flame front as was assessed by manual inspection. A random subset of 1000 frames out of the 24000 frames were inspected for spurious edges. Only 11 frames contained an error where the detected edge partly deviated from what would be considered the flame front by human interpretation. With 95% certainty the amount of erroneous frames in the complete dataset is below 1.8%. Therefore,  $\bar{c}$  and  $\Sigma$  are measured reliably as their error will definitely not be larger than this 1.8%. In subsection 3.5.3 the flame front curvature is assessed in a smaller interrogation area to achieve a higher accuracy. Here an additional convex lens ( $f = 100$  mm) is placed in front of the objective to provide additional magnification, resulting in a resolution of 51 px/mm instead of 12 px/mm. The smoothing parameter is decreased to 18 px (0.35 mm in physical space) which allows to capture curvatures up to  $3.5 \text{ mm}^{-1}$  with an error less than 10%. To determine this error synthetic black/white images were rendered representing OH-LIF data. The geometry of the black/white interface consists of alternating half-circles, such that the ‘flame front’ contains a single well-defined absolute curvature value, i.e., the inverse of the radius that was used. By using a smoothing factor of 18 px the mean value of the detected absolute curvature was found to be within 10% deviation of the exact value. Lower curvatures are detected more accurately.

### 3.2.3 Turbulent flame speed

The turbulent flame speed can be characterized in different ways. Lipatnikov and Chomiak [62] provide an overview of experimental data of the turbulent flame speed which shows a large scatter which is attributed to the lack of unique definition of the turbulent flame speed. Especially, the difference in flame geometry between various burner-types contributes to spread in experimental results. Furthermore, also the definitions and measurement technique for the same burner types differ, leading to a broad range of experimental outcome. It is not our intention to provide an improved definition of the turbulent flame speed, but to present the method that was selected to facilitate comparison with other similar V-shaped flames and to identify the dependence of the flame speed on fractal-grid-generated turbulence. An elaborate description of the definition and the calculation methods are provided for future reference.

Driscoll [27] lays out several approaches to define the turbulent flame speed. Here, the local consumption speed as well as the local displacement speed are used. The latter method is based on the flow velocity which is not accessible in the combusting case by hot-wire anemometry, but only by estimation from the non-burning flow measurements. As the flame will affect the velocity field the degree to which the cold-flow measurements represent the hot flow is questionable. Since both Sponfeldner

et al. [93] and Soulopoulos et al. [92] used this approach, it is considered to be adequate for comparing our measurement data with their results. To determine the difference in turbulent flame speed between the various grids the local consumption speed is more favorable as it does not rely on the mean flow field, but on the amount of flame surface, which can be measured more accurately. Note that the two different methods do not necessarily result in the same values as pointed out in [27, 62]. However, similar trends should be observed, which is what we rely upon in this paper.

First, the definition of the flame speeds are provided whereafter the method to determine the 3D flame surface density from 2D measurements is discussed. Finally, the definition of the interrogation area used to average the turbulent flame speed is discussed.

### 3.2.3.1 Definitions of turbulent flame speed

The local consumption speed is defined by:

$$S_{T,LC} = S_{L0} I_0 \int_{-\infty}^{\infty} \Sigma d\eta \quad (3.1)$$

Here,  $S_{L0}$  represents the unstretched laminar flame speed which is determined by the properties of the mixture. For all measurements reported here using  $\phi = 0.72$   $S_{L0}$  is 0.20 m/s based on laminar flame calculations performed with Cantera [34] and the GRI-mech 3.0 reaction mechanism [90]. The stretch factor,  $I_0$ , corrects for the difference in laminar flame speed between stretched and unstretched flamelets. It is valued close to unity for unit Lewis number, methane flames [56, 27].  $\Sigma$  is the amount of flame surface area per unit volume, which is measured using OH-LIF. Finally,  $\eta$  represents the coordinate perpendicular to the flame brush. To obtain an averaged value of  $S_{T,LC}$  over the measurement region, averaging is performed along the direction of the flame brush, which reduces the expression for the consumption speed to  $S_{T,LC} = S_{L0} I_0 \frac{A_T}{A_L}$ . Here  $A_T$  is the total amount of flame surface in the measurement region and  $A_L$  the amount of surface of the un wrinkled  $\bar{c} = 0.5$  isosurface. The actual measurement region is described in 3.2.3.3.

An alternative definition of the turbulent flame speed is in terms of the local displacement speed,  $S_{T,LD}$ , which is often used for V-shaped flames [27]. As the flame is stationary in the laboratory coordinates, the displacement speed of the flame brush with respect to the unburned mixture is given by:

$$S_{T,LD} = U \sin \alpha \quad (3.2)$$

Here,  $U$  is the mean velocity of the reactants and  $\alpha$  is the flame's half-angle. As both  $U$  and  $\alpha$  are not perfectly constant within the measurement area, averaged values are used. The half-angle is determined using a similar procedure as described in [93]. In the range of  $z \in [200, 220]$  mm a line is fitted through the isocontour of  $\bar{c} = 0.5$ , where  $\bar{c}$  is the mean reaction progress. Subsequently,  $\alpha$  is determined as the angle between this line and the  $z$ -axis. The velocity  $U$  is determined by averaging along the  $\bar{c} = 0.5$  isocontour using linear interpolation of the hot-wire measurements in the range of  $z \in [200, 220]$  mm.

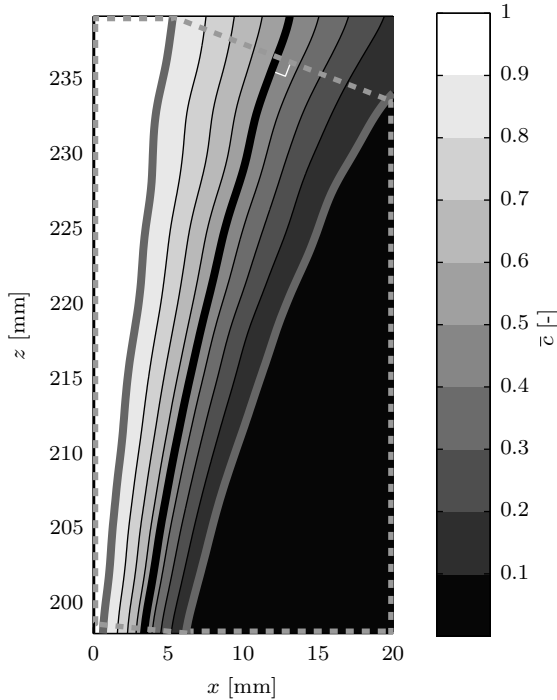
### 3.2.3.2 Estimating FSD from 2D measurements

For the flame surface only a 2D measurement is available. Hence, only the 2D equivalent of the flame surface density can be obtained. This is the ratio of flame front length per area,  $\Sigma_{2D}$ . To estimate the three dimensional flame surface density,  $\Sigma$ , the approach of Halter et al. [35] or Veynante et al. [103] can be used, where it is assumed that the wrinkling in the direction perpendicular to the measurement plane is similar to the wrinkling inside the measurement plane. This method provides the relation  $\Sigma_{2D} = \langle \cos \varphi \rangle \Sigma$ , where  $\varphi$  is the angle between the direction normal to the instantaneous 3D flame surface and the measurement plane. Here,  $\langle \rangle$  denotes the average in both space and time. The average value of  $\cos \varphi$  can be modeled using the variation of the measured flame front's normal direction. For our V-shaped flame it is expected that the fluctuations of the non-measured component of the normal vector behave similarly to the fluctuations of the measured component in the  $z$ -direction, analogous to Halter et al. [35]. In this case  $\langle \cos \varphi \rangle = (1 + \langle m_z^{2D} m_z^{2D} \rangle)^{-1/2}$ , with  $m_z^{2D}$  the  $z$ -component of the fluctuating part of the measured (2D) normal direction. For flames with a low level of turbulence the value of  $\langle \cos \varphi \rangle$  is close to one, while it was found to decrease for flames experiencing stronger turbulence. As an example, measurements for a classical cross grid with  $\sigma = 0.25$  showed that  $\langle \cos \varphi \rangle = 0.97$ , while for the fractal square grid with  $\sigma = 0.45$ ,  $R_t = 0.29$  a value  $\langle \cos \varphi \rangle = 0.83$  was obtained. The value of 0.83 is quite comparable with the ratio of 2D and 3D FSD reported in [103] for a turbulent round jet flame, found to be 0.85.

### 3.2.3.3 Spatial domain

The region used to determine the local consumption speed has an effect on the measured value itself. Therefore, a properly defined interrogation area is needed. Figure 3.3 shows a typical distribution of the mean reaction progress,  $\bar{c}$ . With the isocontour  $\bar{c} = 0.5$  considered as the center of the flame brush it is clear that not for every segment along this centerline the full width of the flame brush is captured. At the lower-left and upper-right corner this is most clear. The domain used for evaluation of the turbulent flame speed is enclosed by the gray dashed line. Only that part of the flame brush is included where in the direction perpendicular to the  $\bar{c} = 0.5$ -isocontour  $\bar{c}$  itself ranges from 0.1 to 0.9. In this way a bias toward unburned (or burned) is limited, while most of the measurement area can be used to extract flame speed information. Especially for flames in strong turbulence, which are accompanied with large values of  $\alpha$ , this is of importance.

The range in  $x$  of the measurement area is limited by the entrainment of the stagnant ambient air. To identify the degree of inhomogeneity, hot-wire measurements are performed in the transversal plane at  $z = 240$  mm for the situation in which no grid was installed. Up to  $x = 20$  mm the mean velocity is uniform within 10%, whereas for higher values of  $x$ , the velocity deficit quickly increases. Therefore, the region up to  $x = 20$  mm is considered as the free stream unaffected by the ambient air and used for analysis of the flame speed.



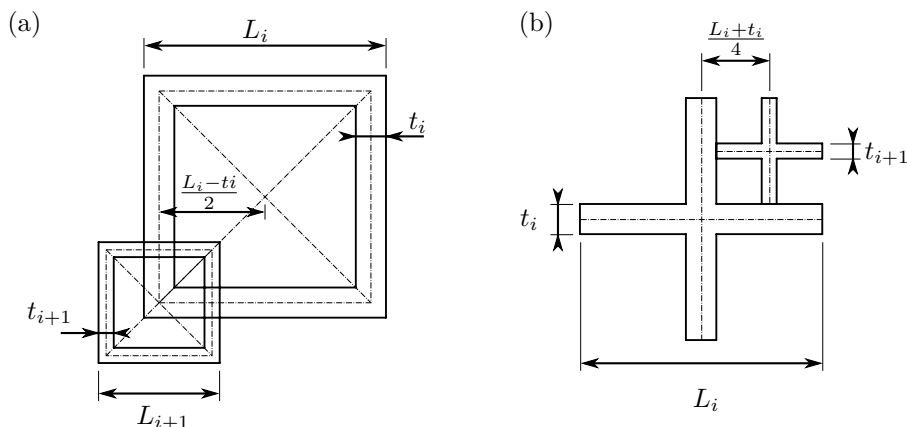
**Figure 3.3:** Example of the distribution of the mean reaction progress,  $\bar{c}$ , with the region used for averaging of the local consumption speed indicated by the dashed gray line. The isocontour  $\bar{c} = 0.5$  is indicated by the thick black line and the isocontours  $\bar{c} = 0.1$  and  $\bar{c} = 0.9$  are indicated by the thick gray lines.

### 3.3 Fractal-grid patterns

Most of the research on fractal grids adopts square-grids [33, 38, 52, 53, 54, 68, 73, 74, 86, 92, 93, 95, 97, 99]. These were also used by Soulopoulos and Sponfeldner. In addition some work has been performed with cross grids [30, 32, 38, 45, 46, 98] and these can also be incorporated in low-swirl burners as presented in [102]. In this work both square and cross grids are investigated for a wide range of blockage ratios, denoted by  $\sigma$ , and the ratio of bar-thicknesses,  $R_t$ .

#### 3.3.1 Definition of grids

For the definition of the fractal patterns we follow the design of Sponfeldner et al. [93] for the square grid and the design of Verbeek et al. [102] for the cross grids. Both designs are slightly different from what is used in the seminal work of Hurst and Vassilicos [38]. For the square grids the design of Sponfeldner is followed in order to directly compare with their results. In [102] a small alteration from the design of Hurst and Vassilicos [38] is made such that all openings in the cross grid are of the same size in order to obtain a more homogeneous flow.



**Figure 3.4:** Definition of fractal square and cross pattern.

In Figure 3.4 the definitions of the patterns are provided. To completely define a square grid five parameters should be defined. These are: the size of the largest square,  $L_0$ , the thickness of the largest square,  $t_0$ , the ratio of square size between iterations  $R_L = L_{i+1}/L_i$ , the ratio of square thickness between iterations  $R_t = t_{i+1}/t_i$  and the number of iterations,  $N$ . We limit ourselves by a number of constraints. The outer size of the grid should equal the duct-size,  $D$ .  $R_L$  is set to 0.5 and  $N = 3$  following [92, 93]. Using  $R_L = 0.5$  the fractal grid patterns is ‘space-filling’, which provides best homogeneity of the flow [38]. Fractal cross grids are described by four parameters which are  $L_0$ ,  $t_0$ ,  $R_t$  and  $N$ . The definition of the grid allows no freedom in  $R_L$ . Also for the cross grids the outer size of the grid is fixed, such that  $L_0 = D$  and furthermore  $N = 3$  following Verbeek et al. [102].

With two degrees of freedom for both grids the parametric variations studied here are expressed in terms of  $\sigma$  and  $R_t$ . Using  $\sigma$  is more convenient as it is a classical parameter to define turbulence-generating grids. And besides that it is more favorable than using a coupled variation in  $t_0$ ,  $R_t$  and  $L_0$  for the square grids.

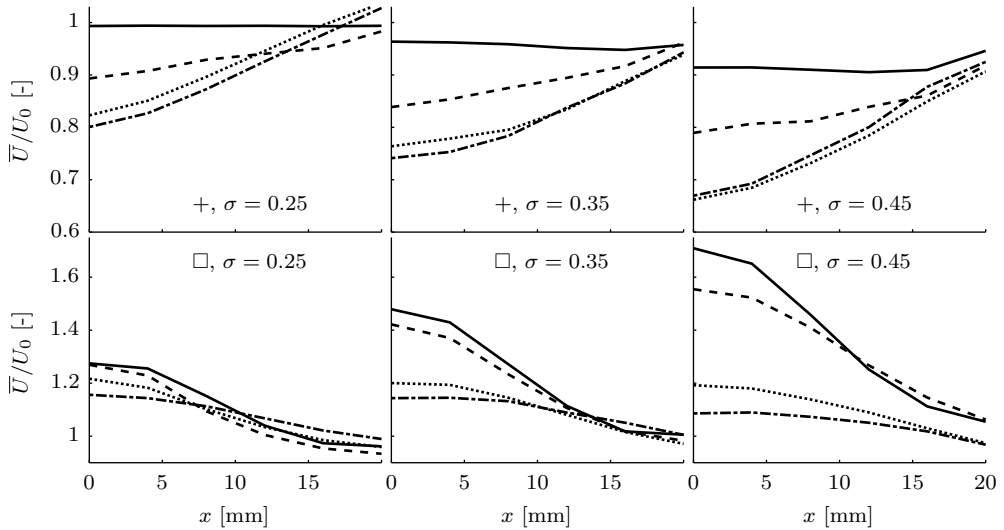
### 3.3.2 Range of parametric variation

In total 24 grids have been produced of which the properties are presented in Table 3.1.  $R_t$  is changed between 1 and 0.29 with two intermediate values of 0.7 and 0.4. For the one extreme,  $R_t = 1$ , the grid contains bars of the same thickness, while at the other extreme the difference in thickness is maximized under the constraint of a minimum thickness of 0.3 mm. This minimum feature size stems from the manufacturing limitations. The tolerance on the dimensions of the grids is below 0.05 mm.

The blockages are 25%, 35% and 45%. The lowest blockage corresponds to values used in earlier wind-tunnel research, e.g. [38], while the highest value is more in the direction of typical values for blockage grids used in low-swirl burners. Note that 45% is still lower than the 60-81% used in low-swirl combustion, but for fractal-grids with blockage ratios of 55% and higher the flame was positioned ahead of the stabilization rod for the flow rate and equivalence ratio considered.

#	marker	Grid type	$\sigma$ [-]	$R_t$ [-]	$L_0$ [mm]	$t_0$ [mm]	$z^*$ [m]
1	✧	square	0.25	0.29	38.2	3.7	0.32
2	★	square	0.25	0.40	37.8	2.9	0.42
3	◻	square	0.25	0.70	37.1	1.7	0.75
4	△	square	0.25	1.00	36.7	1.1	1.18
5	☆	square	0.35	0.29	39.3	5.3	0.22
6	☆	square	0.35	0.40	38.8	4.2	0.29
7	◻	square	0.35	0.70	37.8	2.4	0.51
8	△	square	0.35	1.00	37.2	1.6	0.80
9	☆	square	0.45	0.29	40.5	6.9	0.16
10	☆	square	0.45	0.40	39.8	5.5	0.21
11	◻	square	0.45	0.70	38.6	3.3	0.38
12	△	square	0.45	1.00	37.9	2.2	0.58
13	✧	cross	0.25	0.29	62	4.3	-
14	★	cross	0.25	0.40	62	3.4	-
15	■	cross	0.25	0.70	62	1.9	-
16	★	cross	0.35	0.29	62	6.3	-
17	★	cross	0.35	0.40	62	4.9	-
18	■	cross	0.35	0.70	62	2.8	-
19	★	cross	0.45	0.29	62	8.4	-
20	★	cross	0.45	0.40	62	6.6	-
21	■	cross	0.45	0.70	62	3.7	-
22	▲	cross/class.	0.25	1.00	62	1.2	-
23	▲	cross/class.	0.35	1.00	62	1.7	-
24	▲	cross/class.	0.45	1.00	62	2.3	-

**Table 3.1:** Overview of the parameters of the different grids used in this study. The cross grids with  $R_t = 1.00$  are also denoted as classical grids as these are not multi-scale.



**Figure 3.5:** Homogeneity of the velocity profile at  $z = 180$  mm for all grids, measured by the ratio of local mean velocity,  $\bar{U}$ , and the bulk velocity,  $U_0$ , which is 4.4 m/s. The blockage ratio,  $\sigma$ , is indicated in each sub graph, as well as the grid type. Here, + and  $\square$  denote the cross and square grids resp.. The different values of  $R_t$  are indicated by line style; solid:  $R_t = 1.0$ , dashed:  $R_t = 0.70$ , dotted:  $R_t = 0.40$ , and dash-dot:  $R_t = 0.29$ . Measurements are taken in the center of the flow, i.e.,  $y = 0$  mm.

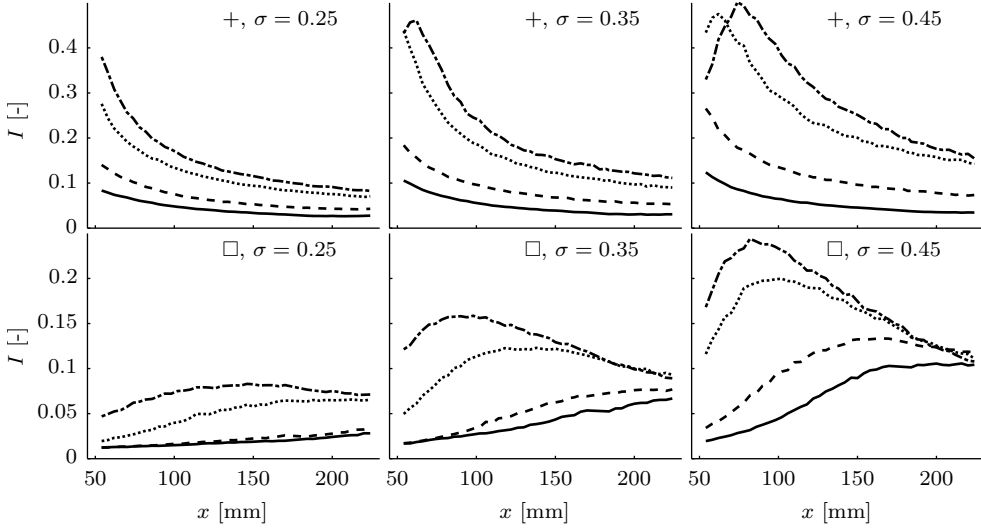
## 3.4 Flow response to fractal-grid-generated turbulence

For each grid the turbulence downstream of the grid is evaluated along the centerline of the burner as well as in the  $xz$ -plane at the level of the flame. Furthermore, the level of homogeneity in transverse direction is determined at 180 mm downstream of the grid corresponding with the rod location in the combustng situation.

### 3.4.1 Inhomogeneity of flow field

Due to the non-uniformity of the blockage for fractal grids, the mean velocity profile downstream is also inhomogeneous to a certain degree. In Figure 3.5 the ratio of the local mean velocity to the bulk velocity,  $\bar{U}/U_0$ , is plotted as function of the  $x$ -coordinate for all studied grids. Whereas for the classical grids almost a perfectly straight line is observed, all other grids show a deviation of more than 10%. For the cross grids  $\bar{U}$  is lower in the center and this deficit increases as  $R_t$  is decreased; a direct consequence of the increased non-uniformity of the grid. For the square grids the velocity deviation is opposite. Here, a higher velocity in the center is observed. Furthermore, the absolute deviation is larger compared to the cross grids, for similar  $\sigma$ . Increasing the blockage leads to an increase in non-uniformity. These results show that care should be taken when comparing the different flames as they are stabilized in different mean flow fields. For example, in the definition of the local consumption speed (eq. 3.1) an averaged value of the upstream velocity is supplied, while the effect





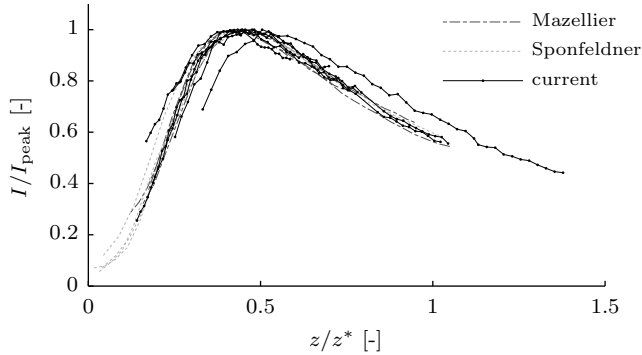
**Figure 3.6:** Turbulent intensity measured along the centerline for all 24 grids. The blockage ratio,  $\sigma$ , is indicated in each sub graph, as well as the grid type. Here, + and  $\square$  denote the cross and square grids resp.. The different values of  $R_t$  are indicated by line style; (—):  $R_t = 1.0$ , (---):  $R_t = 0.70$ , (.....):  $R_t = 0.40$ , and (----):  $R_t = 0.29$ .

of variation in  $\bar{U}$  is not incorporated.

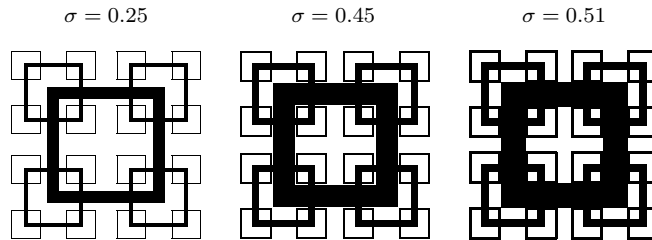
### 3.4.2 Level of turbulence

For each grid the turbulent intensity,  $I$ , along the centerline is plotted in Figure 3.6. A few trends are apparent. Increasing  $\sigma$  results in an increased  $I$  and also decreasing  $R_t$  results in a higher  $I$ . At the location of the rod,  $z = 180$  mm, the obtainable level of turbulence is comparable for square and cross grids. In order to further quantify the dependence of turbulence on the grid parameters each type of grid is assessed separately.

**Square grids** For the square grids Mazellier and Vassilicos [68] showed that the turbulent intensity,  $I = u'/\bar{U}$ , along the centerline first increases whereafter it decreases. Furthermore, the dependence of  $I$  on the downstream distance is self-similar when this distance is scaled with the ‘wake-interaction’ length  $z^*$ . For our grids we use  $z^* = (L_0 - t_0)^2/t_0$ , instead of  $z^* = L_0^2/t_0$  used for the square grids of Mazellier and Vassilicos. This adaptation is needed due to the difference in definition of  $L_0$  and  $t_0$  in the description of our grids. In Figure 3.7  $I/I_{\text{peak}}$  is plotted against  $z/z^*$  for the grids studied here as well as results obtained by [68] and [93]. For some grids with a large  $z^*$  the intensity peak is located further downstream than where the measurements were taken. These measurements are not shown in Figure 3.7. A good agreement is observed between all plotted cases, with one exception at  $\sigma = 0.45$ ,  $R_t = 0.29$ . For this grid, which has the lowest  $z^*$ , a slight deviation to higher  $z/z^*$  is observed. As the scaling of Mazellier and Vassilicos [68] is developed for low-blockage grids (they used 25%) it is expected that corrections may be needed at higher solidity. Increasing



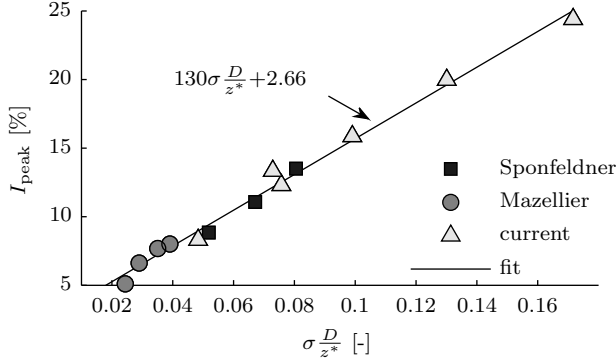
**Figure 3.7:** Normalized intensity plotted against normalized downstream distance according to the ‘wake interaction theory’ of [68]. Using this scaling the turbulence intensity along the centerline downstream of the grids collapse onto a single curve. One outlier can be identified which is shifted somewhat to the right. This line corresponds with the grid for  $\sigma = 0.45$  and  $R_t = 0.29$ . For comparison also work of others on fractal square grids is included [68, 93].



**Figure 3.8:** Three different square grids with different blockage ratio. For all grids  $R_t = 0.29$ . The right grid shows the case where  $\sigma$  cannot be further increased without overlap of the different iteration levels. Here part of the smallest squares coincides with the largest square and the grids do not comply to the initial pattern anymore.

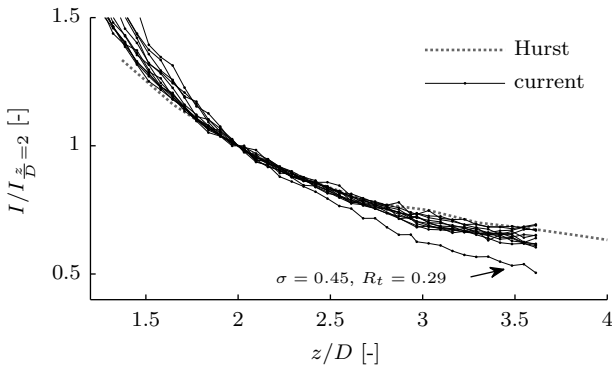
the blockage as done here goes in the direction to where the different iteration levels are overlapping with each other and the self-similarity between the square grids is lost. As an example Figure 3.8 shows the square grids with  $R_t = 0.29$  for  $\sigma = 0.25$ ,  $0.45$  and also for  $\sigma = 0.51$ , which is the limiting case where the squares of the smallest iteration partly coincide with those of the first iteration. The grid with  $R_t = 0.29$  and  $\sigma = 0.45$ , which is the outlier in Figure 3.7, is close to the limiting case for which Mazellier’s scaling appears to deviate.

For engineering purposes it is of interest to not only be able to predict the location of maximum intensity, but also the value of the maximum intensity itself. To that end the peak intensities for the square grids where a maximum in intensity is available are plotted. In Figure 3.9 the maximum intensity,  $I_{\text{peak}}$  is plotted versus  $\sigma \frac{D}{z^*}$ , where  $D$  is the duct size or the size of the test section in the wind-tunnel. Using this scaling a useful linear relation is obtained that predicts  $I_{\text{peak}}$  quite well for the flow downstream of the grids used in the V-shaped flame burner, i.e., the grids of Sponfeldner et al.

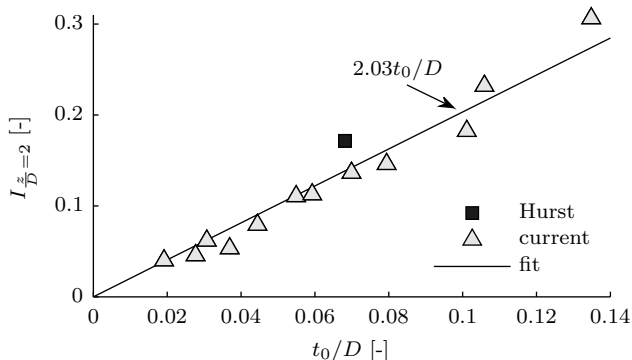


**Figure 3.9:** Maximum turbulence intensity downstream of the fractal square grid as function of the solidity,  $\sigma$ , size of the duct,  $D$ , and the wake interaction length,  $z^*$  in the form of  $\frac{\sigma D}{z^*}$ .

[93] and those presented here, but also for the grids of Mazellier and Vassilicos [68] who used a wind-tunnel with a cross-section several times larger (0.46 m and 0.91 m vs. 0.062 m here) . The fact that  $\sigma \frac{D}{z^*}$  provides an appropriate scaling parameter can be reasoned as follows. First of all, irrespective of the grid geometry an increase of  $\sigma$  will result in an increase in  $I$ . As there is more blockage, more energy (i.e., a higher pressure drop) is required to force the flow through the grid resulting in more turbulence [29]. Secondly,  $I_{\text{peak}}$  will be dependent on the distance from the grid as the turbulence intensity will have decreased as it is convected over a larger distance. In other words; a large  $z^*$  results in a lower  $I_{\text{peak}}$ . This distance can be made dimensionless by scaling it with the width of the channel, which provides a good linear fit.



**Figure 3.10:** Normalized turbulence intensity plotted against the normalized downstream distance. Here  $I$  is normalized by  $I$  measured at  $z = 2D$ , where  $D$  is the duct size. The data for the cross grid with three iterations of [38] (labeled  $\beta_L = 0.00$ ) is included for comparison.



**Figure 3.11:** Turbulence intensity at the centerline at a downstream distance of  $z = 2D$  behind a cross grid as function of  $t_0/D$ . The trend line is fitted using only the data points of the measurements presented here.

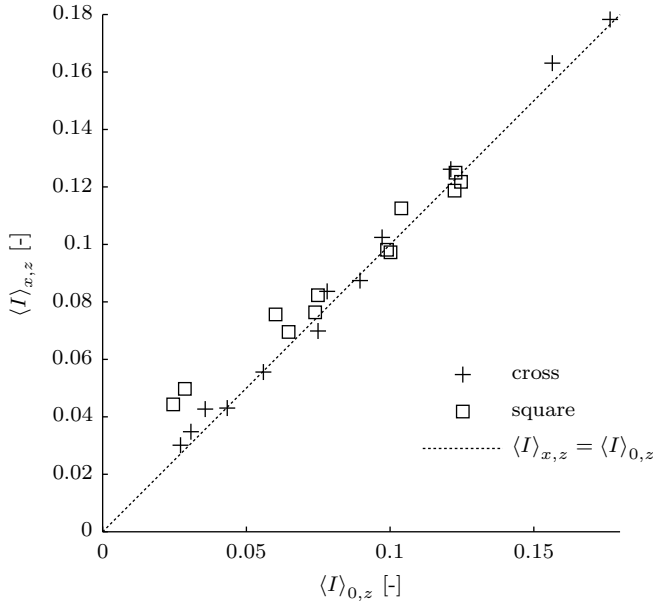
**Cross grids** For the cross grids the development of the turbulent intensity along the centerline is also dependent on the grid parameters. In Figure 3.6 the intensity is plotted for all cross grids. Note that here no peak is present as the measurements are not performed downstream of an open area as is the case for the square grids, but downstream of an obstacle.

The shape of the curves for the different grids are very similar and this can be shown more clearly when  $I$  is scaled by, for example, the value of  $I$  at two duct-sizes downstream of the grid. Figure 3.10 shows the result for this normalization as well as the results from Hurst and Vassilicos [38] obtained in a much larger wind tunnel using a similar grid. Within 10% the lines overlap in the region  $z > 2D$ , where it is most useful to be able to predict the turbulence. One exception here is grid #19 with  $\sigma = 0.45$  and  $R_t = 0.29$ , an extreme grid with respect to both  $\sigma$  and  $R_t$ .

The absolute value of the turbulence is quite well predicted in terms of  $t_0/D$  as shown in Figure 3.11. The result of Hurst for a similar grid in a  $D = 0.91$  m wind-tunnel are included as well, which agree fairly well with our obtained results. The deviation from the trend line is 18%, while the average deviation of our own data with respect to the trend line is 14%. This illustrates the validity of the scaling for different cross grids of different sizes.

Why is the turbulence intensity mainly controlled by the size of the largest cross,  $t_0$ ? For cross grids  $t_0$  is determined by both  $\sigma$  and  $R_t$ . Increasing  $\sigma$  results in an increased thickness of all bars in the grid, including  $t_0$ . The higher solidity is accompanied by an increase in turbulence. The other parameter that is varied,  $R_t$ , also affects  $t_0$ . Using a lower  $R_t$  results in a higher  $t_0$  and as could be seen from Figure 3.6 decreasing  $R_t$  provides an intensified turbulence at the centerline. Apparently, both these effects are captured by  $t_0$ .

**Off centerline** So far only the turbulence intensity along the centerline was discussed. With the flame located out-of-center the question arises whether or not the turbulence intensity along the centerline is a proper measure for the turbulence intensity that the flame encounters. In the region  $0 \leq x \leq 20$  mm and  $180 \leq z \leq 224$  mm,

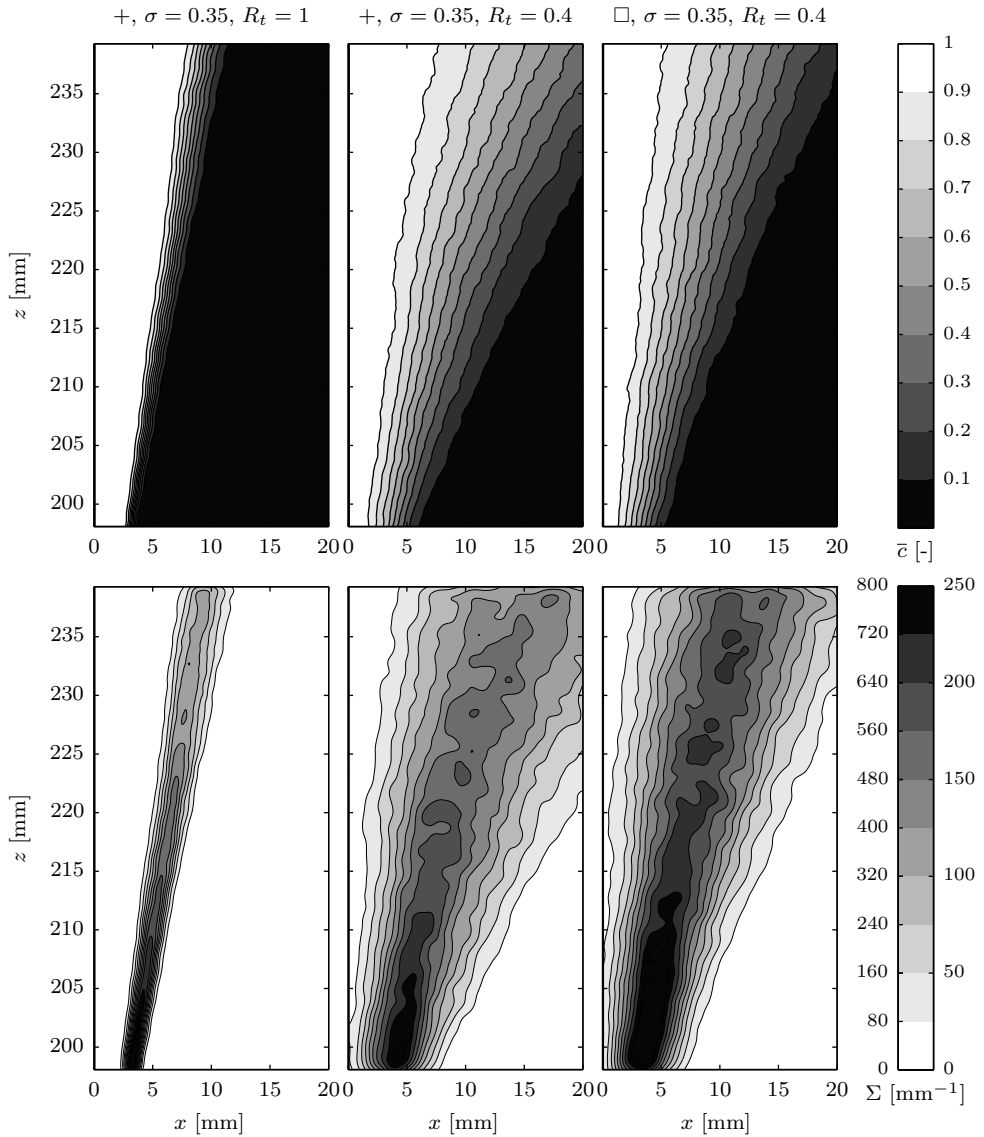


**Figure 3.12:** Relation between average turbulence intensity measured along the centerline,  $\langle I \rangle_{0,z}$ , and measured off-center in the range  $0 \leq x \leq 20$  mm,  $\langle I \rangle_{x,z}$ . For both quantities the range in axial direction is  $180 \leq z \leq 224$  mm.

which is where the flame stabilizes, hot-wire measurements are performed on a uniform grid of points using a spacing of 4 mm in both directions. This enables to compare the average turbulence intensity in the flame region with the average intensity along the centerline. Figure 3.12 shows the mean of  $I$  in the aforementioned region,  $\langle I \rangle_{x,z}$ , plotted against  $I$  averaged along the centerline for the same range in  $z$ ,  $\langle I \rangle_{0,z}$ . The graph shows that there is a high correlation between the two quantities as the points are all located closely to the diagonal. For the square grids there is more deviation, which is not unexpected due to the higher level of inhomogeneity in the flow for these grids. Although there is in general a good agreement, care should be taken for low values as there the relative error is as large as 45%. The relative difference is on average 6% (max 16%) for the cross grids and 12% (max 45%) for the square grids.

**Conclusion cold flow** The study of the turbulence downstream of the various grids revealed important features that can be used for designing fractal grids in practical applications. By applying a fractal grid, either a square or a cross grid, the level of turbulence is significantly enhanced, up to several times, compared to classical grids. This level of turbulence downstream of these grids can be predicted quite well using only grid parameters. It is shown that these relations predict also the value of the turbulence intensity downstream similar grids of much larger dimension. And perhaps most importantly, the turbulence encountered away from the centerline is well represented by the centerline values.

### 3.4. Flow response to fractal-grid-generated turbulence



**Figure 3.13:** Mean reaction progress (top row) and flame surface density (bottom row) for three different grids as denoted above the graphs. Two different gray-scales are used for the flame surface density as the maximum value is significantly different. The left graph corresponds with the left scale on the color bar, while the middle and right graph correspond to the right scale.

### 3.5 Flame response to fractal-grid-generated turbulence

For each of the 24 grids the resulting V-shaped flame is characterized by capturing 1000 OH-LIF images in the  $xz$ -plane. These instantaneous images are subsequently processed using an edge-detection algorithm [100]. Figure 3.13 shows the results for some grids with  $\sigma = 0.35$  to illustrate certain differences between the flames. The left graphs show the result for the classical grid, while the middle and right correspond to the  $R_t = 0.4$  cross and square grid, respectively. Two differences that are clearly visible are the more slanted flame and the wider flame-brush when using fractal grids. From the lower graphs it can be seen that using fractal grids results in lower values of  $\Sigma$ , while the region where the flame surface is located is expanded. Both these effects (lower  $\Sigma$  and large flame brush) have an opposite effect on the turbulent flame speed as is clear from the definition of the consumption speed, eq. 3.1. In the sequel we quantify the combined effect in terms of the consumption speed. However, first we verify that the experimental results agree with those of [92, 93] by comparing the turbulent flame speed in terms of the displacement speed, eq 3.2.

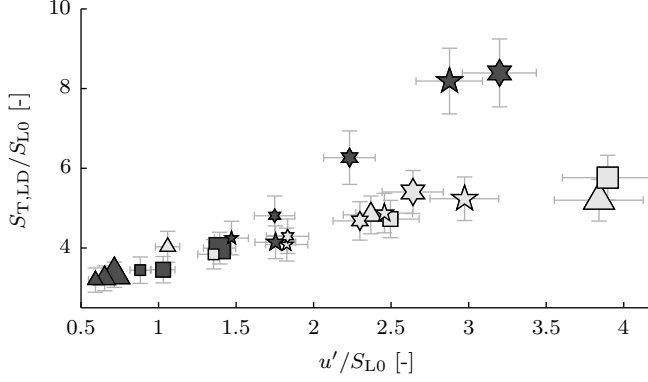
#### 3.5.1 Comparison of flame speed with data of others

From the orientation of the flame brush and the mean flow velocity the local displacement speed is determined. For each grid the normalized value is plotted versus the normalized level of turbulence in Figure 3.14 showing different trends for the two grid types. In all cases the turbulent flame speed is increased by using fractal grids. However, the increase in flame speed for a similar increase in turbulence (measured by  $u'$  averaged along the  $\bar{c} = 0.5$  isocontour) is much higher when using cross grids. The dark points, corresponding to cross grids, tend to form a much steeper curve than the light points of the square grids.

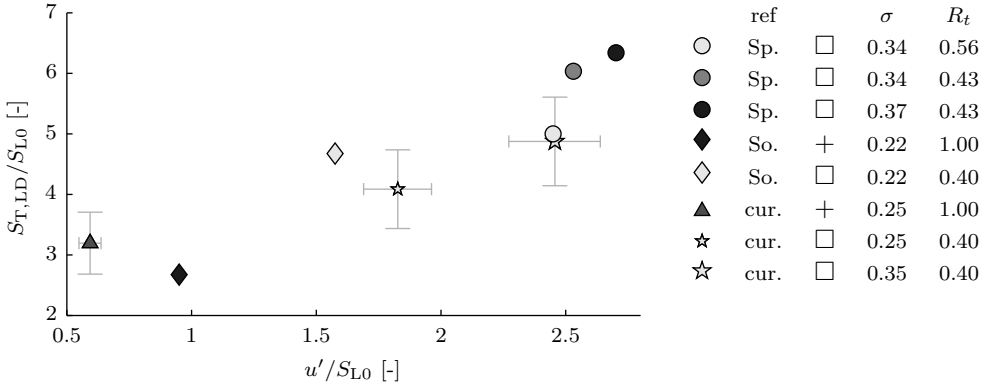
Due to the high level of inhomogeneity of the mean flow, especially for the high solidity grid, the shape of the flame is affected. The square grids, with a higher velocity in the center result in a significantly lower flame angle. The applicability of the approximation for the displacement speed is therefore considered questionable in this regime.

The local displacement speed for the classical and square grids that are comparable with those used by Sponfeldner and Soulopoulos are separately shown in Figure 3.15 together with their data. The results are quite similar given slight differences in experimental setup and grids. In the work of Soulopoulos the stabilization rod is positioned 250 mm downstream of the grid instead of 180 mm. Furthermore, Sponfeldner and Soulopoulos both used an equivalence ratio of  $\phi = 0.7$ , while in the present work  $\phi = 0.72$  is used. The results do nevertheless overlap reasonably well. Consider, for example, the grid with  $\sigma = 0.35$ ,  $R_t = 0.4$  (★) with the grid of Sponfeldner at  $\sigma = 0.34$ ,  $R_t = 0.43$  (●). Since both measurements have similar uncertainties the values do not significantly differ from each other. This also holds for the values corresponding to the grid  $\sigma = 0.24$ ,  $R_t = 0.40$  (★) and the grid of Soulopoulos at  $\sigma = 0.22$ ,  $R_t = 0.40$  (◇).

The uncertainty of the values in Figure 3.14 and 3.15 stems from several factors. For  $u'/S_{L0}$  the uncertainty is dictated by the statistical convergence of  $u'$  (95% con-

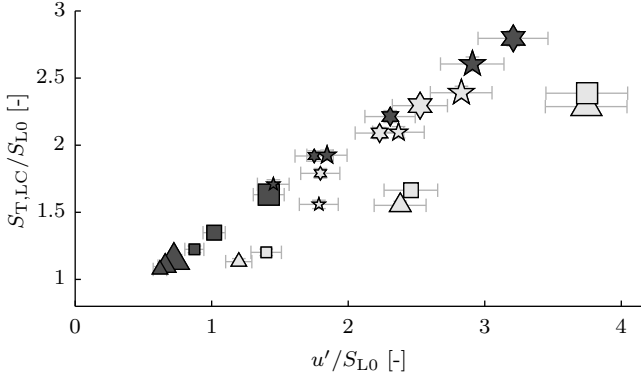


**Figure 3.14:** Normalized turbulent flame speed quantified by the local displacement speed as function of the normalized level of turbulence. All 24 flames are plotted using a unique marker. The light and dark markers correspond to square and cross grids, respectively. The blockage is indicated by the marker size; small -  $\sigma = 0.25$ , medium -  $\sigma = 0.35$  and large -  $\sigma = 0.45$ . The value of  $R_t$  can be read from the marker shape;  $\triangle$  -  $R_t = 1.0$ ,  $\square$  -  $R_t = 0.7$ ,  $\star$  -  $R_t = 0.4$ ,  $\star$  -  $R_t = 0.29$ . The errorbars indicate the uncertainty in both  $S_{T,LD}/S_{L0}$  and  $u'/S_{L0}$ .



**Figure 3.15:** Normalized turbulent flame speed measured by the local displacement speed as function of the normalized level of turbulence. Only grids which are very similar to grids used by others, the result is plotted. This allows for a comparison of the current work (cur.) with the data of Sponfeldner (Sp.) and Soulopoulos (So.) which are also plotted in the Figure.





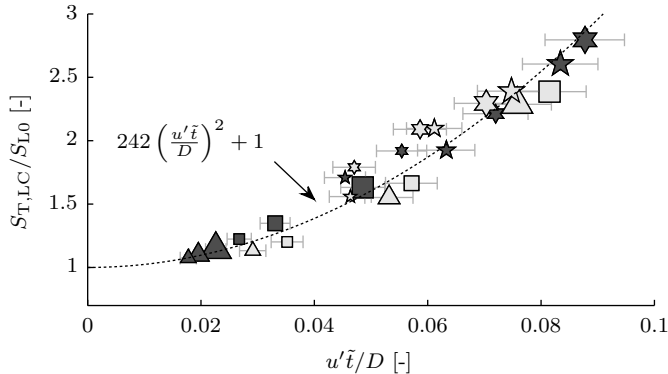
**Figure 3.16:** Normalized turbulent flame speed measured by the local consumption speed as function of the normalized level of turbulence. The light and dark markers correspond to square and cross grids, respectively. The blockage is indicated by the marker size; small -  $\sigma = 0.25$ , medium -  $\sigma = 0.35$  and large -  $\sigma = 0.45$ . The value of  $R_t$  can be read from the marker shape;  $\triangle$  -  $R_t = 1.0$ ,  $\square$  -  $R_t = 0.7$ ,  $\star$  -  $R_t = 0.4$ ,  $\star$  -  $R_t = 0.29$ . The errorbars indicate the uncertainty in both  $S_{T,LC}/S_{L0}$  and  $u'/S_{L0}$

fidence interval gives variation of  $\pm 1\%$ ), the uncertainty in bulk velocity ( $\pm 1.6\%$ ) and the error in  $S_{L0}$  ( $\pm 5\%$ ), due to limited accuracy of determining  $\phi$ . The vertical errorbars are determined by the repeatability of the bulk velocity and the error in  $S_{L0}$  as well, but also by the uncertainty in determining the flames half-angle  $\alpha$  (95% confidence interval gives a variation of  $\leq 1\%$ ). For the vertical errorbars in Figure 3.15 furthermore the possible error due to alignment errors ( $\leq 0.5^\circ$ ) is included. The flow velocity is measured in the non-burning configuration, while in the burning situation the flame will affect the velocity field to some extent. However, this uncertainty is not included here as the focus is on the uncertainty of the repeatability of the measurement values rather than of the definition itself.

### 3.5.2 Flame speed

The local consumption speed is used to compare the different grids as it can be measured more reliably compared to the displacement speed. Figure 3.16 shows these results for the flames of the 24 grids as function of  $u'/S_{L0}$ , where  $u'$  is the averaged value of the turbulent fluctuations along the  $\bar{c} = 0.5$  isocontour. As noted before, the two different definitions of the turbulent flame speed do not necessarily provide the same values as is also the case here;  $S_{T,LC}$  is on average three times larger than  $S_{T,LD}$ . Although this discrepancy may appear large, both measures for the flame speeds are precisely defined without ambiguity, and should not be compared with each other [27]. Similar differences can be found in literature, i.e., Lawn and Schefer [57] report a difference above 1.7 and Shepherd and Cheng [87] even above four. Nevertheless, these measures for the flame speed appear to indicate precise trends of burning rate in response to variations in the fractal grids used to perturb the flow.

The uncertainty for the horizontal errorbar is determined similarly to that for Figure 3.14. The vertical errorbar here is determined by the accuracy of measuring the amount of flame surface, for which the error is estimated to be below 2% accounting for



**Figure 3.17:** Normalized turbulent flame speed measured by the local consumption speed as function of the product of the level of turbulence ( $u'$ ) and the convection time between the stabilization rod and the measurement location ( $\tilde{t}$ ), normalized by the duct-size  $D$ . A fit through the data is shown by the dotted line. The light and dark markers correspond to square and cross grids, respectively. The blockage is indicated by the marker size; small -  $\sigma = 0.25$ , medium -  $\sigma = 0.35$  and large -  $\sigma = 0.45$ . The value of  $R_t$  can be read from the marker shape;  $\triangle$  -  $R_t = 1.0$ ,  $\square$  -  $R_t = 0.7$ ,  $\star$  -  $R_t = 0.4$ ,  $\star$  -  $R_t = 0.29$ .

the statistical convergence ( $<1\%$ ), and errors in the edge-detection process ( $<1.8\%$ ). The uncertainty in  $I_0$  (valued between 0.95 and 1.12 [27], while in this work 1.0 is assumed) and the uncertainty in 2D to 3D conversion of the FSD ( $<10\%$  based on results of [103]) are not included as it is assumed to result in the same offset for all measurements.

The same trend is apparent from Figure 3.16 as from Figure 3.14, i.e., a higher  $u'$  results in a higher turbulent flame speed. However, there is a certain amount of scatter in the figure. Especially, the square grids with  $R_t = 1.0$  or  $0.7$  (light triangle and square markers) tend to have a much lower turbulent flame speed for similar  $u'/S_{L0}$  compared to the other grids. These grids have a rather large  $z^*$  such that the peak in  $I$  at the centerline is located downstream of the stabilization rod. Moreover, the mean flow profile is rather inhomogeneous in these cases. Here, the high flow velocity in the center reduces the time for the turbulence to wrinkle the flame front. This process of time-dependent wrinkling is discussed by Driscoll [27] and explained by Taylor's theory of turbulent diffusion. In this reference it is shown that for different types of flames the flame-brush thickness,  $\delta_T$ , increases with  $u'\tilde{t}$ , which in turn increases the turbulent flame speed. Here  $\tilde{t}$  is a characteristic convection time for the flame concerned. For the V-shaped flame concerned here  $\tilde{t}$  is set to the average time a fluid parcel needs to travel, based on the cold flow measurements, from the position where the combustion is initiated to the point where the wrinkling is assessed. This is in fact the distance between the position of the stabilization rod and the measurement region. The convection time is averaged also along the  $\bar{c} = 0.5$  isocontour similar to  $u'$ . In Figure 3.17 the local displacement speed is plotted against  $u'\tilde{t}$ . By accounting for the convection time a better collapse of the data is obtained. The points fairly well collapse onto a single curve, which can be characterized by a quadratic polynomial as shown by the dotted line. The deviation of the quadratic polynomial fit from the measurement points,  $|S_{T,LC,fit} - S_{T,LC}|/S_{T,LC}$ , is on average 3.9% and 7.4% for

the cross and square grids, respectively. The maximum deviation is 12% and 14%.

The fact that the mean level of turbulence and the mean convection time provide an accurate scaling parameter for predicting the turbulent flame speed is a convenient property for engineering fractal grids for premixed combustion. The curve of Figure 3.17 together with the relation to quantify the turbulence downstream of the grid based on grid parameters can be used to predict the turbulent flame speed based on the design of the grid.

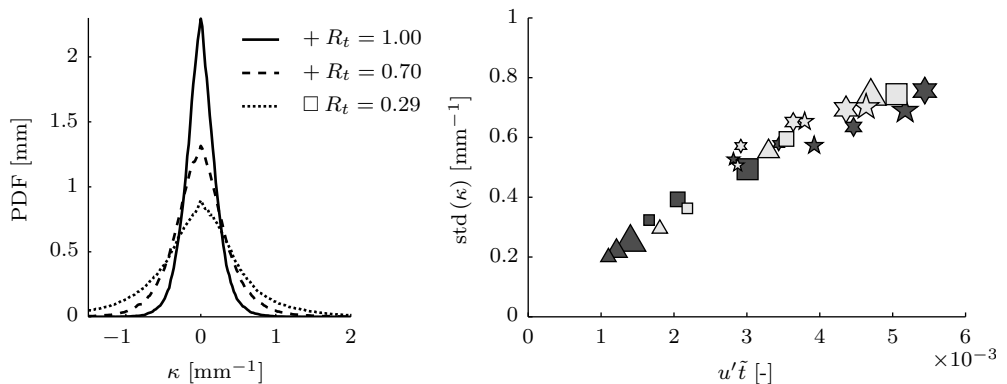
Now that it has become clear what determines the turbulent flame speed in the V-shaped flame for different classical and fractal grids it is interesting to have a look at the observation of Sponfeldner et al. [93] as mentioned in the introduction. According to the measurements of Sponfeldner et al. an increase in  $u'$  due to a decrease of  $R_t$  seems to be more effective than an increase in  $u'$  due to an increase in blockage. According to the curve obtained here,  $u'$  and  $\tilde{t}$  are the parameters determining the increase in  $S_{T,LC}$  (or  $S_{T,LD}$ ). The change in  $R_t$  in [93] from 0.56 to 0.43 provides an increase in  $u'$ , but also a decrease of the inhomogeneity of the mean flow profile and thereby a lower velocity in the center which, in turn, extends the time available for wrinkling the flame. This change in grids increases both  $u'$  and  $\tilde{t}$  and leads to an increased flame speed. Changing the blockage of the grid with  $R_t = 0.43$  now from 0.34 to 0.37 provides a similar increase in  $u'$  but no further increase in  $\tilde{t}$ . Consequently, the resulting increase in flame speed is less compared to the previous change. With the dependence between  $u'$ ,  $\tilde{t}$  and  $S_{T,LC}$  identified here the observation of Sponfeldner et al. are correctly explained.

### 3.5.3 Flame front curvature

As reported by Soulopoulos et al. [92], the flame front curvature distribution for flames in fractal-grid-generated turbulence tends to be only marginally affected compared to the situation using a classical grid. Nonetheless, an enhancement of the turbulent flame speed is reported. For the flames presented here also the flame front curvature distribution is directly determined, for which significant differences between the classical and fractal grid cases are observed, contrasting [92].

The region where the flame front curvature is assessed is reduced compared to previously presented OH-LIF measurements. The region assessed is bounded by  $0.7 \leq x \leq 18$  mm and  $205 \leq z \leq 222$  mm. By using this configuration much smaller curvatures can be measured accurately, i.e., within 10% for curvatures up to  $3.5 \text{ mm}^{-1}$ .

Figure 3.18a shows the probability density function (PDF) of the flame front curvature for several grids with the same blockage. For the classical grid a much more narrow distribution is obtained than for the fractal grids, which is contrary to what was observed by Soulopoulos. For our measurements a clear dependence is apparent for the standard deviation of the curvature distribution on the level of turbulence and the convection time as can be seen in Figure 3.18b. So, the increase in turbulent flame speed appears to be accompanied by finer flame structures, which seems a natural consequence of the increased turbulence and available time for wrinkling of the flame front. Finer wrinkling makes it possible to confine more flame front in the same space, thereby increasing  $\Sigma$ . The enhanced turbulence, however, also contributes to increased large scale corrugation of the flame front which widens the flame-brush and thereby lowering  $\Sigma$ . As demonstrated in [27] the definition of the local displacement speed can be approximated by  $S_{T,LC}/S_{L0} \approx I_0 \Sigma_{\max} \delta_T$ , where  $\Sigma_{\max}$  and  $\delta_T$  are the maximum



**Figure 3.18:** (a) Probability density function of the flame front curvature of the flames for three different grids. The blockage ratio for the three grids is 0.35. (b) Standard deviation of the curvature distribution for all 24 grids plotted as function of  $u'\tilde{t}$  (same as used in Figure 3.17). The light and dark markers correspond to square and cross grids, respectively. The blockage is indicated by the marker size; small -  $\sigma = 0.25$ , medium -  $\sigma = 0.35$  and large -  $\sigma = 0.45$ . The value of  $R_t$  be can read from the marker shape;  $\triangle$ -  $R_t = 1.00$ ,  $\square$  -  $R_t = 0.70$ ,  $\star$  -  $R_t = 0.40$ ,  $\star$  -  $R_t = 0.29$ .

FSD and the flame-brush thickness, respectively according to appropriate curve-fits. The combination of the two effects (change in  $\Sigma_{\max}$  and  $\delta_T$ ) on the turbulent flame speed is clearly positive. The product  $\Sigma_{\max}\delta_T$  increases when supplying enhanced fractal-grid-generated turbulence due to finer wrinkling and to a widened flame-brush.

## 3.6 Conclusions

A parametric study has been performed to identify how fractal-grid-generated turbulence increases the turbulent flame speed for premixed flames. In total 24 different grids were used to generate turbulence upstream of a V-shaped flame. By using two different fractal patterns and variation in blockage ratio,  $\sigma$ , and ratio of bar thicknesses,  $R_t$  clear trends have been observed.

A close approximation of the experimental setup of Soulopoulos and Sponfeldner was realized, thereby providing the basis for a direct comparison with their results. The turbulent flame speed measured by the flame's half-angle agrees with their reported values within the measurement uncertainties, which provides an independent confirmation and hence a high level of confidence that the turbulent flame speed can be significantly enhanced when using fractal grids compared to classical grids with similar blockage ratio.

The flame speed is mainly related to the level of turbulence present at the location of the flame and the time available for the turbulence to wrinkle the flame. Here, the turbulence downstream of the fractal grids is simply more intense. All measurement points, including the three classical grids, follow a consistent trend where variation in local displacement speed is almost exclusively explained by variation in  $u'\tilde{t}$ .

With  $u'$  being key in determining the turbulent flame speed, it is of great value that this quantity can be predicted reliably downstream of different grids. The turbulence

intensity,  $I$ , along the centerline downstream of the square grids is self-similar when scaling the downstream distance with ‘wake-interaction’ length,  $z^* = (L_0 - t_0)^2 / t_0$ . We extended this by showing that the peak value of  $I$  behaves as a linear function of  $\sigma \frac{D}{z^*}$  which also agrees with data of others for much different grid sizes. Also for the cross grids the turbulence intensity along the centerline follows a self-similar dependence when the downstream distance is scaled with the outer grid size. The absolute intensity scales linearly with  $t_0/D$ , which also holds for wind-tunnel data of Hurst and Vassilicos. Using the centerline data is in general representative for the mean turbulence intensity in the off-center region near the flame. However, the inhomogeneity in mean flow for some grids is too severe to use only centerline data. The square grids show a larger inhomogeneity of the mean flow in transverse direction, which also creates more variation in convection time, hindering the a-priori prediction of the turbulent flame speed. In that sense it is more favorable to use cross grids albeit that square grids result in slightly higher turbulence levels.

In order to further fortify the obtained trends it is suggested to extend the current work with measurement at different equivalence ratio and different bulk velocities. However, current results will already be of use in the design process when applying fractal grids in practical burners. For example, it is shown by Verbeek et al. [102] that the combustion rate in low-swirl burners can be significantly enhanced when applying fractal cross grids. The clear view of the level of turbulence and its effect on the turbulent flame speed for a wide range of different fractal grids facilitates the selection procedure for the right grid for a specific burner.

### Acknowledgment

The authors very much appreciated the constructive contact with Thomas Sponfeldner and Frank Beyrau from Imperial College London in order to obtain a V-shaped flame burner similar to their facility.

## Chapter 4

# Fractal grids enhancing low-swirl combustion

### Abstract

The use of fractal grids in a low-swirl burner can significantly increase the turbulent combustion rate, realizing a higher power density in these flames. The standard turbulence generating blocking grid has been replaced by one consisting of a pattern of cruciform structures of different sizes, forming a multi-scale grid derived by truncating an underlying fractal structure. It is shown that the turbulence is intensified when comparing the flow behind the multi-scale grid to the reference situation, where a standard single-scale grid is used. This increase is expressed by more than doubling of the r.m.s. of the velocity fluctuations, while only marginal changes in pressure drop are observed. From the energy spectrum of the velocity it becomes clear that not only the largest scales are more energetic; also smaller scales are introduced as the spectrum is further extended into the high-frequency range. By means of planar OH-LIF the flame geometry was assessed, showing an increase in flame surface density and widening of the flame brush as well as much finer wrinkling of the flame front for the cases involving a multi-scale blocking grid. Here the turbulent flame speed (local consumption speed) is doubled. The grid parameters that were varied are the level of ‘fractality’ and the blockage. For both properties their effect on the flow and combustion are evaluated. The blockage mainly affects the stabilization mechanism, while the level of ‘fractality’ determines the increase in turbulence and combustion rate. Finally, it is shown that the low  $\text{NO}_x$  emission levels that characterize the low-swirl mode of combustion are not affected.

---

This chapter is based on publication:  
Fractal grids enhancing low-swirl combustion, A.A. Verbeek, T.W.F.M. Bouten, G.G.M. Stoffels, B.J. Geurts and T.H. van der Meer (2014), *Combustion and Flame* (in press).

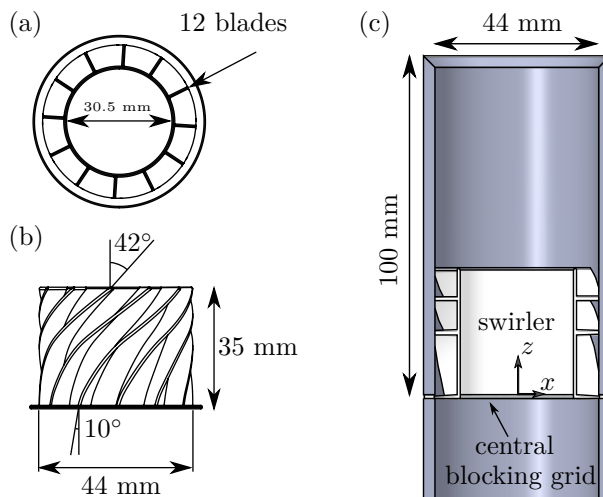
## 4.1 Introduction

It is known that fractal grids can efficiently produce turbulence. The extensive study on fractal-grid-generated turbulence by Hurst and Vassilicos [38] marks the start of intense interest in fractal grids. With a flat partially blocking object placed in a flow that is constructed according to an iterative multi-scale pattern, i.e., a fractal, turbulence can be generated at different scales simultaneously. This leads to an elongated region behind the fractal object where intense turbulence is produced before it decays further downstream. A fractal grid acts as a ‘magnifying lens’ for the non-equilibrium region as stated by Valente and Vassilicos [99]. There is a significant amount of research on the decay of this fractal-grid-generated turbulence [45, 46, 68, 86, 97, 98, 99] which appears to extend classical theory on homogeneous decaying turbulence, in which the dissipation rate,  $\varepsilon \propto u'^3/L$  [82], where  $u'$  and  $L$  denote the r.m.s. of the velocity fluctuations and integral lengthscale, respectively. However, the fact that turbulence is intensified, measured by  $u'$ , starting from several mesh-sizes downstream of the grid is indisputably established.

Many practical applications can benefit from the efficient generation of turbulence. As mixing is enhanced as shown in [53, 95], it can be of use in mixing of product streams in process technology, in premixed combustion [32, 92, 93] or even in environmental fluid mechanics as fractal fences [43]. Fractal grids could also be used as air brakes on planes having in addition considerable noise reduction [54, 74] or in the form of fractal flanges for more efficient flow metering [2, 70, 75, 108] or flow conditioning [67]. An alternative approach to enhance mixing can be found in the effect of time-modulated turbulence [12, 15, 47, 48, 49]. By modulating the rate at which energy is supplied to the flow at a frequency close to the inverse of the large-eddy turn-over time, the turbulence tends to be more receptive to the supplied energy, resulting in a higher turbulent kinetic energy. This effect has been observed in both numerical simulations [47, 48, 49] and experiments [12, 15]. An active grid as used in [15] is quite laborious and typically used in wind tunnels only. A much simpler and more compact active grid is proposed in [101], however the authors did not report a particular frequency of the forcing at which the turbulence response was maximal. In that respect, fractal grids provide a more convenient static agitation to raise the level of turbulence, especially for the incorporation into practical applications.

In this paper it is demonstrated that fractal grids can be used to increase the power density of a practical, industrial low-swirl burner [18]. Up to now only academic flames have been subjected to fractal-grid-generated turbulence. Goh et al. [32] investigated a counter-flow flame and V-flames have been examined by Soulopoulos et al. [92, 93]. The combustion in a low-swirl burner takes place in mid-air and is dominated by a diverging mean flow field generated by a flow consisting of an outer swirling part and a central purely axial part with turbulence generated by a blocking grid (see Figure 4.1). Recent work also shows the importance of the turbulence generated by the shear layer between the two flows [4], especially in view of the stability of these flames. However, in the center region it can be considered as a freely propagating turbulent flame. This makes the low-swirl flame by its very nature ideal to study the effect of the fractal-grid-generated turbulence on the combustion rate of premixed flames.

In the center region of the low-swirl flame there is a relatively low level of turbulence compared to the outer regions where large shear stresses are observed [63].



**Figure 4.1:** (a) Top view of the low-swirl generator. (b) Side view of low-swirl generator. (c) Cross section of complete burner arrangement.

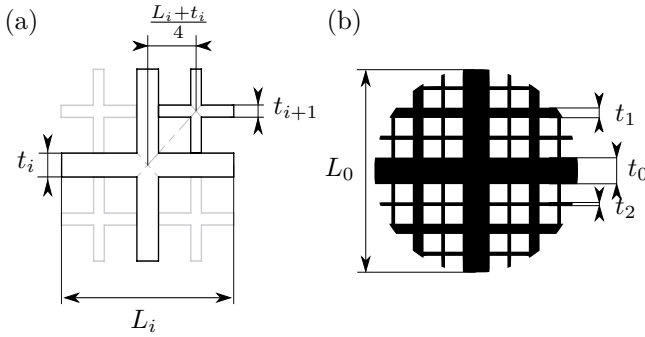
This results in limited wrinkling of the flame [40] and therefore a limited combustion rate. To increase the combustion rate in this central region, the turbulence should be enhanced, since the turbulent flame speed,  $S_T$ , linearly relates to  $u'$  as demonstrated by Cheng et al. [20]. By replacing the central blocking grid (see Figure 4.1) that is balancing the central and swirling flow, while also generating the turbulence, by a fractal grid, we exploit the beneficial properties of fractal-grid-generated turbulence in a practical burner. While the used thermal power of 30 kW on its own cannot be considered as industrial scale, the mean axial velocity, being a more relevant scaling parameter, (here 8.4 m/s) is comparable with those of small industrial burners [18]. Hence, it is expected that the findings presented in this paper are of relevance to industrial applications. Further engineering optimization may be required in actual products - this is beyond the scope of this paper.

The organization of the paper is as follows. In section 4.2 we describe the fractal grids that are investigated as well as the low-swirl burner and the experimental conditions. The properties of the isothermal flow are reported in section 4.3. Here a distinction is made between a fractal grid placed in a pipe flow and a fractal grid placed inside a low-swirl generator. In section 4.4 the burning configuration is analyzed. Concluding remarks are made in section 4.5.

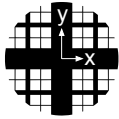

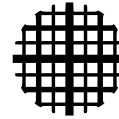
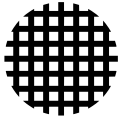
## 4.2 Fractal grid suitable for low-swirl burner

In this section we first discuss the design of the fractal pattern that is used in combination with the low-swirl burner (4.2.1) and proceed with the actual dimensions of the grids (4.2.2). The low-swirl generator itself is described in subsection 4.2.3.



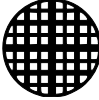
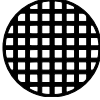
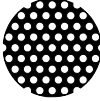




**Figure 4.2:** (a) Definition of the fractal ‘cross’-pattern. (b) Circular cropped fractal grid with three iterations.

Fractal cross			Classical cross
$R_t = 0.23$	$R_t = 0.40$	$R_t = 0.70$	$R_t = 1.00$
			
$t_0 = 8.4$	$t_0 = 5.9$	$t_0 = 3.4$	$t_0 = 2.4$

**Table 4.1:** Grids used in pipe flow with different  $R_t = \frac{t_{i+1}}{t_i}$ . The blockage ratio,  $\sigma$ , is for all these grids 60%, which is typical for blockage disks in low-swirl burners [17].  $L_0 = 44$  mm. The bar thickness of the largest iteration,  $t_0$  is indicated in mm.

	Fractal cross			Clas.	hex.
$R_t \rightarrow$	0.29	0.40	0.70	1.00	-
					
$\sigma \downarrow$	-	3.41	-	1.27	-
.60	4.73	3.80	2.26	1.41	2.53
.65	5.25	4.20	2.52	1.56	2.37

**Table 4.2:** Grids used in combination with low-swirl generator. The grids are created with various blockage ratios ( $\sigma$ ) and different thickness ratios ( $R_t = \frac{t_{i+1}}{t_i}$ ). The thickness of the bar of the first iteration,  $t_0$ , is denoted for each grid in mm. For the hexagonal grids the hole diameter is given. The outer diameter is  $L_0 = 28.5$  mm.

### 4.2.1 Different fractal patterns

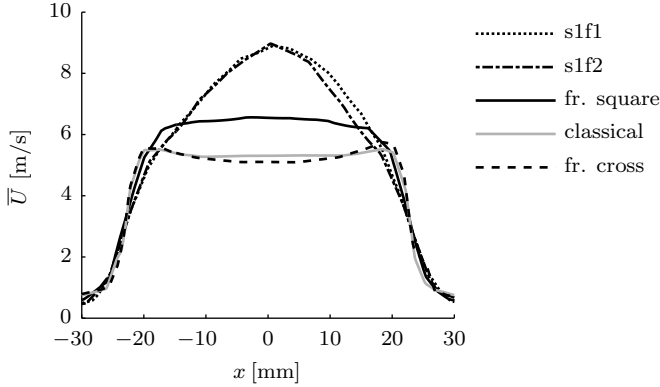
Several families of fractal grids have been studied by Hurst and Vassilicos [38]. Each family of grids studied in [38] is based on a different fractal-generating pattern, being a ‘cross’, an ‘I’ or a ‘square’. Of these families, the ‘square’-family is most extensively studied. Other multi-scale grid patterns are studied by Nicolleau et al. [75], where instead of a flange with a single large opening, a fractal distribution of holes of different sizes is used as well as openings with fractal perimeters. For all these types of grids it is known that the turbulence downstream is enhanced. However, the grid used in combination with the low-swirl burner should yield a flow field that is compatible with the flame stabilization mechanism. This requires a mean axial velocity,  $\bar{U}$ , that remains constant in radial direction or it should be a slightly convex function as function of the radial distance from the centerline [20].

Isothermal RANS simulations were performed to investigate the applicability of the various grids. The flow domain included the low-swirl generator as depicted in Figure 4.1c, as well as 100 mm length of pipe upstream of the grid. Downstream of the burner exit the domain extends 80 mm in radial direction and 100 mm in axial direction. The domain was discretized using 325000 tetrahedral elements with an edge size of approximately 2 mm in the region up to the burner exit. Downstream of the exit the elements are gradually increased to 15 mm. The number of elements was considered sufficient as increasing the number did not change the obtained velocity profiles at the burner exit significantly. The RANS simulations are performed using the commercial software Ansys CFX 14, with the  $k - \varepsilon$  turbulence model applied. The axial velocity is evaluated for the different blockage grids far enough downstream of the low-swirl generator to allow for the development of the flow, but still upstream of the flame. Here, 4 mm downstream of the burner exit is used.

A grid of the fractal ‘square’ and ‘cross’-family and fractal orifices from [75] denoted by ‘s2f1’ and ‘s2f2’ where used, as well as a classical grid. For each of these grids the resulting mean velocity profile is depicted in Figure 4.3. The classical grid yields a constant velocity profile as function of the radial direction and the fractal cross grid results in a slightly convex profile. Both these grids are therefore considered as compatible with the low-swirl burner. The velocity profiles determined for the other grids show a concave profile, which is due to the relatively low blockage in the center of the grid. The high axial velocity in the center results in poor stabilization as observed in preliminary measurements rendering these grids unsuitable for the current combustion applications.

In Figure 4.2a the fractal cross pattern is defined. Three iteration levels are used and the pattern is subsequently cropped circularly to fit inside the pipe or low-swirl generator. Each grid is completely defined by four parameters. These are the length of the largest bar,  $L_0$ , the number of iterations,  $N$ , thicknesses of the largest bar,  $t_0$ , and the ratio of the consecutive bar-thicknesses,  $R_t = \frac{t_{i+1}}{t_i}$ .  $L_0$  is equal to the pipe diameter or the inner diameter of the low-swirl generator. In this study we limit ourselves to  $N = 3$ . Although it is possible to manufacture a grid with four iterations, this limits the range of varying  $R_t$  and  $t_0$ , which are the parameters that are investigated in this work. The blockage ratio,  $\sigma$ , which is often used as a parameter to describe a grid, follows from  $R_t$  and  $t_0$ .

The grids defined according to the ‘cross’-pattern will be referred to as cross grids. The cross grids with  $R_t < 1$  are also denoted as ‘fractal cross’ grids. A cross grid with



**Figure 4.3:** Transverse mean velocity profiles 4 mm downstream of the burner exit for different blocking grids. All grids have a blockage of  $\sigma = 0.6$ . The grids labeled ‘s2f1’ and ‘s2f2’ correspond to the fractal orifices as used in [75].

$R_t = 1$  is referred to as a ‘classical cross’ grid, since it is not multi-scale. In addition a standard low-swirl blocking grid is used. This reference grid contains a hexagonal hole pattern, and is therefore labeled as ‘classical hexagonal’ grid.

### 4.2.2 Two sets of grids

Two sets of grids are examined. The first set of grids is placed inside a pipe flow, without swirl, to investigate solely the effect of the fractal grid on the turbulent flow. In Table 4.1 the four grids for pipe flow are listed. The second set of grids is used in combination with a low-swirl generator. With this set we quantify to what extent the turbulence enhancement due to fractal grids is maintained in the presence of a swirling flow. These grids are listed in Table 4.2.

The minimum value of  $R_t$  arises because of the minimum thickness limit of the laser cutting process, which is 0.4 mm for a metal plate of 1 mm. The tolerances are better than 0.05 mm. Besides the two extreme values of  $R_t$ , two intermediate values for  $R_t$  are selected. The blockage ratios of the grids, which are between 55-65%, are typical for blocking grids in low-swirl burners [17].

### 4.2.3 Low-swirl generator

The low-swirl generator is designed according to the design rules of Cheng and Levinsky [17] and is depicted in Figure 4.1 with all the dimensions that fully define the geometry. The outer diameter is set to 44 mm, which makes the burner appropriate for combustion under atmospheric conditions with a thermal power up to 50 kW. The swirl-number,  $S$ , is approximated to be 0.45 using:

$$S = \frac{2}{3} \tan \alpha \frac{1 - R^3}{1 - R^2 + (m^2 (1/R^2 - 1)^2) R^2}$$

where  $R$  is the ratio between the radius of the central passage and the outer radius,  $\alpha$  is the exit angle and  $m$  is the ratio of the mass flows through the center and

the swirling outer annulus, which is typically 0.8 [17]. According to our tests this low-swirl generator results in a properly stabilized flame when using conventional hexagonal grids with blockage ratios between 0.55 and 0.65.

### 4.3 Turbulent pipe flow with fractal perturbation

In this section first the method for measuring the flow properties is described in subsection 4.3.1. The flow behind the cross grids in a pipe flow is presented in subsection 4.3.2. Subsequently, the flow behind the low-swirl generator with the various blocking grids is presented in subsection 4.3.3.

#### 4.3.1 Measurement method

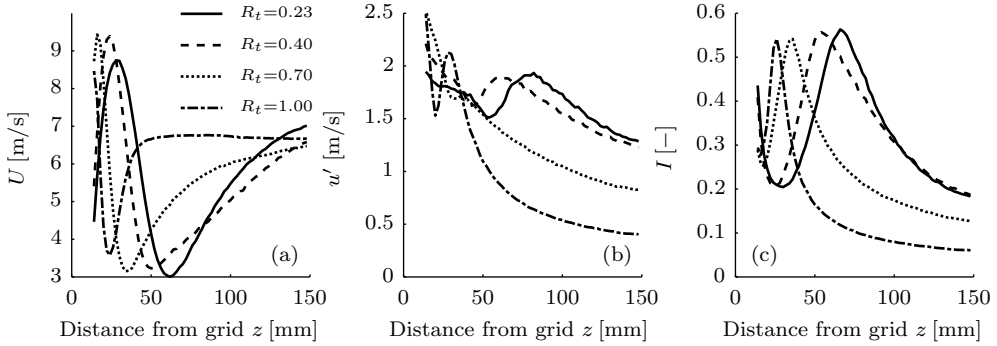
The properties of the turbulent flow are measured by hot-wire anemometry using a locally manufactured single hot-wire probe of 5  $\mu\text{m}$  diameter platinum coated tungsten wire with a length of 0.73 mm. This probe is used in combination with a Dantec 90C10 Constant Temperature Anemometer (CTA) module. More details about the hot-wire setup can be found in [101].

The air is supplied to the grid through a one meter long pipe with a restriction installed upstream which cancels upstream curvature effects. This results in a symmetrical and axial flow profile. The flow rate is controlled by a mass flow controller and set to a bulk velocity of  $U_0 = 7.8$  m/s. The velocity, which is an important scaling parameter for these type of burners [18] is comparable with other experiments [20, 63]. The Reynolds number is  $2.3 \times 10^4$ .

The velocity data is recorded using a NI 9215A BNC with 16 bit resolution. When measuring the mean velocity,  $\bar{U}$ , and the standard deviation of the velocity,  $u'$ , a sample frequency of 1 kHz is used. To obtain converged values of  $\bar{U}$  and  $u'$  data is recorded for 30 s in case of measuring along the centerline. When measuring the velocity at multiple points in a plane, a shorter integration period of 10 s is used. For both cases the value of  $\bar{U}$  does not deviate more than 0.5% from the mean velocity obtained on the basis of a recording of 5 minutes. For  $u'$  the deviation is less than 1%. This indicates that the integration times are long enough to allow a precise comparison of turbulent flow characteristics as function of fractal grid parameters. Alternatively, this can be shown by the fact that the product  $\bar{U}t$  is much larger than the integral lengthscale, which is estimated to be in the order of the burner radius  $r$ , i.e.,  $\bar{U}t/r \geq 3500$ . For measuring energy spectra a higher sampling frequency of 50 kHz is used together with a measuring interval of 5 minutes. These time-traces contain about  $1 \times 10^5$  integral lengthscales, which is sufficient to obtain statistically reliable energy spectra [15, 101]. The 50 kHz sampling frequency is sufficiently to capture the Kolmogorov scales that have a frequency of  $f = \bar{U}/2\pi\eta \leq 12$  kHz, based on the mean velocity on the centerline at the burner exit and Kolmogorov lengthscale,  $\eta$ , determined from the energy spectrum [101].

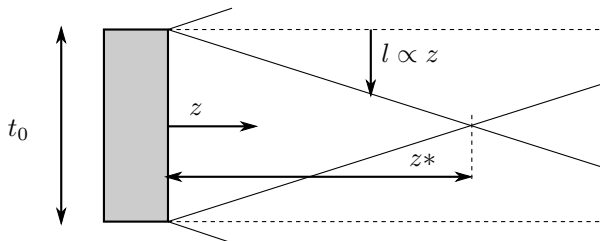
#### 4.3.2 Fractal grid in pipe flow

In Figure 4.4 a-b the variation of  $\bar{U}$  and  $u'$  along the centerline of the tube are plotted. An enhancement of  $u'$  is observed for the fractal grids, compared to the classical grid

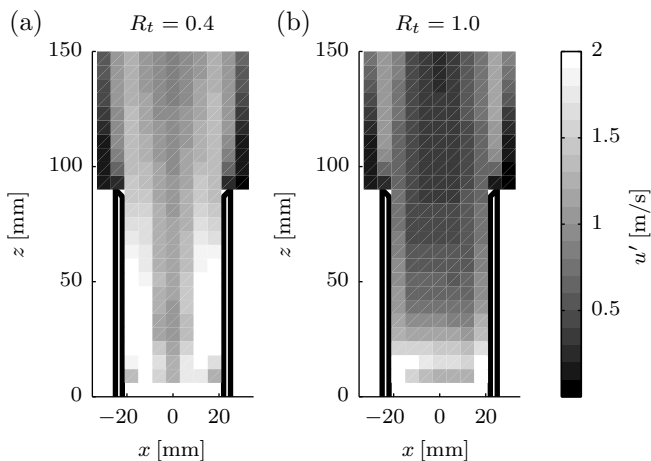


**Figure 4.4:** (a) Mean velocity, (b) r.m.s. of velocity fluctuations and (c) turbulence intensity,  $I = u' / \bar{U}$  as function of the downstream distance measured on the centerline. (No swirl configuration)

with  $R_t = 1.0$  for distance  $\gtrsim 50$  mm. The downstream region ahead of the region in which the monotonic decay of  $u'$  takes place is significantly longer for the fractal cases compared to the classical one. Moreover, the decay rate is observed to be much lower. Already a slight difference in the rearrangement of the square perforations when going from the classical cross grid to the fractal cross grid at  $R_t = 0.7$  induces a much stronger turbulence. By decreasing  $R_t$ ,  $u'$  is further increased. Between the cases at  $R_t = 0.40$  and  $R_t = 0.23$  no significant additional increase is observed. However, the region behind the grid ahead of the far-field monotonic decay region is seen to increase significantly with decreasing  $R_t$ . The turbulence intensity,  $I = u' / \bar{U}$ , which is plotted in Figure 4.4c as function of the downstream distance shows a clear peak at different locations for the various grids. This distance is an increasing function of  $t_0$  which can be reasoned analogously to the ‘wake-interaction’ theory as proposed by Mazellier and Vassilicos [68] for the self-similarity of the turbulence intensity downstream of fractal square grids. It is assumed that the location of the maximum level of turbulence is related to interaction of the wakes downstream of the individual bar-shaped obstructions. The wake downstream of the largest bar of the cross grid develops according to two mixing layers, with  $l \propto z$  [82]. In Figure 4.5 this concept is illustrated. Accordingly, it can be expected that the location where these two mixing layers will ‘meet’ scales as  $z^* \propto t_0$ . The location of the maximum intensity for the four different grids is between  $10t_0$  and  $12t_0$  showing thereby a



**Figure 4.5:** Conceptual wake interaction theory for cross grids by two mixing layers.



**Figure 4.6:** R.m.s of velocity fluctuations as function of axial and radial coordinate for two different cases. (a)  $R_t = 0.4$  and (b)  $R_t = 1.0$ . Each square corresponds to a single measurement point. The black lines indicate pipe geometry. The grid is located at  $z = 0$  mm. (No swirl configuration)

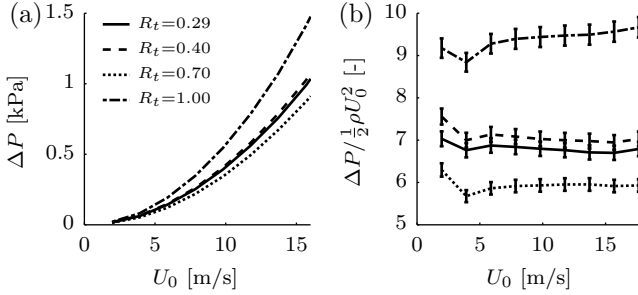
good agreement with this ‘wake-interaction’ theory. However, the self-similarity of the turbulence intensity along the centerline cannot be shown as the investigated range in terms of  $z/t_0$  is rather different for the studied grids. Investigation to whether there is a similar scaling behavior as for square grids is left for further research.

**Off centerline** By traversing the hot-wire in the  $xz$ -plane formed by the radial and axial direction downstream of the grid it is shown that the enhancement of  $u'$  is not exclusively restricted to a narrow region along the axis, but expresses itself throughout the domain. Figure 4.6 compares  $u'$  for the classical grid and the fractal grid with  $R_t = 0.4$ . The relative increase of  $u'$  averaged over a line segment at  $z = 100$  mm and  $|x| < 22$  mm, which is at the exit of the pipe is by a factor of 2.7. This global enhancement of the turbulence intensity behind a fractal grid compared to the classical grid is also observed for the other fractal grids.

**Pressure drop** The pressure drop across the grid,  $\Delta P$ , which is a measure of the energy input required to generate the enhanced turbulence, is measured for the different grids. This is done by a differential pressure meter that measures the static pressure 10 cm upstream of the grids relative to the ambient pressure.

Figure 4.7a shows a typical quadratic behavior of the pressure drop as function of the bulk flow velocity, which is in agreement with experiments performed in a wind tunnel for both classical [44] and fractal grids [38].

The pressure drop can be expressed as a dimensionless pressure drop coefficient or flow resistance,  $\Delta P / \frac{1}{2} \rho U_0^2$ , where  $\rho$  is the density [39]. The pressure drop coefficient is plotted in Figure 4.7b as function of  $U_0$ , where it shows almost horizontal curves for all cases, indicating a constant flow resistance. Furthermore, it clearly visualizes the differences in flow resistance between the different grids. Using a fractal grid results in a 15-35% lower pressure drop compared to the classical cross case at  $R_t = 1.0$ . The



**Figure 4.7:** (a) Pressure drop,  $\Delta P$ , across the grid for several bulk flow velocities,  $U_0$ . (b) Dimensionless pressure drop coefficient,  $\Delta P / \frac{1}{2} \rho U_0^2$ , where  $\rho$  denotes the density. The errorbars represent the variation as observed when repeating the pressure drop measurements several times which yielded the same result within 5%. (No swirl configuration)

largest reduction in  $\Delta P$  is observed for  $R_t = 0.7$ . For  $R_t = 0.23$  and  $R_t = 0.40$  the reduction is a bit less. This suggests that there is an optimum for  $R_t$  where  $\Delta P$  is minimized while maintaining the same flow rate.

The velocity and pressure drop measurements demonstrate clearly that the turbulence downstream of a fractal grid is created much more efficiently, since the turbulent kinetic energy ( $u'^2$ ) increases more than a factor of four as was observed in Figure 4.6, while the energy input decreases.

### 4.3.3 Fractal grid in swirler

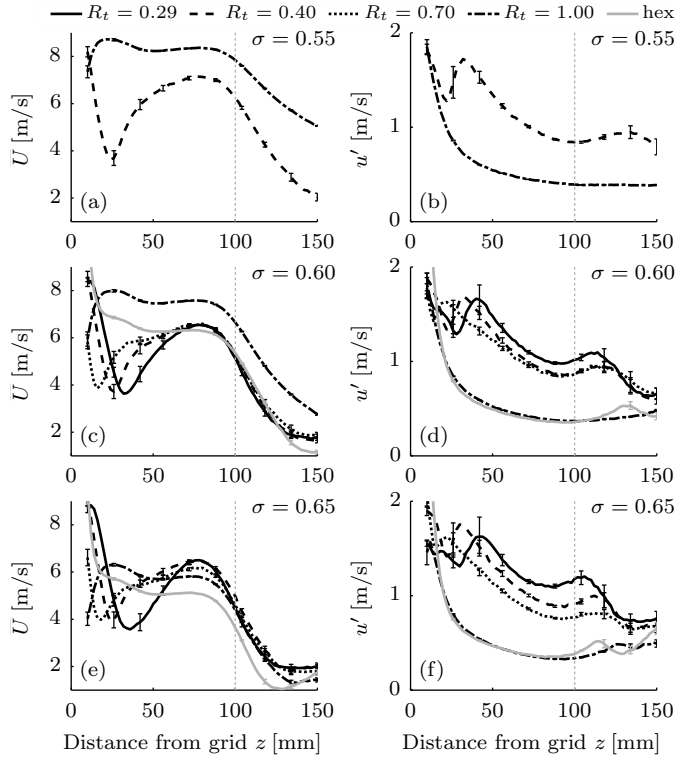
In this subsection the isothermal flow downstream of the swirler in combination with the various grids as listed in Table 4.2 is presented.

#### 4.3.3.1 Measurement along centerline

Figure 4.8 shows an overview of the mean velocity and the r.m.s of the velocity fluctuations along the centerline when the selected fractal grids are used in combination with the low-swirl generator.  $\bar{U}$  experiences a linear decay near the exit of the pipe, which forms the key feature for low-swirl flame stabilization [107]. The strength of this decay is controlled by  $\sigma$ , i.e., an increase in  $\sigma$  also increases the decay rate considerably. Therefore,  $\sigma$  can be used to control the lift-off height of the low-swirl flame.

Apart from the rate of the decay in  $\bar{U}$ , also the value of  $\bar{U}$  is affected by  $\sigma$ . At  $\sigma = 0.55$  a relatively high value of  $\bar{U}$  is measured at the exit of the pipe. For these cases no stable low-swirl flame was obtained. The high velocity resulted in blow-off of the flame. In addition, at  $\sigma = 0.6$  and  $R_t = 1.0$  also a high mean velocity on the centerline develops, implying a poorly stabilized flame.

Close to the grid a local minimum in  $\bar{U}$  is observed for the cases involving a fractal grid, which is directly related to the ‘wake-interaction’ as discussed for pipe flow. Downstream of this largest cross the mean velocity will be lower than the bulk velocity. The downstream distance needed for the flow profile to become homogeneous increases with increasing size of the obstruction. Closer to the grid it is likely that



**Figure 4.8:** Mean velocity (left) and r.m.s of velocity fluctuations (right) along the centerline as function of the downstream distance. Different blockage ratios of the grids are used;  $\sigma = 0.55$  (top),  $\sigma = 0.60$  (middle) and  $\sigma = 0.65$  (top). The vertical errorbars indicate the uncertainty based on the local turbulent intensity according to [96]. The vertical dotted line indicates the pipe exit. (Swirl configuration)

there exist flow recirculations due to the locally high blockage of the largest cross, which cannot be captured accurately using hot-wire anemometry. This explains the high value measured close to the grid downstream of solid material.

It is assumed that the grid is placed far enough upstream of the flame such that there will be enough time for the strong local inhomogeneities present directly downstream of the grid to disappear and that it will not alter the stabilization of the low-swirl flame significantly. This claim is supported by the fact that no large differences in  $\bar{U}$  remain at the location of the exit of the burner for the different grids with the same  $\sigma$ . The remaining inhomogeneity in radial direction caused by the fractal grid are expected not to be larger than what is reported by Hurst and Vassilicos [38]. They observe only a 20% velocity deficit, measured four duct-sizes downstream of the grid. The velocity is a convex function of the span-wise coordinate and all small scale inhomogeneities have disappeared. This also indicated that the grid is placed far enough upstream by using a distance between the grid and the flame of about four grid diameters.

For  $u'$  the same striking difference between fractal and non-fractal grids is observed as in the non-swirling case. An increase of at least a factor of two is measured at the



exit of the pipe for all cases considered with  $R_t < 1$ .

The classical cross and the classical hexagonal cases show a nearly identical development of  $u'$  as function of the downstream distance, while there is a significant difference in the geometry of the grid as shown in Table 4.2. However, a slight alteration in the positioning of the openings of the grid, which exist between the classical cross grid at  $R_t = 1.0$  and the fractal cross grid at  $R_t = 0.7$ , results in a significant difference in  $u'$ . Decreasing  $R_t$  further leads to an additional increase of  $u'$  in the region where  $50 \text{ mm} < z < 120 \text{ mm}$ , albeit less pronounced than the difference between the cases at  $R_t = 1.0$  and  $0.7$ . These results show that the grid parameter  $R_t$  controls the intensification of the turbulence. The relationship between  $R_t$  and the increase in  $u'$  is monotonic over the tested range and  $u'$  appears to be sensitive to changes in  $R_t$  near  $R_t = 1$ . This argues for further investigation of fractal cross grids with  $0.7 < R_t < 1$  to examine the transition in turbulence state between the flows downstream classical and fractal grids.

Using hot-wire anemometry in strong turbulence implies higher uncertainties compared to, e.g., particle image velocimetry or laser doppler velocimetry, due to the inability to measure flow reversals [10]. Especially, downstream of the exit of the pipe, where  $\bar{U}$  decreases, the turbulent intensity,  $u'/\bar{U}$  increases. An estimation of the introduced errors can be made according to [96], who calculated the voltage signal created by a random field up to turbulence intensities of 50%. The error of the measured value  $\bar{U}$  is identified as function of the turbulence intensity. The estimated error is shown in Figure 4.8 by the vertical errorbars. Although there is some uncertainty about the actual value, the claim of approximately doubling  $u'$  can be clearly maintained.

#### 4.3.3.2 2D scan of hex vs fractal

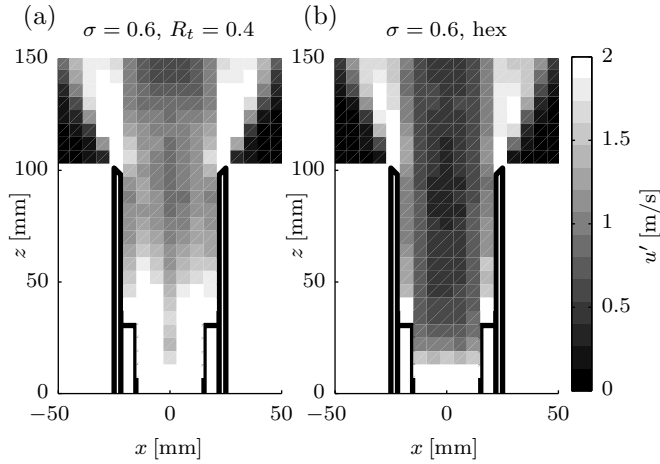
To examine to what extent a fractal grid intensifies the turbulence away from the centerline, hot-wire measurements were performed in the  $xz$ -plane, which is a radial-axial plane. The value of  $u'$  is plotted in Figure 4.9 for a fractal grid with  $R_t = 0.4$  and a classical hexagonal grid, both with  $\sigma = 0.60$ . In the center region, which can be defined as the region behind the grid, i.e.,  $-15 \text{ mm} < x < 15 \text{ mm}$ , and 10 mm downstream of the burner exit, the level of turbulence is doubled as there is an averaged increase in  $u'$  of 103%. This location is most relevant since the flame will stabilize here and most enhancement is desired here.

The fractal grid enhances  $u'$  mainly in the central region. Near the wall inside the tube high values of  $u'$  are observed for both cases, which are caused by the shear near the wall and the shear between the central and swirling flow. Outside the burner for  $|x| > 25 \text{ mm}$  also a high value of  $u'$  is observed, which is due to the turbulence generated by the shear with the stagnant ambient air. The turbulence in both these regions is not affected by the presence of the central blocking grid. Also no enhancement is needed here, since turbulence levels are already high.

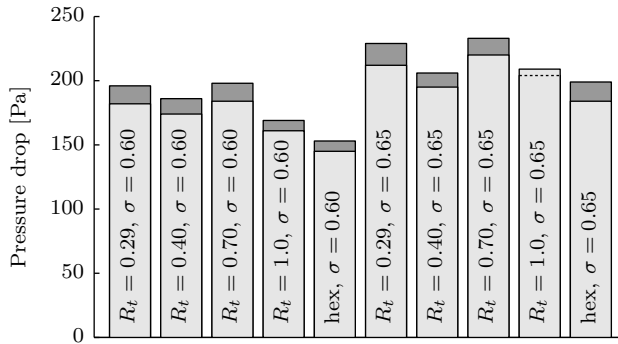
#### 4.3.3.3 Pressure drop

Switching from the standard grid inside the low-swirl generator to a fractal grid affects the pressure drop somewhat. In Figure 4.10 the measured pressure drop over

### 4.3. Turbulent pipe flow with fractal perturbation



**Figure 4.9:** Turbulent velocity as function of axial and radial coordinate for two different cases: (a) a fractal grid with  $R_t = 0.4$  and (b) a hexagonal grid.  $\sigma = 0.6$  for both cases. Each square corresponds with a single measurement point. The black lines indicate the burner geometry. The color-scale is clipped at 1.5 m/s to emphasize the differences in the center region where, in the burning configuration, the flame would stabilize. This is along the centerline and near the pipe exit at  $z = 100$  mm. (Swirl configuration)



**Figure 4.10:** Pressure drop over the complete burner in the non-burning (light bar) and burning (dark bar) situation for different grids. For the classical cross grid with  $\sigma = 0.65$  the pressure drop in the burning situation is lower than for the cold flow. Here the pressure drop for the hot flow is indicated by the dotted line.

the complete burner is shown for the burning and non-burning situations. Replacing the hexagonal grid with a cross grid (fractal or classical) results in a slightly higher pressure drop. The increase is maximally 29% as observed for the case at  $R_t = 0.7$  and  $\sigma = 0.60$ . The pressure drop for fractal cross grids is generally slightly higher than for the classical cross grid, with the exception of  $R_t = 0.4$  and  $\sigma = 0.65$ . This differs somewhat from what was observed for the pipe flow, where consistently a 15-35% lower pressure drop was observed.

The comparison between the pressure drop measured solely over the grids and the pressure drop over the low-swirl generator with blockage grids is somewhat ambiguous as in the latter case not all the flow is forced through the grid. Here, a difference in flow-resistance between grids will alter the balance between the central- and swirling flow. However, this effect is assumed to be small, since  $\bar{U}$  measured along the centerline does not show a strong decrease for grids with higher pressure drop.

The pressure drop in the burning configuration is, with the exception of the case with  $R_t = 1.0$  and  $\sigma = 0.65$ , consistently higher than for the isothermal case. This increase is 6% on average and is caused by the flame itself that creates an ‘obstacle’ for the flow.

To summarize, it can be stated that the pressure drop varies between the various grids. The lower pressure drop for fractal grids as observed with the pipe flow measurements is not maintained in the combination with a low-swirl generator. Almost all cases with fractal grids tend to have a higher pressure drop than the case with the classical cross grid. In all cases the pressure drop is higher than for the classical hexagonal case. However, these differences (up to maximally 29%) can be considered marginally, compared to the increase in turbulent kinetic energy downstream of the fractal grids, which is more than a factor of four. In conclusion it can be stated that the presence of swirl does not cancel the property of efficient turbulence generation by a fractal grid.

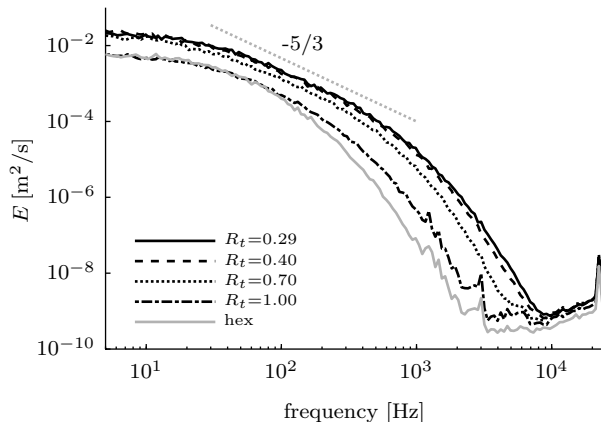
#### 4.3.3.4 Energy spectrum

To display which turbulent scales are enhanced by the use of fractal grids, the energy spectrum of the velocity signal is calculated according to the method introduced by Welch [105] and described in more detail in [101].

Figure 4.11 shows the energy spectrum of the velocity signal recorded at the centerline and 20 mm downstream of the exit of the pipe, which is approximately the location where a flame would stabilize, for a grid with a blockage of 65%. It clearly demonstrates that the turbulence is enhanced over the whole range of scales when using fractal grids. The energy spectra show a small region of about one decade of Kolmogorov power law dependence (slope of  $-5/3$ ) for the cases involving a fractal grid. For the two classical grids no clear power law behavior can be identified.

The classical grids (hex and  $R_t = 1.0$ ) both have a lower level of turbulent kinetic energy (TKE) in the low frequency range compared to the fractal grids. The difference between these two occurs at higher frequency, above approximately 200 Hz. The spectrum for  $R_t = 1.0$  extends further into the high frequency range.

For the fractal grids ( $R_t < 1.0$ ) at low frequency the spectra do overlap, corresponding with the comparable level of TKE observed in Figure 4.8 ( $u'^2$ ). At higher frequency the effect of the ‘fractality’ becomes more clear. Decreasing  $R_t$  from 0.70 to 0.40 extends the spectrum a bit further into the high frequency range. Decreasing



**Figure 4.11:** Energy spectrum at 120 mm downstream of the swirler for the grids with  $\sigma = 0.65$ .

$R_t$  further to 0.29 results in only an additional extension of this range of energetically active scales.

The higher level of turbulence for flows involving fractal grids is accompanied with a wider range of scales contributing to the turbulence.

#### 4.3.3.5 Integral lengthscale

The integral lengthscale,  $L$ , of the turbulence is of importance in premixed combustion. It describes the characteristic lengthscale of the largest eddies [82] and is used as a scaling parameter in the regime diagram for premixed turbulent combustion [79] and in turbulent flame speed correlations [27]. Therefore, it is of interest to see how the use of fractal grids affects  $L$ .

The integral lengthscale is calculated by  $L = \bar{U}T$ , where  $T$  is the integral of the normalized auto-correlation of the fluctuating part of the velocity signal. Instead of integrating up to infinity the auto-correlation is integrated up to the first zero-crossing which is sufficient as demonstrated by [77]. This integration limit is in the order of  $10T$  and is considered adequate [82]. Values do not change significantly ( $< 3.5\%$ ) if the integration limit is doubled.

The values obtained for  $L$  are between 12 and 18 mm. There appears to be no systematic change in  $L$  observed due to the use of particular fractal grids. The range of values of  $L$  is in correspondence with values reported by others [5] for a similar sized burner, adopting a different turbulence generator. It appears that the fractal grids enhance the turbulence level without much changing  $L$ . This is contrary to the observation of Mazellier and Vassilicos [68] where  $L$  was found to increase by more than a factor of two when fractal grids were used. This apparently applies to the use of fractal square grids in a wind-tunnel, while in a low-swirl burner configuration the confined turbulence appears to be characterized by a single well-defined integral lengthscale.

For the evaluation of other turbulent (length)scales that are relevant for combustion, like the dissipation rate and the Kolmogorov scale [79], an estimation of the spatial velocity derivative from the temporal velocity derivative is needed. The often used Taylor frozen turbulence hypothesis is known to be inaccurate at high turbulence intensities (e.g., [24, 65]) as observed in our situation, which is in the order of 20-30% at the exit of the pipe. Therefore, these quantities can not be considered here, but will be investigated using PIV later.

## 4.4 Combustion enhancement due to fractal perturbations

The flames stabilized on the low-swirl burner are assessed by means of OH-LIF. This provides instantaneous 2D cross sections of the turbulent flame front. Statistics of the flame front geometry are obtained from multiple images to describe the flame brush size and turbulent burning rate. Two sets of measurements are presented; one for the full width of the flame and one concentrating on the center region. Global properties as the shape and the stabilization location of the flame follow from full width measurements, while flame front curvature and flame surface density (FSD) are assessed in the center region where the turbulence perturbations arising from the fractal grid are added with significant amplitude.

First a subsection (4.4.1) is devoted to the experimental method and data processing. Subsequently, the shape of the flame (4.4.2), turbulence at the flame brush (4.4.3), turbulent flame speed (4.4.4), and curvature measurements (4.4.5) are presented. Finally, subsection 4.4.6 is dedicated to the emissions.

### 4.4.1 Measuring flame front

In this subsection the method for capturing the flame front geometry by OH-LIF is described. The equipment and operating conditions are discussed, followed by the image-processing procedure and the necessary corrections.

#### 4.4.1.1 Equipment

An excimer pumped dye laser (Lambda Physik LPX 240i in combination with Lambda Physik Scanmate 2, Coumarin-153 dye dissolved in Methanol) is used to generate light with a wavelength near 283 nm. The laser is tuned to the  $Q_1(6)$  line @283.010 nm of the  $A^2\Sigma^+(v' = 1) \leftarrow X^2\Pi(v'' = 0)$  absorption band, as this resulted in the strongest fluorescence signal. The pulse energy is about 0.3 mJ. The laser beam is converted into a planar sheet with a height of approximately 25 mm by using a series of lenses following [100]. We use two lenses to decrease the size of the incoming beam, subsequently two cylindrical lenses to convert the beam into a sheet and a single cylindrical lens to decrease the thickness of the laser sheet which is kept below 150  $\mu\text{m}$ . The OH-LIF signal is captured with an ICCD camera (PI-MAX 3) that has a resolution of  $1024 \times 1024$  px. As objective the Cerco UV lens 45  $f/1.8$  is used. In this configuration the resolution is 12 px/mm. For the measurements where only the center region is examined an additional convex lens ( $f = 100$  mm) is placed in front of the objective to provide for additional magnification, resulting in a resolution of 44 px/mm.

In the burning configuration natural gas is premixed with air in a separate mixing device to ensure complete premixing. The equivalence ratio,  $\phi$ , is set to 0.73, which is typical value for a lean low-swirl flames (e.g., [20]) and far enough from the lean blow-off limit required for stable combustion. The power is set to 33 kW (based on the HHV of Dutch Natural Gas), resulting in a bulk velocity of 8.4 m/s. Although this is slightly higher (7.3%) compared to the isothermal flow, it is expected that the turbulence properties measured in the isothermal case are representative for the combusting situations. In [17] it is shown that the axial velocity measured along the centerline downstream of the low-swirl generator scales very well with the bulk velocity over a wide turn-down ratio of 3.5 for both the combusting and non-combustion situation. Furthermore,  $u'$  along the centerline is not much affected by the presence of the flame [20].

#### 4.4.1.2 Data processing

To extract the flame front geometry from the 2D OH-LIF images a gradient based edge detector is used followed by a spline fitting procedure to obtain a smooth and differentiable representation of the flame front. The full details are described in [100]. Basically, a Laplacian of Gaussian (LoG) edge detector is used to obtain continuous edges. Thresholding is not directly based on the intensity gradient magnitude, but on the overlap of edges with edges detected by the Canny algorithm [13]. This combination is found to perform reliably and allows to detect continuous edges with little erroneous ones included in the results, as well as a priori settings and no need for user input during the detection process.

The procedure requires a single smoothing parameter to be set by the user. This parameter is the standard deviation of the rotationally symmetric Gaussian low-pass filter applied to an image prior to the edge-detection process to reduce noise, which otherwise distorts the detected flame front. The setting of this parameter is a trade-off between the suppression of noise and the ability to measure high curvature values. An estimation of the expected maximum curvature,  $\kappa_{\max}$ , can be made based on the reciprocal value of the laminar flame thickness,  $l_f$ . Based on a laminar flame calculation using Cantera [34] and the GRI-mech 3.0 reaction mechanism [90] for methane combustion  $l_f$  is approximated to be 0.65 mm, resulting in  $\kappa_{\max} = 1.54 \text{ mm}^{-1}$ . This is in correspondence with the maximum flame front curvatures measurements by others. For example, Day et al. [25] show that for a similar low-swirl flame more than 95% of the measured curvatures are smaller than  $1.54 \text{ mm}^{-1}$ . The smoothing parameter is set to 12 px or 0.27 mm of actual length in the zoomed measurement plane. According to [100] this allow for curvatures up to  $1.8 \text{ mm}^{-1}$  to be measured with an error less than 10%. A lower value (6 px) was considered, but this resulted in too much noise and unphysically high curvatures. An error of 10% for the smallest structures and an error lower than 10% for larger structures is found to be adequate to observe changes in the curvature distributions between flames with different turbulent agitation.

#### Corrections

There are inhomogeneities of the OH-LIF intensity across the flame which impede robust edge detection. Two sources for such inhomogeneity can be identified and corrected for. The first one is the inhomogeneity of the laser-sheet, which causes

intensity differences over the height of a frame. To correct for this the recorded OH-LIF signal per frame is divided by the local sheet intensity. The second kind of inhomogeneity occurs in the horizontal direction, since part of the laser energy has been absorbed by the OH radicals along the path of the laser. This inhomogeneity is different for each frame. Values higher than 1.5 times the Otsu threshold [78] of the complete dataset are ‘clipped’ and set to the clipping value. This levels the intensity difference between burned areas upstream and downstream along the laser path. For the zoomed measurements a much smaller area is investigated and much less intensity differences are observed. Nevertheless, the same corrections are applied.

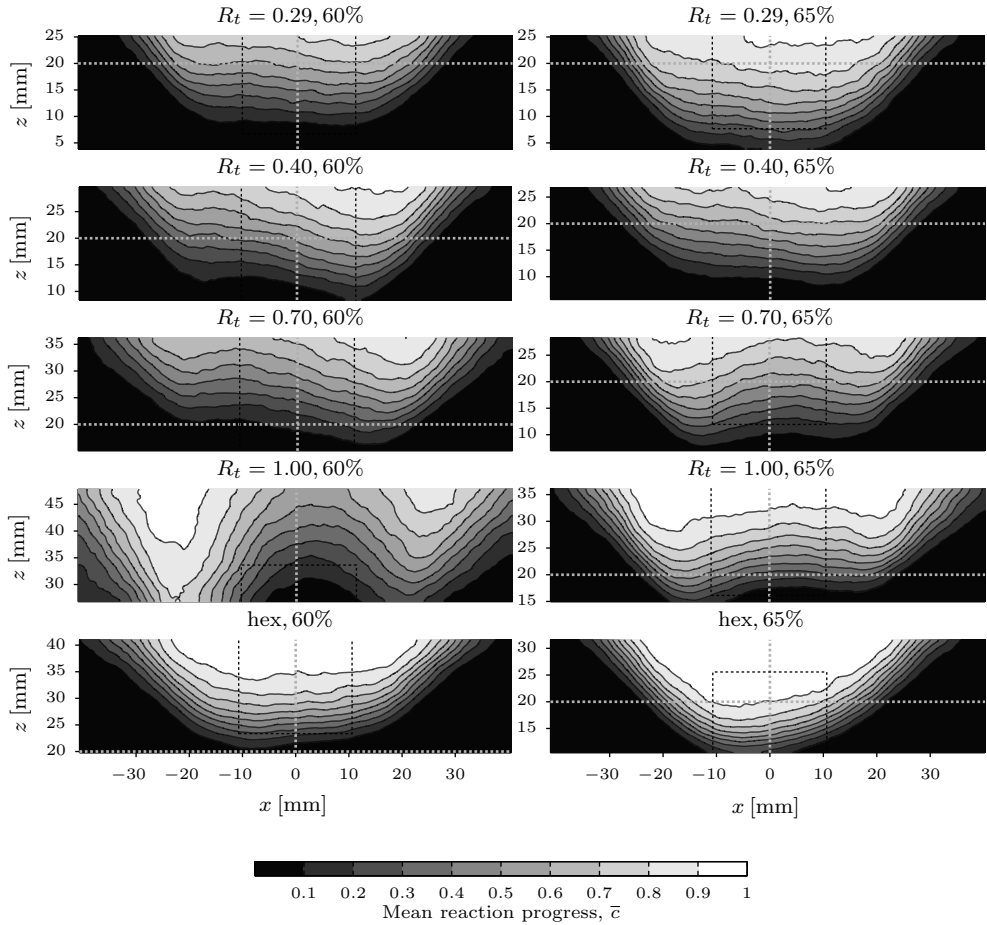
### Post-processing

Some erroneous frames are present in the recordings, which are caused by the nature of the continuous LoG edges. Once the LoG edge overlaps sufficiently with the result of the Canny edge detector a complete edge is included. In regions along a flame front with low gradient in the OH-LIF intensity the LoG-edge detector will find an edge that does not correspond with a flame front, but based on the overlap of the complete LoG-edge with the Canny output it is included in the result. To reduce contamination of the final dataset with these errors an additional post-processing step is used.

First, the value of the LoG of the OH-LIF intensity is measured along an obtained edge. When there is a part along the edge where this LoG signal is low, it indicates that this part of the edge may not be a flame front. Based on two threshold values, i.e., the length of this poor edge region and the value of the LoG, frames are excluded from the dataset. The thresholds are set to an appropriate value by manually investigating a limited number of frames. On average 5.4% of the frames are excluded and this varies between 2.2% and 8.8% for the different measurements. It is assumed that the erroneous frames are mainly caused by frame-by-frame variations in the laser-pulse energy and spatial homogeneity of the laser-sheet and not by a turbulence or combustion related phenomenon that is being disregarded by the filtering operation.

To assure the quality of the final dataset, a sample of 500 frames was taken for both the zoomed and non-zoomed set. From an additional manual inspection we may claim with 95% certainty that the fraction of frames with erroneous edges for the final dataset is below 1.5%. This appears sufficient to measure properties like flame surface density, reaction progress (no more than 1.5% error is made) and also for curvature as shown in [100].

In order to provide insight in the effect of the post-processing on the measured variables, the relative change is determined. The standard deviation of the curvature distribution based on all the detected edges is on average 5.1% higher than for the distribution determined with only the edges in the filtered dataset. This change varies between 3.2% and 7.3% for the different measurements. The difference for the reaction progress (measured between 0 and 1) is in the order of 0.02. For the flame surface density averaged over the flame brush the change is about 2%. In total we conclude that the extraction of flame structures is reliable and a proper basis for further analysis.



**Figure 4.12:** Mean reaction progress,  $\bar{c}$ , for the low-swirl flames with different blockage grids. The vertical and horizontal gray dotted lines denote the centerline and the position 20 mm downstream of the burner exit respectively, to indicate the absolute location of the flame. The total height of the graphs is 22.4 mm. The black dotted lines indicate the region of the zoomed measurements that are performed for a more precise evaluation of the flame front geometry in that region.

#### 4.4.2 Shape of flames

In Figure 4.12 the mean reaction progress,  $\bar{c}$ , obtained from the OH-LIF results is shown. Here,  $\bar{c}$  is the averaged value of the instantaneous reaction progress,  $c$ , which is either zero or unity for unburned and burned regions, respectively. The effect of the different grids on the shape of the flame is two-fold. First, there is a difference in lift-off height. Grids with lower blockage stabilize at a higher position as was expected based on the cold flow measurements. Using fractal grids, and increasing thereby the level of turbulence, results in a lower stabilization position. The second effect concerns the flame brush thickness. The cases involving a fractal grid have



higher turbulence levels and also thicker flame brushes. While the thickness of the total flame brush of the ‘hex’ configuration is only 10 mm, defined as the distance between the  $\bar{c}$  isocontours of 0.1 and 0.9 at the centerline, the flame brush for the  $R_t = 0.29$  case does not even fit within the height of 20 mm.

The global shape of the flame shows for all cases, to a greater or lesser extent, some asymmetry with respect to the centerline. A similar level of asymmetry is also present in low-swirl flames studied by others [16, 5, 18, 20, 25]. In particular, [25] reports similar asymmetric flames for a comparable low-swirl burner, i.e., a diameter of 50 mm. They contribute this to an ‘under-developed’ flow for bulk velocities  $U_0 < 10$  m/s and issues related to misalignment of the vanes with the holes in the perforated plate. This makes the stabilization of the flame prone to azimuthal variation of the flow profile, which are due to the finite number of swirl vanes and the six-fold and four-fold symmetry of the hexagonal grid and cross grid, respectively. However, comparing the effect of the significantly intensified turbulence on combustion properties, like flame surface density, turbulent flame speed and flame front curvature, is not hindered by the slight asymmetry.

An oddity in the set of results is the case of  $R_t = 1.0$  and  $\sigma = 60\%$  which results clearly in a differently stabilized flame. The high axial velocity at the center, as can be seen in Figure 4.8c, creates an extreme ‘W’-shaped flame. Although ‘W’-shaped flames are also reported by others, e.g, [4, 76, 107] and can be identified to some extent in the shapes of the other flames presented here, the severity of the W-shape for this particular flame impedes a proper comparison. The stabilization mechanism of this flame tends to be much more dominated by the inner shear layer (ISL) between the inner core flow and outer annular flow, rather than the flow divergence. A detailed discussion on this ‘shear layer stabilized’ or ‘W-type’ flames can be found in [4]. As the focus of this work is on the effect of fractal-grid-generated turbulence on the combustion rate, this particular flame is disregarded as it is more dominated by the stronger ISL than the turbulence generated by the grids.

### 4.4.3 Turbulence upstream of the flame

It is shown that flames involving a fractal grid are being stabilized at a location closer to the outflow, compared to the case with a classical grid. This implies a higher mean upstream velocity, which suggests an increased burning rate. Furthermore, the increased brush thickness also indicates a higher burning velocity. To investigate quantitatively how the burning rate increased under the effect of fractal-grid generated turbulence, the turbulent flame speed is evaluated as function of the level of turbulence ( $u'$ ). In this way it is verified if the, for low-swirl flames, typical linear dependence between these quantities is maintained [17]. First, in this subsection the level of turbulence at the leading edge of the flame brush is determined, while in section 4.4.4 the turbulent flame speed is evaluated.

In order to have a single measure for the level of turbulence encountered by the low-swirl flame, the centerline value of  $u'$  is used at the location of the leading edge of the flame brush. Here, the leading edge is defined where  $\bar{c} = 0.15$ , as this point is available for all measurements. However, choosing a different value of  $\bar{c}$  does not change the obtained level of turbulence significantly and does not change the conclusions at all.

	$\bar{U}$	$u'_c$	$u'_h$
$R_t = 0.29, \sigma = 0.60$	3.7	1.1	1.36 ( $\pm 0.15$ )
$R_t = 0.40, \sigma = 0.60$	3.7	0.94	1.17 ( $\pm 0.13$ )
$R_t = 0.70, \sigma = 0.60$	3.0	0.92	1.15 ( $\pm 0.13$ )
Hex, $\sigma = 0.60$	2.7	0.46	0.57 ( $\pm 0.06$ )
$R_t = 0.29, \sigma = 0.65$	3.7	1.2	1.49 ( $\pm 0.16$ )
$R_t = 0.40, \sigma = 0.65$	3.5	0.99	1.24 ( $\pm 0.14$ )
$R_t = 0.70, \sigma = 0.65$	3.2	0.81	1.01 ( $\pm 0.11$ )
$R_t = 1.00, \sigma = 0.65$	2.3	0.41	0.52 ( $\pm 0.06$ )
Hex, $\sigma = 0.65$	2.2	0.49	0.60 ( $\pm 0.07$ )

**Table 4.3:** Velocity data in m/s at the centerline and at the downstream position corresponding with the leading edge of the flame ( $\bar{c} = 0.15$ ). Here,  $\bar{U}$  and  $u'_c$  are obtained from the hot-wire measurements in the isothermal flow and  $u'_h$  is the estimated value for  $u'$  at the location of the leading edge of the flame in the burning situation. The estimate is determined from  $u'_c$  increasing it with 7.3% due to the higher bulk velocity and subsequently by 16% due to the higher  $u'$  upstream of the flame for the burning configuration compared to the isothermal flow as is determined from measurements of [20]. The uncertainty of  $u'_h$  is also determined from the data of [20]. Estimating  $u'$  from the isothermal flow data by an increase of 16%, results in no more than 11% deviation from their hot flow data in the region up to the flame ( $8 \text{ mm} < x < 20 \text{ mm}$ ).

Table 4.3 lists both  $\bar{U}$  and  $u'_c$  retrieved from the cold flow data where  $\bar{c} = 0.15$ . Based on the measurement of [20] in flows of low-swirl burners in both burning and isothermal flow one can expect the value of  $u'_c$  of the isothermal flow to be representative for the r.m.s. of the velocity fluctuations of the combusting flow,  $u'_h$ , as well. The level of  $u'$  remains relative unaffected by the flame, which is convenient when only isothermal data is available. In Table 4.3 the estimate of  $u'_h$  is listed together with the uncertainty associated with the used method.

Flames involving a fractal grid encounter a flow with a higher level of turbulence. On average  $u'_h$  is two times higher for the fractal cases. This applies for both blockages. Now a systematic trend becomes clear for  $R_t$ . Decreasing  $R_t$  results in a higher value of  $u'_h$ .

The mean velocity is much more affected by the presence of the flame than  $u'$ . As the flame creates an ‘obstacle’ for the flow, the linear decrease of  $\bar{U}$  along the centerline becomes more steep [20]. Under the assumption that this effect is also encountered for all cases considered here, at least a qualitative trend for the turbulent flame speed measured as the flame’s displacement speed,  $S_{T,LD}$ , can be made. This displacement speed is defined as the local speed at which the leading edge of the flame brush is propagating and it is an often used definition for turbulent flame speed of low-swirl flames [27]. By approximating  $S_{T,LD} \approx \bar{U}$  at the location of the leading edge from the isothermal data, a 40% increase for  $\sigma = 0.60$  and an 80% increase for  $\sigma = 0.65$  in  $S_{T,LD}$  is observed when switching to fractal grids. This suggests that a significant increase in the turbulent flame speed can be realized by applying fractal grids in a low-swirl burner. For a more quantitative determination of  $S_{T,LD}$  LDA or PIV measurements should be performed in the hot-flow [87, 20, 25, 80].

## 4.4.4 Turbulent Flame Speed

### 4.4.4.1 Definition

Instead of using the uncertain, upstream mean velocity to define the turbulent flame speed the more reliable measured amount of flame surface (within 5%) is used here. Under the assumption that the flame front locally propagates with the laminar flame speed,  $S_L$ , the amount of flame surface determines the consumption speed. According to the regime diagram of Peters [79] flames are expected in the ‘corrugated flamelets’ and ‘thin reaction zones’ regimes which is consistent with the local laminar flamelet assumption. The effect of stretch and curvature of the flame front on average on  $S_L$  is assumed to be minimal for unity Lewis number, methane flames [27, 56]. Therefore,  $S_L$  is equal to the unstretched laminar flame speed,  $S_{L0}$  and is evaluated at 0.20 m/s based on the laminar flame simulation using Cantera [34] and the GRI-mech 3.0 reaction mechanism [90]. The turbulent flame speed can be obtained using the local consumption speed,  $S_{T,LC}$ , which is determined from the FSD according to:

$$\frac{S_{T,LC}}{S_{L0}} = I_0 \int_{-\infty}^{\infty} \Sigma d\eta \quad (4.1)$$

where  $\eta$  is the coordinate perpendicular to the flame brush and  $I_0$  the stretch factor accounting for the effect of stretch on the laminar flame speed [27].  $I_0$  is assumed to be 1 for all flames considered here based on [27] who analyzed the DNS of [36] using air methane with  $\phi = 0.52$  and of [6] using  $\phi = 0.8$  reporting values of  $I_0$  between 0.95 and 1.12.  $I_0 = 1$  implies in fact  $S_L = S_{L0}$ .

In reference [27] it is pointed out that expression 4.1 can be rewritten as:

$$\frac{S_{T,LC}}{S_{L0}} = I_0 \Sigma_{\max} \delta_T \quad (4.2)$$

Here,  $\Sigma_{\max}$  is the maximum flame surface density according to the quadratic fit for the flame surface density,  $\Sigma$ , as function of the progress variable:  $\Sigma = 4\Sigma_{\max}\bar{c}(1 - \bar{c})$  and  $\delta_T$  is the flame brush thickness that follows from parameterizing the mean reaction progress as  $\bar{c} = \left[1 + \exp\left(\frac{-4(\eta - \eta_m)}{\delta_T}\right)\right]$ , where  $\eta_m$  is the value of  $\eta$  at which  $\bar{c} = 0.5$ . Both these fits are appropriate for flat flames [57, 87] as well as other premixed flames [27].

The use of the fitted variables,  $\Sigma_{\max}$  and  $\delta_T$ , provides a method to obtain a consumption speed that applies to the complete flame brush (i.e.,  $0 < \bar{c} < 1$ ), while the flame brush is not completely captured for all zoomed measurements. The overlapping range in  $\bar{c}$  for all flames is limited to  $0.22 < \bar{c} < 0.85$ . Although this contains the majority of the flame surface (82% according to the quadratic fit in  $\Sigma$ ) and the integration according to expression 4.1 could be used to capture the trends of  $S_{T,LC}$ , the generality of the value of  $S_{T,LC}$  according to expression 4.2 it preferred.

### 4.4.4.2 Calculation of flame surface density

For an accurate quantification of the FSD and the flame wrinkling, zoomed results from the center region are obtained. The region that is examined for each flame is centered around the centerline and the position where  $\bar{c} = 0.5$ . This region is indicated in Figure 4.12 by the black dotted lines. For each flame 1000 frames are analyzed.

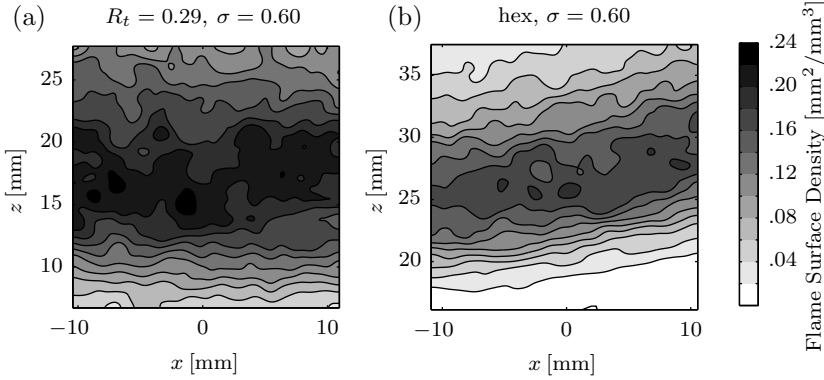
A continuous and smooth spline representing the flame front is obtained during the edge detection process. The FSD is determined by calculating the spline length in every pixel, similar to Shy et al. [89]. This is subsequently averaged over all frames. Note that the obtained FSD is the 2D flame surface density,  $\Sigma_{2D}$ , which is the flame length per area. The method of Shy et al. accounts for the orientation of the flame front within a pixel, yielding a higher accuracy. A comparison with straight-forward edge-pixel counting shows a difference of 9%.

In order to estimation the 3D FSD from the 2D measured equivalent we employed the method described by Veynante et al. [103] and Halter et al. [35]. The conversion factor is defined as  $\Sigma_{2D} = \langle \cos \phi \rangle \Sigma$ , where  $\phi$  the angle between the unit vector normal to the instantaneous three-dimensional flame surface and the measurement plane.  $\langle \dots \rangle$  denotes the ensemble average. Veynante et al. show that  $\langle \cos \phi \rangle^2 + \langle m_y m_y \rangle = 1$ , with  $m_y$  being the fluctuating part of the  $y$ -component (out of the measurement plane) of the unit vector normal to the instantaneous three-dimensional flame surface. However, as this fluctuation is not accessible by the planar OH-LIF measurements  $\langle m_y m_y \rangle$  should be modeled by the measured in-plane components. As we are using a different flame than both Halter et al. and Veynante et al. the question rises which component of the unit vector normal to the measured flame front should be used to model  $\langle m_y m_y \rangle$ . The low-swirl flame can be considered as a flat flame in the center region, where on average the unit vector normal to the flame surface points in the negative  $z$ -direction (in the direction of the unburned mixture). Fluctuations of the normal vector in the  $y$ -direction (out-of-plane) should therefore be represented by the fluctuations in  $x$ -direction as the flame is axi-symmetric with the  $z$ -axis as the axis of symmetry. By stating that  $\langle m_y m_y \rangle \approx \langle m_x m_x \rangle$  the conversion factor becomes  $\langle \cos \phi \rangle = (1 + \langle m_{x,2D} m_{x,2D} \rangle)^{-1/2}$ . Here,  $m_{x,2D}$  is the fluctuating part of the  $x$ -component of the unit vector normal to the measured flame front. (This uses the approximation of  $m_x \approx \langle \cos \phi \rangle m_{x,2D}$ , which is valid if the orientation of the measured flame front inside the measurement plane and the angle  $\phi$  are statistically independent. According to the data of Veynante et al. this is an appropriate assumption.) The conversion factor varies somewhat between the different measurements; on average  $\langle \cos \phi \rangle = 0.83$  and it ranges from 0.82 to 0.86. The values closer to unity correspond to the classical grids, whereas the more intense turbulence associated with the fractal grids results in somewhat lower values of  $\langle \cos \phi \rangle$ .

Figure 4.13 shows the FSD for two cases; fractal cross  $R_t = 0.29$  and hex both with  $\sigma = 0.6$ . Here it can be seen that the maximum FSD is higher for the fractal case: an increase of approximately 20%. Also from this figure it is clear that a larger flame brush is established in the fractal case. In the next section the FSD and the brush size are addressed more quantitatively.

#### 4.4.4.3 Effect on FSD and brush thickness

The control volume that is used to study the flame properties is bounded by a cylinder with a radius of 5 mm. The limited range in radial direction is used to study only a part of the flame that is exclusively affected by the grid turbulence. Table 4.4 lists the values of the maximum FSD,  $\Sigma_{\max}$ , and the flame brush thickness,  $\delta_T$ , obtained from this region. It is interesting to investigate which quantity is most affected by the fractal-grid-generated turbulence as they both contribute to the local consumption speed, which is also displayed in the same table. For the grids at  $\sigma = 0.6$ ,  $\Sigma_{\max}$



**Figure 4.13:** 3D Flame surface density,  $\Sigma$ , for low-swirl flame with (a) fractal cross grid at  $R_t = 0.29$  and  $\sigma = 0.60$ , (b) classical hexagonal grid at  $\sigma = 0.60$ . The FSD is filtered with a Gaussian filter with a standard deviation of 1 mm. This is done to remove the pixel variation in FSD as the value for each pixel is not statistically converged based on 1000 frames. By applying the filter operation a smoother field (better statistical convergence for each filtered point) is obtained while sufficient resolution is maintained.

increases up to 21%, relative to the classical hex case for  $R_t = 0.29$ , but for the case at  $R_t = 0.7$  a small decrease is observed (-2%). All grids at  $\sigma = 0.65$  except the one at  $R_t = 0.29$ , show a decrease with respect to the classical hex case. This means that there is no enhancement of the FSD in general when exchanging the classical hex grids with fractal grids. Among the cross grid alone there is a consistent trend, i.e., decreasing  $R_t$  results in a higher  $\Sigma_{\max}$ . The effect on  $\delta_T$  is more pronounced as using a fractal grid results in a significant increase of  $\delta_T$ , compared to the reference case with a classical hex grid. At  $\sigma = 0.6$ ,  $\delta_T$  changes from 11 mm to 23 mm (for  $R_t = 0.7$ ) and at  $\sigma = 0.65$   $\delta_T$  increases from 8 mm to 20 mm (for  $R_t = 0.29$ ). However, no consistent trend for  $\delta_T$  with respect to  $R_t$  can be identified among the cross grids. For  $\sigma = 0.6$   $\delta_T$  decreases with decreasing  $R_t$ , while for  $\sigma = 0.65$  the opposite trend is observed. This differing observation might be due to the limited number of experiments. It is therefore suggested to perform additional measurements to test whether increasing  $R_t$  mainly affects the large-scale wrinkling, measured in terms of  $\delta_T$ , or the fine-scale wrinkling expressed by  $\Sigma_{\max}$ .

In conclusion, the FSD is dependent on  $R_t$ . A decreasing  $R_t$  results in a higher FSD, but it is not necessarily higher than the FSD for the classical hexagonal case. Furthermore,  $\delta_T$  is clearly increased when using (fractal) cross grids. By intensifying the turbulence using fractal grids, one can clearly obtain an increased consumption speed, which is largely caused by broadening of the flame brush.

#### 4.4.4.4 Local Consumption Speed

In Figure 4.14 the values of  $\frac{S_{T,LC}}{S_{L0}}$  are plotted as function of  $\frac{u'_h}{S_{L0}}$ . Here, it can be seen that the flames involving fractal grids have a significantly higher local consumption speed, i.e., a factor of about two increase compared to the hex and the classical grid cases is measured. When incorporating all measured points a linear trend can be observed that is indicated in Figure 4.14 as well. Such linear trend is also observed

#### 4.4. Combustion enhancement due to fractal perturbations

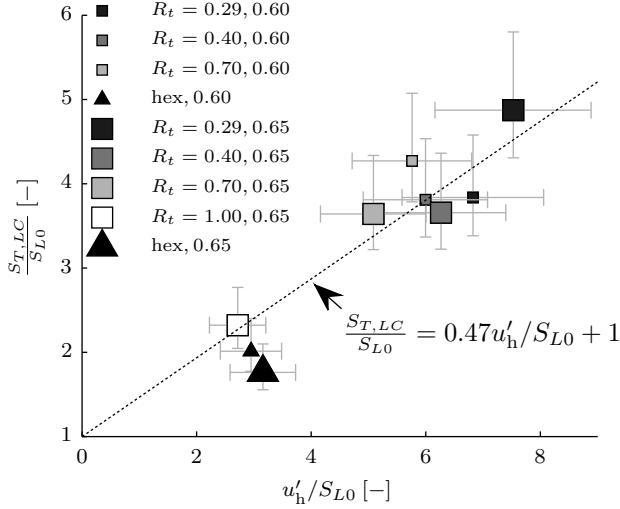
	$\frac{u'_h}{S_{L0}}$ [-]	$\Sigma_{\max}$ [mm <sup>2</sup> /mm <sup>3</sup> ]	$\delta_T$ [mm]	$\frac{S_{T,LC}}{S_{L0}}$ [-]
$R_t = 0.29, \sigma = 0.60$	6.6	0.226	17	3.8
$R_t = 0.40, \sigma = 0.60$	5.8	0.216	18	3.8
$R_t = 0.70, \sigma = 0.60$	5.6	0.183	23	4.3
Hex, $\sigma = 0.60$	2.8	0.187	11	2.0
$R_t = 0.29, \sigma = 0.65$	7.2	0.249	20	4.9
$R_t = 0.40, \sigma = 0.65$	6.0	0.212	17	3.7
$R_t = 0.70, \sigma = 0.65$	4.9	0.193	19	3.6
$R_t = 1.00, \sigma = 0.65$	2.6	0.179	13	2.3
Hex, $\sigma = 0.65$	3.0	0.218	8	1.8

**Table 4.4:** Maximum flame surface density, flame brush thickness and the normalized turbulent flame speed, determined from the center region,  $-5 \text{ mm} < x < 5 \text{ mm}$ .  $\Sigma_{\max}$  is the maximal flame surface density according to the fit for  $\Sigma = 4\Sigma_{\max}\bar{c}(1-\bar{c})$ .  $\delta_T$  is the flame brush thickness according to the fit  $\bar{c} = [1 + \exp(\frac{-4(\eta-\eta_m)}{\delta_T})]$ . Here,  $\eta$  is the coordinate perpendicular to the flame brush and  $\eta_m$  is the value of  $\eta$  at which  $\bar{c} = 0.5$ . The normalized turbulent flame speed,  $\frac{S_{T,LC}}{S_{L0}}$ , is the product of  $\Sigma_{\max}$  and  $\delta_T$ .  $S_{L0}$  is the laminar flame speed, evaluated at 0.20 m/s. From completeness, the level of turbulence upstream of the flame brush,  $\frac{u'_h}{S_{L0}}$  is shown as well.

by others and is characteristic for LSB [17, 20, 87]. This linear trend is persistent for values up to  $u'_h/S_{L0}$  as high as 30 as reported by [20]. Intensifying the turbulence by using fractal grids efficiently enhances the local combustion rate due to the linear response in  $u'$ . The actual slope of the linear dependence varies for different definitions of the turbulent flame speed. The local displacement speed,  $S_{T,LD}$ , is known to increase more rapidly than the local consumption speed,  $S_{T,LC}$ , as shown by Shepherd and Cheng [87] and discussed in more detail in [27]. For the evaluation of  $S_{T,LC}$  Shepherd and Cheng did not use a correction factor to convert  $\Sigma_{2D}$  into the 3D  $\Sigma$ . The slope of their fit is 0.438. This value corresponds reasonably well with the value of 0.37 as observed here when omitting the 2D to 3D correction.

The uncertainty for  $\frac{S_{T,LC}}{S_{L0}}$ , as well as,  $\frac{u'_h}{S_{L0}}$  is also indicated in 4.14. The uncertainty in  $\frac{u'_h}{S_{L0}}$  stems mainly from evaluating  $u'_h$  from  $u'_c$  ( $\pm 11\%$ ) and the variation in  $S_{L0}$  ( $\pm 5.4\%$ ), due the limited repeatability of the equivalence ratio between consecutive measurements ( $\pm 2\%$ ). The errorbar for  $\frac{S_{T,LC}}{S_{L0}}$  is composed of the uncertainty in  $I_0$  (between  $-8\%$  and  $+12\%$ ), the 95% confidence interval for the averaged flame surface density using 1000 frame ( $\pm 3.3\%$ ), the 95% confidence intervals of both  $\Sigma_{\max}$  and  $\delta_T$  ( $< 1\%$ ) and the possible error due to the inclusion of erroneous frames ( $\pm 1.5\%$ ). Although the identified errors result in significant errorbars, the data of Figure 4.14 remains clustered in two separate regions, i.e., one with the classical grids with a low level of turbulence and a low turbulent flame speed and one region with fractal grids associated with much stronger turbulence and a higher burning rate. This demonstrates that fractal grids can be used in actual industrial burners to significantly increase the turbulent flame speed.

The effect of  $R_t$  for the different fractal grids tends to be overshadowed by the uncertainty when considering  $S_{T,LC}$ . A decrease in  $R_t$  results consistently in an

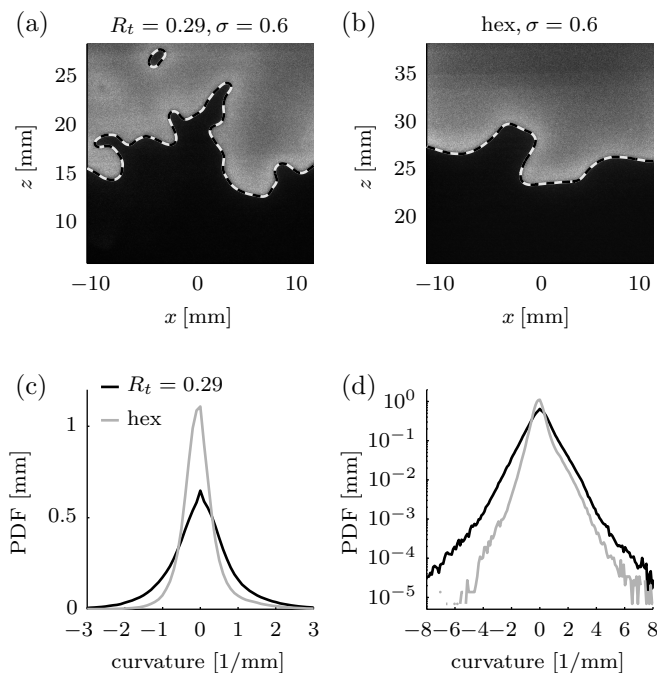


**Figure 4.14:** Normalized local consumption speed as function of the normalized turbulent velocity for the different flames. The errorbars indicate the estimated uncertainties in both  $\frac{S_{T,LC}}{S_{L0}}$  and  $\frac{u'_h}{S_{L0}}$ .

increase in  $u'$ , but not in an increase in  $S_{T,LC}$ . However, all measurement points correspond, within their uncertainty, with the linear trend for the increase in  $\frac{S_{T,LC}}{S_{L0}}$  as function of  $\frac{u'_h}{S_{L0}}$ . This indicates that the nature of low-swirl combustion is not altered by employing fractal grid. Only the level of turbulence is enhanced efficiently.

#### 4.4.5 Flame front curvature

The wrinkling of the flame front can be expressed by its curvature distribution. The flame front curvature,  $\kappa$ , is calculated according to  $\kappa = \frac{x'z'' - z'x''}{(x'^2 + z'^2)^{3/2}}$ , where  $[\dots]'$  represent the directional derivative of  $[\dots]$  along the smooth spline representing the flame front as obtained in the edge-detection process. The curvature is defined positive when the center-of-curvature is located in the unburned mixture. Two instantaneous OH-LIF images, showing a clear difference in flame front curvature between a flame using a fractal grid and a hexagonal grid, are depicted in Figure 4.15a-b. The PDF's of the curvature show much finer wrinkling for the flame with the fractal grid at  $R_t = 0.29$ , compared to the hexagonal grid, as can be seen in 4.15c-d. Only two cases are plotted since the curvature distribution is similarly 'bell'-shaped for all measurements. To compare the different cases the standard deviation of the PDF,  $\sigma_\kappa$ , is plotted in Figure 4.16 for all measurements as function of  $u'_h$ . Here, it can be seen that  $\sigma_\kappa$  is considerably higher for the fractal cases compared to the non-fractal cases. Similar to Figure 4.14 also here two clusters are observed. Such finer wrinkling was not reported by Soulopoulos et al. [92] when switching from a classical grid to a fractal grid in their V-flame configuration. Only a marginal difference in the tail of the PDF was reported, while there was a significant difference in turbulence level between the



**Figure 4.15:** (a,b) Example of an OH-LIF data frame, showing the clear difference in flame front curvature between fractal and non-fractal case. (c) PDF of flame front curvature on linear scale. (d). Same as c, but on logarithmic scale.

flow behind the fractal and classical grid.

There is a clear relation between the standard deviation of the PDF and  $u'_h$ , since all points tend to form a straight line. This shows that decreasing  $R_t$ , which is accompanied with a higher  $u'_h$ , results in finer wrinkling. The finer wrinkling folds more flame surface into the measurement volume, and this corresponds with the increase in turbulent flame speed.

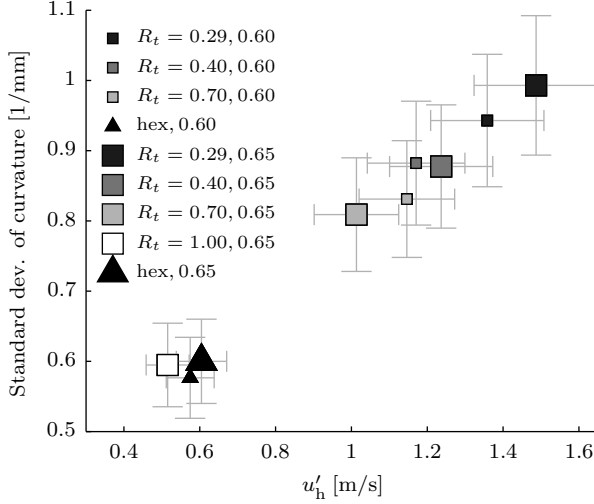
The increase in turbulence furthermore enables the flame front to vary more in downstream position, which is also illustrated by Figure 4.15a&b. Here the flame front of the fractal case spans a larger range in  $z$ -direction compared to the classical case. The increased wrinkling is therefore not necessarily accompanied by an increase in local flame surface density as also the flame brush thickness can be increased as shown in the previous section.

As there is no deviation of the linear trend in both  $\sigma_\kappa$  and  $S_{T,LC}$ , that would indicate some kind of saturation- or ‘bending’-behavior as denoted by [27], the question arises if an even more compact flame can be acquired by reducing  $R_t$  even further. However, this will require more precise methods to manufacture the smallest details of the grid.

#### 4.4.6 Emissions

In order to verify the low emission characteristic of the LSB, the  $\text{NO}_x$  and CO emissions are measured. To be able to measure species concentration in the exhaust gasses





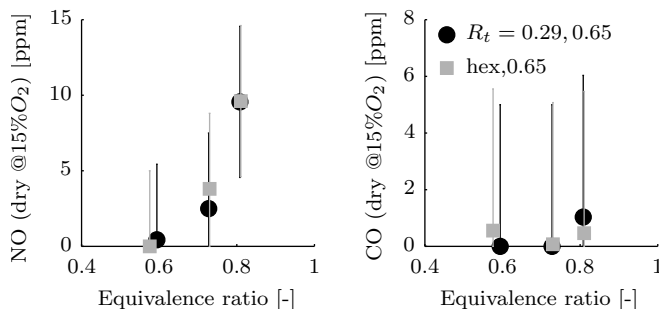
**Figure 4.16:** Standard deviation of the flame front curvature distribution as function of  $u'$  at the leading edge of the flame brush. The uncertainty in  $u'_{\text{hot}}$  is defined in Table 4.3. The uncertainty in  $\sigma_{\kappa}$  is estimated to be below 10%, as curvatures up to  $1.8 \text{ mm}^{-1}$  are measured with an accuracy better than 10%.

a combustion chamber is used to avoid entrainment of cold ambient air. This consists of a 0.5 m tube with inner radius of 150 mm. As this is more than three times the burner radius, it is expected that the enclosure has no effect on the combustion as was verified by Yegian and Cheng [107]. The exhaust gases are sampled at the centerline at the exit plane. The sample is cooled to  $4^{\circ}\text{C}$  to remove the water content and subsequently supplied to an Ecom-RBR mobile gas analyzer.

Only the results for the reference burner, i.e., classical hex at  $\sigma = 0.65$  and one fractal burner at  $R_t = 0.29$  and  $\sigma = 0.65$  are shown in Figure 4.17. There is no significant difference in  $\text{NO}_x$  and CO emissions between the burners. We therefore limited the emissions measurements to only one fractal grid and the hexagonal grid, which show the largest difference in turbulent flame speed. The values were compared with those of Littlejohn and Cheng [63], which show very similar emission characteristics. The  $\text{NO}_x$  emissions are low and an exponential-like dependence on the equivalence ratio is observed. In fact, the equivalence ratio affects the flame temperature which in turn affect the  $\text{NO}_x$  formation. For the CO emissions also a low level is observed. Replacing the conventional central blocking grid by a fractal grid does not compromise the low  $\text{NO}_x$  capabilities of the low-swirl burner.

## 4.5 Conclusions

The properties of turbulence generated with fractal grids are being studied extensively as can be seen by the large number of publications in the past few years. We investigated a practical application for fractal-grid-generated turbulence, i.e., the low-swirl burner. It is shown that replacing the traditional hexagonal grid by a fractal grid



**Figure 4.17:** NO and CO emissions as function of the equivalence ratio. The errorbars indicate the measurement uncertainty, which is  $\pm 5$  ppm.

leads to a higher turbulent flame speed.

The grids that were investigated are constructed according to an iterative pattern of crosses of decreasing length. The ratio of the thickness of the consecutive crosses, indicated by  $R_t$ , is varied between 1 and 0.23. The grid at  $R_t = 1$  is considered as a classical cross grid, since there is no multi-scale pattern and all grids with  $R_t < 1$  are denoted as fractal cross grids. Besides the cross grids also a classical hexagonal grid is used as a reference.

The properties of the turbulence downstream of various grids were measured by hot-wire anemometry. These measurements reveal that fractal grids effectively increase the turbulent intensity in the center region of a low-swirl burner. A doubling of  $u'$  and a four times higher TKE is observed while maintaining a similar pressure drop. In the situation where the grids are placed in a pipe flow, not only a similar increase in  $u'$  is observed, but here also a reduction in pressure drop is measured. For the grid at  $R_t = 0.7$  a maximal reduction of 35% compared to the classical case is observed. The energy spectra of the velocity measured just downstream of the exit of the pipe show that the enhancement applies to the whole range of turbulent scales. The increase in  $u'$  is not exclusively along the centerline. The measurements performed in an axial-radial plane show that  $u'$  is increased throughout the center region downstream of the central blocking grid of the low-swirl generator and up to the location of the flame ( $25 \text{ mm} < z < 125 \text{ mm}$ ).

The OH-LIF experiments allow for an evaluation of the FSD, flame brush thickness and the local consumption speed,  $S_{T,LC}$ . The increase in  $S_{T,LC}$  is linear in the level of turbulence at the leading edge of the flame front, which is in correspondence with literature [87]. This shows that the nature of the LSB appears unchanged by applying fractal grids, and only  $u'$  is increased. Although the direct measurement of the level of turbulence at the flame front is not possible by hot-wire anemometry, a reliable estimate has been made based on data of others [20].  $S_{T,LC}$  is determined by both the flame brush thickness and the flame surface density. The results as shown in Table 4.4 indicate that the increase in  $S_{T,LC}$  is more determined by the increase in the flame brush thickness than by the flame surface density, when switching from classical grids to fractal grids. The standard deviation of the flame front curvature distribution linearly increases with the level of turbulence at the leading edge of the flame front. This indicates that the flame front is finer wrinkled when it is exposed the more intense turbulence. Within the investigated range of  $u'$  there is no sign of a

deviation of this linear trend as well as from the linear trend for  $S_{T,LC}$ , suggesting that the flame front can be even finer wrinkled and that the flame speed can be enhanced more when increasing  $u'$  even further. It is left for further research to investigate higher  $u'$  by increasing the bulk velocity or by decreasing  $R_t$ .

With respect to the measurement volume the flame can be made more compact when employing fractal grids as more flame surface is folded into this measurement volume. However, this is associated with a wider flame brush. With respect to the cross-sectional throughput of reactants through the flame there is a solid increase as shown by  $S_{T,LC}$ . This provides means to increase the bulk velocity without blow-off and to achieve higher power densities in the same burner. Alternatively, one could exploit the efficient turbulence-generating property of the fractal grid to create similar levels of turbulence, but at lower expense of pressure drop.

Parameters of the fractal grids that were varied are the thickness ratio,  $R_t$ , and the blockage ratio of the grid,  $\sigma$ . The ratio of central- and swirling flow and thereby the strength of the linear decay of  $\bar{U}$  along the centerline downstream of the grid is mainly determined by  $\sigma$ , allowing control over the lift-off height of the flame. This effect was observed here as well. The flames involving a grid with  $\sigma = 0.65$  stabilized at a lower position than for the cases with a grid with  $\sigma = 0.60$ . There is no large difference in  $u'$  measured between the two different blockages.  $R_t$  mainly determines the increase in turbulence and combustion. When switching from a classical grid, either a hexagonal or cross grid, to the fractal grid at  $R_t = 0.7$  the largest difference in turbulence and combustion is observed. Here  $u'$  and  $S_{T,LC}$  both double. Decreasing  $R_t$  further to 0.4 and 0.29 slightly increases  $u'$ , and thereby marginally increases  $S_{T,LC}$ . The large difference in turbulence and combustion rate between the classical grids and the fractal grids at  $R_t = 0.7$  suggests that the flow is very sensitive to small alterations in the distribution of perforations in the grid. Therefore, it is interesting to further investigate the transition from classical to fractal by using grids with values of  $0.7 < R_t < 1$ . The fact that  $R_t$  and  $\sigma$  both have a more or less independent effect on the flame, i.e.,  $R_t$  controls turbulence intensity and  $\sigma$  the low-swirl stabilization mechanism, makes it convenient for engineering fractal grids for low-swirl combustion. Finally, it was verified that the low level of emissions for  $\text{NO}_x$  and also CO are not affected by changing to a fractal grid.

# Chapter 5

## Conclusions

In this chapter the conclusions of the individual chapters are summarized, which together provide an answer to the research question posed in the introduction (chapter 1). The first part of this chapter reviews to what extent it is possible to generate turbulence in an efficient way usable for low-swirl burners. The second part addresses the effect of the modified turbulence on the turbulent flame speed. Here, both the active grid and fractal grid approach are discussed separately. However, due to differences in blockage ratio and characteristic hole size between the two methods a direct comparison is omitted.

### 5.1 Methods to efficiently generate turbulence

#### 5.1.1 Active grid

A compact active grid was constructed, which introduces fluctuations into the turbulent flow at distinct and controllable frequencies without creating a large pulsation of the mean flow. This last property is a prerequisite for the usability of the active grid in a combustion context. Pulsation of the mean flow is undesired in, for example, gas turbines where it can lead to combustion instabilities [51]. The active grid consists of two perforated disks of which one is rotating, making it much less elaborate than the active grid of Makita [66] with multiple rotating parts. Four intrinsically different combinations of disks were tested in a pipe flow configuration.

The hot-wire results show an energy spectrum with a significant fraction of the energy in distinct, controllable peaks. The response, defined as the amount of energy contained in these peaks, is high (up to 25%) when the introduced scales have a timescale in the energy-containing range and decreases when these timescales are shorter and lie in the inertial range. This is in agreement with literature, e.g. [12, 15, 48, 49].

There was no indication of a ‘resonant enhancement’ for the current design and parameter range of the turbulent kinetic energy or dissipation rate, i.e., a maximum for the quantity concerned at a particular operating frequency of the grid. However, such behavior was observed by Cekli et al. [15] for the dissipation rate using an active grid in a wind-tunnel and by Cadot et al. [12] for the turbulent kinetic energy in their ‘French washing machine’. The current active grid operates at different, much lower

Reynolds numbers and does not display such a striking enhancement of turbulence in the available parameter range.

The active grid was found to introduce a significant amount of fluctuations into the flow. These fluctuations can be introduced between the large-scale, energy-containing range up to considerably smaller scales into the inertial subrange. To test whether these fluctuations directly enhance the combustion rate of the low-swirl flame the compact active grid is adapted such that it replaces the central blocking grid of a low-swirl burner. The hot-wire measurements in the center of the flow for this combination show very similar results as for the active grid in pipe flow in terms of the strength of the induced fluctuations. Evaluation of the mean velocity shows that the characteristic decrease in velocity with downstream distance is maintained. Furthermore, it is verified that a well stabilized low-swirl flame can be obtained.

### 5.1.2 Fractal grids

The fact that it is possible to use fractal grids to obtain higher turbulence levels in the wake of the grid, while maintaining a similar pressure drop is known from studies performed by others, e.g., [38, 92]. The experimental results reported here extend this knowledge on two main aspects. In chapter 3 the relation between the fractal-grid parameters and the turbulence is quantified in detail, while the results of chapter 4 demonstrate the usability of fractal grids in a low-swirl burner.

To identify the relation between the strength of the turbulence downstream a fractal grid and the parameters defining the grid, the flow downstream 24 different grids, containing variation in pattern, solidity and range of embedded scales, was examined. Two different fractal patterns were used, being the ‘square’ pattern as is widely reported in literature and the ‘cross’ pattern which was expected to be more suitable for low-swirl combustion. An image of these patterns can be found in Figure 3.1.

By increasing the range of embedded scales the turbulence was found to be intensified. An up to four times higher r.m.s. of the velocity fluctuations,  $u'$ , is observed when applying fractal grids instead of a classical grid with the same solidity. This is measured roughly three duct sizes downstream of the grid. Both grid types allow for a similar maximum enhancement. The difference lies in the inhomogeneity of the mean velocity in transversal direction. In case of the square grid there is a high velocity in the center, while there is a velocity deficit at this position for the cross grids. The level of inhomogeneity increases with blockage ratio and is also dependent on the range of lengthscales present in the grid.

The hot-wire results provide a good description of the turbulence intensity along the centerline for the various fractal grids. For the square grids the intensity first builds up and reaches a maximum whereafter it decreases. The development of the normalized turbulent intensity,  $I/I_{\text{peak}}$ , is self-similar with the downstream distance scaled by a ‘wake-interaction’ length,  $z^* = (L_0 - t_0)^2/t_0$ , where  $L_0$  is width of the largest rectangle and  $t_0$  the thickness of the bars forming the largest rectangle. This notion introduced by Mazellier and Vassilicos [68] is expanded by showing that the peak value,  $I_{\text{peak}}$ , behaves as a linear function of  $\sigma \frac{D}{z^*}$  which also agrees with data of others for much different grid sizes. Here,  $\sigma$  and  $D$  are the solidity of the grid and the duct size, respectively. Also for the cross grids the turbulence intensity along the centerline follows a self-similar dependence when the downstream distance is scaled

by the outer grid size. The absolute intensity scales linearly with  $t_0/D$ , which also holds for wind-tunnel data of Hurst and Vassilicos [38]. Being able to predict the turbulence intensity downstream various fractal grids is an important feature that can be used for designing fractal grids in practical applications.

The results discussed so far concern the measurements for the grids inside the square duct used in combination with a V-shaped flame (chapter 3). In chapter 4 we reported on the flow downstream cross grids placed in a pipe flow as well as in a low-swirl generator. Only the cross pattern is used here as it is preferred over the square pattern due to its velocity deficit instead of a velocity surplus in the center region. The otherwise high velocity along the centerline results in an improperly stabilized low-swirl flame. In the pipe flow configuration  $u'$  increased maximally by a factor 2.7 compared to using a single scale grid. An increase was observed for all fractal grids included in the study and illustrates a marked difference with the use of a classical single-scale grid. While  $u'$  is increased, the pressure drop over the grid is lower (15-35%), indicating that turbulence is more efficiently generated. The increase in turbulence is persistent when using the fractal cross grid in combination with the low-swirl generator. In this case a doubling of  $u'$  is observed at 3.5 grid sizes ( $L_0$ ), downstream, i.e., at the location where the flame is designed to stabilize. From the energy spectrum of the velocity it becomes clear that not only the largest scales are more energetic; also smaller scales are introduced as the spectrum is further extended into the high-frequency range.

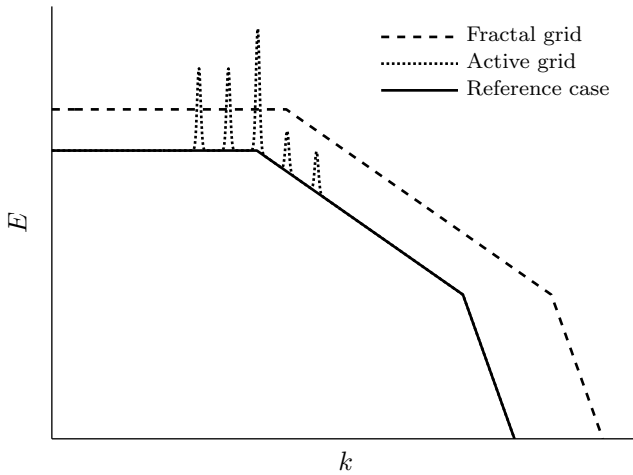
### 5.1.3 Summarizing the turbulence response

To summarize the results on achieving a more turbulent flow it can be stated that fractal grids provide an intense turbulence with an enhancement at all scales, while the active grid approach only increases the energy at specific scales. This is graphically depicted in Figure 5.1.

## 5.2 Enhancement of the turbulent flame speed

To evaluate whether the turbulent flame speed,  $S_T$ , is enhanced by generating turbulence using either an active or a fractal grid OH-LIF experiments have been performed. These experiments provide instantaneous cross sections of the flame front from which the amount of flame surface and subsequently the turbulent flame speed can be determined.

As there is no optimum operating frequency,  $f_r$ , identified for the active grid where  $u'$  is maximized, the most important question that remains is whether the specific scales introduced by the active grid provide a beneficial effect on the flame speed. For increasing  $f_r$  a decreasing  $u'$  is observed. For one of the active grid combinations (spiral-hex) this is accompanied with a decrease in turbulent flame speed, while for the other combination (chopper3) an almost constant value was observed. It was hypothesized that part of these fluctuations could be directly capable of wrinkling the flame front and thereby increase the combustion rate, but this has not been confirmed by the experimental results as the variation in turbulent flame speed is of the same order as the measurement uncertainty. The relative amount of energy in the specific fluctuations is most likely too low to induce a significant change in the



**Figure 5.1:** Schematic energy spectrum illustrating the distribution of the enhancement of different turbulence scales by active and fractal grids.  $E$  represents the energy per wave length and  $k$  represents the wave length, both in arbitrary units. While the active grid was found to introduce additional energy in specific peaks in the spectrum, the fractal grid induced an overall more intense turbulence, affecting both the large as well as the flame-wrinkling scales.

combustion rate. In contrast, Cardoso de Souza [14] obtains an increased combustion rate in simulations of a Bunsen flame using a spatial forcing scheme at the inflow of a turbulent jet configuration. However, the velocity fluctuations imposed close to the flame have an amplitude of at least 50% of the mean velocity and are applied for all three velocity components. Such forcing is considered to be much stronger than the active grid approach studied experimentally here.

A side effect of the deterministic periodic forcing is that it induces a periodic movement of the flame. Although the level of pulsation of the mean flow was found to be low, phaselock averaging of the OH-LIF data shows that at low  $f_r$  there is substantial movement of the flame (in the order of 10 mm). When  $f_r$  is increased this movement reduces. Such movement can lead to combustion instabilities when used inside an enclosure.

In two different configurations the effect of fractal-grid-generated turbulence on the turbulent flame speed is evaluated. The results of both studies provide qualitatively similar results. The results show clearly how the turbulent flame speed of the reference case, using a single scale grid, is increased by using multiple lengthscales in the grid. The relatively small geometrical alteration that exists between the classical cross grid ( $R_t = 1.0$ ) and the fractal cross grid with  $R_t = 0.7$  (the grid with the smallest range of different scales) already induces a strong increase in turbulent flame speed. The increase in flame speed is very well described by  $u'$  evaluated at the location of the flame. Infact, in the low-swirl context  $S_T$  increases linearly with  $u'$ . This linear dependence is characteristic for a low-swirl flame and has been confirmed by others to hold over a much larger range in  $u'$  than investigated here. While in most

of these studies, e.g., [20, 87, 88],  $u'$  is increased by using a higher mean velocity (and  $I$  remaining constant), here  $u'$  has been independently varied by using different fractal grids. In addition to the effect of fractal-grid-generated turbulence on the turbulent flame speed, it has also been verified that the low  $\text{NO}_x$  emissions, that are characteristic for a low-swirl burner, are not affected. When using a V-shaped flame the relation between the turbulent flame speed and the turbulent flow is quantitatively somewhat different, but also here  $S_T$  is mainly an increasing function of  $u'$ . At the position of the flame-stabilizing rod the wrinkling of the flame front is nil. In the time the flame front is convected downstream this wrinkling develops due to the turbulence and increases thereby the local turbulent flame speed. By incorporating this convection time,  $\tilde{t}$ , the increase in  $S_T$  for all measurement points, including the classical grids and the grids of two different fractal patterns, follow a consistent trend. This trend can be parameterized as a quadratic function in  $u'\tilde{t}/D$ . For the low-swirl flame the wrinkling of the flame front is considered to be steady in time and no such convection time is involved in determining  $S_T$ .

The relation between the grid parameters and the resulting turbulence, and subsequently, the relation between the turbulence and the turbulent flame speed obtained for a variety of grids for an academic V-shaped flame, as well as for a more realistic low-swirl flame will be of use in the design process when applying fractal grids in practical burners.

The study presented in this thesis clearly provides a positive answer to the question whether it is possible to increase the turbulent flame speed in a low-swirl burner by efficiently generated turbulence. The active grid approach appears to be of limited use as it does not introduce sufficient additional perturbations at the right scales. It leaves the question unanswered how to implement a ‘modulated forcing’, as successfully applied in simulations, in an actual low-swirl configuration. On the other hand, the fractal grid approach induces a strong increase of all turbulence scales leading to a direct increase of the turbulent flame speed. The increase in turbulence does not come at the expense of additional pressure drop.

## 5.3 Outlook

Several points are recommended for further investigation. One such point is the strong transition in turbulence intensity between the classical and slightly fractal cross grids. Expanding the current work with measurements in the range  $0.7 < R_T < 1.0$  can elucidate the sensitivity of the turbulence response to changes in the grid geometry.

A second point is that for the presented work only a single bulk velocity and equivalence ratio was used. Although the results provide conclusive information, the obtained trends could be further fortified by extending the current work with measurement at different equivalence ratios and bulk velocities.

A third and more practical point that can be addressed at this stage is the added value of the enhanced flame speed due to fractal-grid-generated turbulence. Due to the increased flame speed a higher specific power density is possible which is typically desired in gas-turbine application [60]. This fact itself implies a better usability of



low-swirl burners in gas turbines. However, it should be investigated how well the modified low-swirl burner deals with other typical gas-turbine difficulties.

- For example, the higher volumetric heat release rate may lead more easily to thermoacoustic instabilities as the temporal variation in heat release rate is one of the sources leading this phenomenon [85].
- Regarding a more sustainable future, it is expected that gas turbines will have to cope with different, less CO<sub>2</sub> intensive, fuels. Based on projects like ‘Power-to-Gas’ [106], to store the surplus of wind energy as hydrogen into the natural gas network, gas-turbine burners should be able to stabilize flames for fuels with a substantial fraction of hydrogen. As the high diffusivity of hydrogen leads to an increased turbulent flame speed [9] it is worthwhile to investigate whether the increase in turbulent flame speed due to fractal-grid-generated turbulence is maintained for such fuels.
- A third important issue is to be able to operate the gas turbine at part-load, which requires the stabilization of flames at low equivalence ratio [60]. In case the fractal-grid-generated turbulence lowers the minimum possible equivalence ratio to stabilize a low-swirl flame, it will greatly add to the applicability of fractal grids in such burners in practice.

# Bibliography

- [1] Natural gas 1998 issues and trends, Technical report, Energy Information Administration, **1999**. URL [http://www.eia.gov/pub/oil\\_gas/natural\\_gas/analysis\\_publications/natural\\_gas\\_1998\\_issues\\_trends/pdf/it98.pdf](http://www.eia.gov/pub/oil_gas/natural_gas/analysis_publications/natural_gas_1998_issues_trends/pdf/it98.pdf).
- [2] A. Abou El-Azm Aly, A. Chong, F.C.G.A. Nicolleau, and S.B.M. Beck, Experimental study of the pressure drop after fractal-shaped orifices in turbulent pipe flows, *Experimental Thermal and Fluid Science*, 34(1):104–111, **2010**. doi:10.1016/j.expthermflusci.2009.09.008.
- [3] R.A. Antonia, On estimating mean and instantaneous turbulent energy dissipation rates with hot wires, *Experimental Thermal and Fluid Science*, 27(2): 151–157, **2003**. doi:10.1016/s0894-1777(02)00259-5, 6th International Thermal Anemometry Symposium.
- [4] G.E. Ballachey and M.R. Johnson, Prediction of blowoff in a fully controllable low-swirl burner burning alternative fuels: Effects of burner geometry, swirl, and fuel composition, *Proceedings of the Combustion Institute*, 34(2):3193–3201, **2013**. doi:10.1016/j.proci.2012.05.095.
- [5] B. Bédard and R.K. Cheng, Experimental study of premixed flames in intense isotropic turbulence, *Combustion and Flame*, 100(3):485–494, **1995**. doi:10.1016/0010-2180(94)00138-I.
- [6] J.B. Bell, M.S. Day, J.F. Grcar, M.J. Lijewski, J.F. Driscoll, and S.A. Filatyev, Numerical simulation of a laboratory-scale turbulent slot flame, *Proceedings of the Combustion Institute*, 31(1):1299–1307, **2007**. doi:10.1016/j.proci.2006.07.186.
- [7] L. Biferale, A.S. Lanotte, and F. Toschi, Effects of forcing in three-dimensional turbulent flows, *Phys. Rev. Lett.*, 92:094503, **2004**. doi:10.1103/physrevlett.92.094503.
- [8] R.B. Bird, W.E. Stewart, and E.N. Lightfoot, *Transport Phenomena*. John Wiley & Sons, Inc, 605 Third Avenue, New York, NY, 2nd edition, **2002**. ISBN 0471364746.
- [9] E. Boschek, P. Griebel, and P. Jansohn, Fuel variability effects on turbulent, lean premixed flames at high pressures, volume 2, pages 373–382, **2007**. doi:10.1115/GT2007-27496.
- [10] H. Bruun, *Hot Wire Anemometry*. Oxford University Press, **1995**. ISBN 9780198563426.

## BIBLIOGRAPHY

- [11] P. Burattini, The effect of the X-wire probe resolution in measurements of isotropic turbulence, *Measurement Science and Technology*, 19(11):115405, **2008**. doi:10.1088/0957-0233/19/11/115405.
- [12] O. Cadot, J.H. Titon, and D. Bonn, Experimental observation of resonances in modulated turbulence, *Journal of Fluid Mechanics*, 485:161–170, **2003**. doi:10.1017/S0022112003004592.
- [13] J. Canny, A computational approach to edge detection, *Pattern Analysis and Machine Intelligence, IEEE Transactions on*, PAMI-8(6):679–698, **1986**. doi:10.1109/tpami.1986.4767851.
- [14] T. Cardoso de Souza, *Modulated Turbulence for Premixed Flames*, PhD thesis, Eindhoven University of Technology, **2014**. URL <http://repository.tue.nl/771731>.
- [15] H.E. Cekli, C. Tipton, and W. van de Water, Resonant enhancement of turbulent energy dissipation, *Physical Review Letters*, 105:044503, **2010**. doi:10.1103/PhysRevLett.105.044503.
- [16] C.K. Chan, K.S. Lau, W.K. Chin, and R.K. Cheng, Freely propagating open premixed turbulent flames stabilized by swirl, *Symposium (International) on Combustion*, 24(1):511–518, **1992**. doi:10.1016/S0082-0784(06)80065-2.
- [17] R.K. Cheng and H. Levinsky, *Lean Combustion: Technology and Control*, chapter 6 - Lean Premixed Burners, pages 161–177, Elsevier, Inc, **2008**. ISBN 978-0-12-370619-5. doi:10.1016/B978-012370619-5.50007-8.
- [18] R.K. Cheng, D. Yegian, M. Miyasato, G. Samuelsen, C. Benson, R. Pellizzari, and P. Loftus, Scaling and development of low-swirl burners for low-emission furnaces and boilers, *Proceedings of the Combustion Institute*, 28(1):1305–1313, **2000**. doi:10.1016/S0082-0784(00)80344-6.
- [19] R.K. Cheng, I. Shepherd, B. Bédard, and L. Talbot, Premixed turbulent flame structures in moderate and intense isotropic turbulence, *Combustion Science and Technology*, 174(1):29–59, **2002**. doi:10.1080/713712911.
- [20] R.K. Cheng, D. Littlejohn, W. Nazeer, and K. Smith, Laboratory studies of the flow field characteristics of low-swirl injectors for adaptation to fuel-flexible turbines, *Journal of Engineering for Gas Turbines and Power*, 130(2):021501, **2008**. doi:10.1115/1.2795786.
- [21] M.B. Chiekh, J.C. Béra, and M. Sunyach, Synthetic jet control for flows in a diffuser: vectoring, spreading and mixing enhancement, *Journal of Turbulence*, 4(32):1–12, **2012**. doi:10.1088/1468-5248/4/1/032.
- [22] C.J. Coffey, G.R. Hunt, R.E. Seoud, and J.C. Vassilicos, Mixing effectiveness of fractal grids for inline static mixers, Proof of concept report for the attention of Imperial Innovations, Imperial College London, **2007**.
- [23] G. Comte-Bellot and S. Corrsin, The use of a contraction to improve the isotropy of grid-generated turbulence, *Journal of Fluid Mechanics*, 25:657–682, **1966**. doi:10.1017/s0022112066000338.
- [24] W.J.A. Dahm and K.B. Southerland, Experimental assessment of Taylor’s hypothesis and its applicability to dissipation estimates in turbulent flows, *Physics*

- of Fluids*, 9(7):2101–2107, **1997**. doi:10.1063/1.869329.
- [25] M.S. Day, S. Tachibana, J.B. Bell, M. Lijewski, V. Beckner, and R.K. Cheng, A combined computational and experimental characterization of lean premixed turbulent low swirl laboratory flames: I. Methane flames, *Combustion and Flame*, 159(1):275–290, **2012**. doi:10.1016/j.combustflame.2011.06.016.
- [26] K. Döbbeling, J. Hellat, and H. Koch, 25 years of BBC/ABB/Alstom lean premix combustion technologies, *Journal of Engineering for Gas Turbines and Power*, 129(1):2–12, **2007**. doi:10.1115/1.2181183.
- [27] J.F. Driscoll, Turbulent premixed combustion: Flamelet structure and its effect on turbulent burning velocities, *Progress in Energy and Combustion Science*, 34(1):91–134, **2008**. doi:10.1016/j.pecs.2007.04.002.
- [28] A.C. Eckbreth, *Laser Diagnostics for Combustion Temperature and Species*, volume 3 of *Combustion Science and Technology Book Series*. Gordon and Breach Publishers, Amsterdam, The Netherlands, 2nd edition, **1996**. ISBN 90-5699-532-4.
- [29] M. Gad-el Hak and S. Corrsin, Measurements of the nearly isotropic turbulence behind a uniform jet grid, *Journal of Fluid Mechanics*, 62(1):115–143, **1974**.
- [30] P. Geipel, K.H.H. Goh, and R.P. Lindstedt, Fractal-generated turbulence in opposed jet flows, *Flow, Turbulence and Combustion*, 85(3-4):397–419, **2010**. doi:10.1007/s10494-010-9288-x.
- [31] A. Glezer and M. Amitay, Synthetic jets, *Annual Review of Fluid Mechanics*, 34(1):503–529, **2002**. doi:10.1146/annurev.fluid.34.090501.094913.
- [32] K.H.H. Goh, P. Geipel, F. Hampp, and R.P. Lindstedt, Flames in fractal grid generated turbulence, *Fluid Dynamics Research*, 45(6):061403, **2013**. doi:10.1088/0169-5983/45/6/061403.
- [33] R. Gomes-Fernandes, B. Ganapathisubramani, and J.C. Vassilicos, Particle image velocimetry study of fractal-generated turbulence, *Journal of Fluid Mechanics*, 711:306–336, **2012**. doi:10.1017/jfm.2012.394.
- [34] D. Goodwin. Cantera: An object-oriented software toolkit for chemical kinetics, thermodynamics, and transport processes, **October 2013**. URL <http://code.google.com/p/cantera>.
- [35] F. Halter, C. Chauveau, I. Gökalp, and D. Veynante, Analysis of flame surface density measurements in turbulent premixed combustion, *Combustion and Flame*, 156(3):657–664, **2009**. doi:10.1016/j.combustflame.2008.11.016.
- [36] E.R. Hawkes and J.H. Chen, Direct numerical simulation of hydrogen-enriched lean premixed methane-air flames, *Combustion and Flame*, 138(3):242–258, **2004**. doi:10.1016/j.combustflame.2004.04.010.
- [37] M. Hultmark and A.J. Smits, Temperature corrections for constant temperature and constant current hot-wire anemometers, *Measurement Science and Technology*, 21(10):105404, **2010**. doi:10.1088/0957-0233/21/10/105404.
- [38] D. Hurst and J.C. Vassilicos, Scalings and decay of fractal-generated turbulence, *Physics of Fluids*, 19:035103, **2007**. doi:10.1063/1.2676448.
- [39] I.E. Idelchik, *Handbook of Hydraulic Resistance*. Begell House, 4 edition, **2007**.

## BIBLIOGRAPHY

ISBN 9781567002515.

- [40] M.R. Johnson, D. Littlejohn, W. Nazeer, K. Smith, and R.K. Cheng, A comparison of the flowfields and emissions of high-swirl injectors and low-swirl injectors for lean premixed gas turbines, *Proceedings of the Combustion Institute*, 30(2): 2867–2874, **2005**. doi:10.1016/j.proci.2004.07.040.
- [41] H.S. Kang, S. Chester, and C. Meneveau, Decaying turbulence in an active-grid-generated flow and comparisons with large-eddy simulation, *Journal of Fluid Mechanics*, 480:129–160, **2003**. doi:10.1017/S0022112002003579.
- [42] H.S. Kang, D. Dennis, and C. Meneveau, Flow over fractals: Drag forces and near wakes, *Fractals*, 19(04):387–399, **2011**. doi:10.1142/s0218348x1100549x.
- [43] C.J. Keylock, K. Nishimura, M. Nemoto, and Y. Ito, The flow structure in the wake of a fractal fence and the absence of an inertial regime, *Environmental Fluid Mechanics*, 12(3):227–250, **2012**. doi:10.1007/s10652-011-9233-0.
- [44] A.L. Kistler and T. Vrebalovich, Grid turbulence at large reynolds numbers, *Journal of Fluid Mechanics*, 26:37–47, **1966**. doi:10.1017/s0022112066001071.
- [45] P.Å. Krogstad and P.A. Davidson, Freely decaying, homogeneous turbulence generated by multi-scale grids, *Journal of Fluid Mechanics*, 680:417–434, **2011**. doi:10.1017/jfm.2011.169.
- [46] P.Å. Krogstad and P.A. Davidson, Near-field investigation of turbulence produced by multi-scale grids, *Physics of Fluids*, 24(3):035103, **2012**. doi:10.1063/1.3693132.
- [47] A.K. Kuczaj and B.J. Geurts, Mixing in manipulated turbulence, *Journal of Turbulence*, 7(67), **2006**. doi:10.1080/14685240600827534.
- [48] A.K. Kuczaj, B.J. Geurts, and D. Lohse, Response maxima in time-modulated turbulence: Direct numerical simulations, *Europhysics Letters*, 73(6):851–857, **2006**. doi:10.1209/epl/i2005-10486-2.
- [49] A.K. Kuczaj, B.J. Geurts, D. Lohse, and W. van de Water, Turbulence modification by periodically modulated scale-dependent forcing, *Computers & Fluids*, 37(7):816–824, **2008**. doi:10.1016/j.compfluid.2007.01.012.
- [50] A.K. Kuczaj, B.J. Geurts, and W.D. McComb, Nonlocal modulation of the energy cascade in broadband-forced turbulence, *Phys. Rev. E*, 74:016306, **2006**. doi:10.1103/physreve.74.016306.
- [51] C. Külsheimer and H. Büchner, Combustion dynamics of turbulent swirling flames, *Combustion and Flame*, 131(1,2):70–84, **2002**. doi:10.1016/s0010-2180(02)00394-2.
- [52] S. Laizet and J.C. Vassilicos, DNS of fractal-generated turbulence, *Flow, Turbulence and Combustion*, 87:673–705, **2011**. doi:10.1007/s10494-011-9351-2.
- [53] S. Laizet and J.C. Vassilicos, Fractal space-scale unfolding mechanism for energy-efficient turbulent mixing, *Physical Review E*, 86:046302, **2012**. doi:10.1103/physreve.86.046302.
- [54] S. Laizet, V. Fortuné, E. Lamballais, and J.C. Vassilicos, Low Mach number prediction of the acoustic signature of fractal-generated turbulence, *International Journal of Heat and Fluid Flow*, 35:25–32, **2012**.

- doi:10.1016/j.ijheatfluidflow.2012.03.004.
- [55] J.V. Larssen and W.J. Devenport, On the generation of large-scale homogeneous turbulence, *Experiments in Fluids*, 50(5):1207–1223, **2011**. doi:10.1007/s00348-010-0974-1.
- [56] C.K. Law and C.J. Sung, Structure, aerodynamics, and geometry of premixed flamelets, *Progress in Energy and Combustion Science*, 26(4-6):459–505, **2000**. doi:10.1016/s0360-1285(00)00018-6.
- [57] C.J. Lawn and R.W. Schefer, Scaling of premixed turbulent flames in the corrugated regime, *Combustion and Flame*, 146(1-2):180–199, **2006**. doi:10.1016/j.combustflame.2006.03.010.
- [58] J.G. Lee and D.A. Santavicca, Experimental diagnostics for the study of combustion instabilities in lean premixed combustors, *Journal of Propulsion and Power*, 19(5):735–750, **2003**. doi:10.2514/2.6191.
- [59] T. Lee and R. Budwig, Two improved methods for low-speed hot-wire calibration, *Measurement Science and Technology*, 2(7):643–646, **1991**. doi:10.1088/0957-0233/2/7/011.
- [60] T.C. Lieuwen and V. Yang, *Gas Turbine Emissions*, Cambridge Aerospace Series. Cambridge University Press, **2013**. ISBN 9781107244245.
- [61] S.C. Ling and C.A. Wan, Decay of isotropic turbulence generated by a mechanically agitated grid, *Physics of Fluids*, 15(8):1363, **1972**. doi:10.1063/1.1694093.
- [62] A.N. Lipatnikov and J. Chomiak, Turbulent flame speed and thickness: phenomenology, evaluation, and application in multi-dimensional simulations, *Progress in Energy and Combustion Science*, 28(1):1–74, **2002**. doi:10.1016/s0360-1285(01)00007-7.
- [63] D. Littlejohn and R.K. Cheng, Fuel effects on a low-swirl injector for lean premixed gas turbines, *Proceedings of the Combustion Institute*, 31(2):3155–3162, **2007**. doi:10.1016/j.proci.2006.07.146.
- [64] D. Lohse, Periodically kicked turbulence, *Physical Review E*, 64(4):4946–4949, **2000**. doi:10.1103/PhysRevE.62.4946.
- [65] L.J. Lumley, Interpretation of time spectra measured in high-intensity shear flows, *Physics of Fluids*, 8(6):1056–1062, **1965**. doi:10.1063/1.1761355.
- [66] H. Makita, Realization of a large scale turbulence field in a small wind tunnel, *Fluid Dynamics Research*, 8(1-4):53–64, **1991**. doi:10.1016/0169-5983(91)90030-M.
- [67] B. Manshoor, F.C.G.A. Nicolleau, and S.B.M. Beck, The fractal flow conditioner for orifice plate flow meters, *Flow Measurement and Instrumentation*, 22(3):208–214, **2011**. doi:10.1016/j.flowmeasinst.2011.02.003.
- [68] N. Mazellier and J.C. Vassilicos, Turbulence without Richardson Kolmogorov cascade, *Physics of Fluids*, 22:075101, **2010**. doi:10.1063/1.3453708.
- [69] B. Mazzi, F. Okkels, and J.C. Vassilicos, A shell-model approach to fractal-induced turbulence, *The European Physical Journal B - Condensed Matter and Complex Systems*, 28(2):243–251, **2002**. doi:10.1140/epjb/e2002-00226-6.

## BIBLIOGRAPHY

- [70] P.A.J. van Melick and B.J. Geurts, Flow through a cylindrical pipe with a periodic array of fractal orifices, *Fluid Dynamics Research*, 45(6):061405, **2013**. doi:10.1088/0169-5983/45/6/061405.
- [71] L. Mydlarski and Z. Warhaft, On the onset of high-Reynolds-number grid-generated wind tunnel turbulence, *Journal of Fluid Mechanics*, 320:331–368, **1996**. doi:10.1017/S0022112096007562.
- [72] K. Nagata, H. Suzuki, Y. Sakai, T. Hayase, and T. Kubo, Direct numerical simulation of turbulence characteristics generated by fractal grids, *International Review of Physics*, 2(6), **2008**. URL [http://www.praiseworthyprize.org/latest\\_issues/IREPHY-latest/IREPHY\\_vol\\_2\\_n\\_6.html#Direct\\_Numerical\\_Simulation\\_of\\_Turbulence\\_Characteristics\\_Generated\\_by\\_Fractal\\_Grids](http://www.praiseworthyprize.org/latest_issues/IREPHY-latest/IREPHY_vol_2_n_6.html#Direct_Numerical_Simulation_of_Turbulence_Characteristics_Generated_by_Fractal_Grids).
- [73] K. Nagata, Y. Sakai, T. Inaba, H. Suzuki, O. Terashima, and H. Suzuki, Turbulence structure and turbulence kinetic energy transport in multiscale/fractal-generated turbulence, *Physics of Fluids*, 25(6):065102, **2013**. doi:10.1063/1.4811402.
- [74] J. Nedic, B. Ganapathisubramani, J.C. Vassilicos, J. Boree, L.E. Brizzi, and A. Spohn, Aeroacoustic performance of fractal spoilers, *AIAA Journal*, 50(12): 2695–2710, **2012**. doi:10.2514/1.J051387.
- [75] F.C.G.A. Nicolleau, S.M.M. Salim, and A.F. Nowakowski, Experimental study of a turbulent pipe flow through a fractal plate, *Journal of Turbulence*, 12, **2013**. doi:10.1080/14685248.2011.637046.
- [76] K.J. Nogenmyr, C. Fureby, X.S. Bai, P. Petersson, R. Collin, and M. Linne, Large eddy simulation and laser diagnostic studies on a low swirl stratified premixed flame, *Combustion and Flame*, 156(1):25–36, **2009**. doi:10.1016/j.combustflame.2008.06.014.
- [77] P.L. O’Neill, D. Nicolaidis, D. Honnery, and J. Soria, Autocorrelation functions and the determination of integral length with reference to experimental and numerical data, In *15th Australasian Fluid Mechanics Conference*. The University of Sydney, **2004**. URL <http://sydney.edu.au/engineering/aeromech/15afmc/proceedings/papers/AFMC00064.pdf>.
- [78] N. Otsu, A threshold selection method from gray-level histograms, *IEEE Trans Syst Man Cybern*, SMC-9(1):62–66, **1979**. doi:10.1109/TSMC.1979.4310076.
- [79] N. Peters, *Turbulent Combustion*. Cambridge University Press, **2004**. ISBN 0-521-66082-3.
- [80] T. Plessing, C. Kortschik, N. Peters, M.S. Mansour, and R.K. Cheng, Measurements of the turbulent burning velocity and the structure of premixed flames on a low-swirl burner, *Proceedings of the Combustion Institute*, 28(1):359–366, **2000**. doi:10.1016/S0082-0784(00)80231-3.
- [81] R.E.G. Poorte and A. Biesheuvel, Experiments on the motion of gas bubbles in turbulence generated by an active grid, *Journal of Fluid Mechanics*, 461: 127–154, **2002**.
- [82] S.B. Pope, *Turbulent Flows*. Cambridge University Press, **2006**.
- [83] D. Queiros-Conde and J.C. Vassilicos, *Turbulent wakes of 3D fractal grids*, chap-

- ter 9, pages 136–167, Cambridge University Press, **2001**. ISBN 9780521792219.
- [84] F. Ravelet, A. Chiffaudel, and F. Daviaud, Supercritical transition to turbulence in an inertially driven Von Kármán closed flow, *Journal of Fluid Mechanics*, 601: 339–364, **2008**. doi:10.1017/s0022112008000712.
- [85] Lord Rayleigh, The explanation of certain acoustical phenomena, *Nature*, 18 (455):319–321, **1878**. doi:10.1038/018319a0.
- [86] R.E. Seoud and J.C. Vassilicos, Dissipation and decay of fractal-generated turbulence, *Physics of Fluids*, 19(105108), **2007**. doi:10.1063/1.2795211.
- [87] I. Shepherd and R.K. Cheng, The burning rate of premixed flames in moderate and intense turbulence, *Combustion and Flame*, 127(3):2066–2075, **2001**. doi:10.1016/s0010-2180(01)00309-1.
- [88] I. Shepherd, R.K. Cheng, T. Plessing, C. Kortschik, and N. Peters, Premixed flame front structure in intense turbulence, *Proceedings of the Combustion Institute*, 29(2):1833–1840, **2002**. doi:10.1016/S1540-7489(02)80222-X.
- [89] S.S. Shy, E.I. Lee, N.W. Chang, and S.I. Yang, Direct and indirect measurements of flame surface density, orientation, and curvature for premixed turbulent combustion modeling in a cruciform burner, *Proceedings of the Combustion Institute*, 28(1):383–390, **2000**. doi:10.1016/s0082-0784(00)80234-9.
- [90] G.P. Smith, D.M. Golden, M. Frenklach, N.W. Moriarty, B. Eiteneer, M. Goldenberg, C.T. Bowman, R.K. Hanson, S. Song, J. William C. Gardiner, V.V. Lissianski, and Z. Qin. Gri-mech 3.0, **2014**. URL [http://www.me.berkeley.edu/gri\\_mech/](http://www.me.berkeley.edu/gri_mech/).
- [91] N. Soulopoulos, J. Kerl, F. Beyrau, Y. Hardalupas, A.M.K.P. Taylor, and J.C. Vassilicos, A turbulent premixed flame on fractal-grid generated turbulence, *Physics & Fluid Dynamics*, **2010**. URL <http://arxiv.org/abs/1004.2146/>.
- [92] N. Soulopoulos, J. Kerl, T. Sponfeldner, F. Beyrau, Y. Hardalupas, A.M.K.P. Taylor, and J.C. Vassilicos, Turbulent premixed flames on fractal-grid-generated turbulence, *Fluid Dynamics Research*, 45(6):061404, **2013**. doi:10.1088/0169-5983/45/6/061404.
- [93] T. Sponfeldner, S. Henkel, N. Soulopoulos, F. Beyrau, Y. Hardalupas, A.M.K.P. Taylor, and J.C. Vassilicos, A parametric study of the effect of fractal-grid generated turbulence on the structure of premixed flames, *European Combustion Meeting*, **2011**.
- [94] A. Staicu, B. Mazzi, J.C. Vassilicos, and W. van de Water, Turbulent wakes of fractal objects, *Phys. Rev. E*, 67:066306, **2003**. doi:10.1103/physreve.67.066306.
- [95] H. Suzuki, K. Nagata, Y. Sakai, and R. Ukai, High-Schmidt-number scalar transfer in regular and fractal grid turbulence, *Physica Scripta*, 2010(T142): 014069, **2010**. doi:10.1088/0031-8949/2010/T142/014069.
- [96] M.K. Swaminathan, G.W. Rankin, and K. Sridhar, Evaluation of the basic systems of equations for turbulence measurements using the Monte Carlo technique, *Journal of Fluid Mechanics*, 170:1–19, **1986**. doi:10.1017/S0022112086000782.
- [97] P.C. Valente and J.C. Vassilicos, The decay of turbulence generated by a



## BIBLIOGRAPHY

- class of multiscale grids, *Journal of Fluid Mechanics*, 687:300–340, **2011**. doi:10.1017/jfm.2011.353.
- [98] P.C. Valente and J.C. Vassilicos, Dependence of decaying homogeneous isotropic turbulence on inflow conditions, *Physics Letters A*, 376(4):510–514, **2012**. doi:10.1016/j.physleta.2011.11.040.
- [99] P.C. Valente and J.C. Vassilicos, Universal dissipation scaling for nonequilibrium turbulence, *Physical Review Letters*, 108(21):214503, **2012**. doi:10.1103/physrevlett.108.214503.
- [100] A.A. Verbeek, W. Jansen, G.G.M. Stoffels, and T.H. van der Meer, Improved flame front curvature measurements for noisy OH-LIF images, In *8th World Conferences on Experimental Heat Transfer, Fluid Mechanics and Thermodynamics*, **2013**. URL <http://purl.utwente.nl/publications/86288>.
- [101] A.A. Verbeek, R.C. Pos, G.G.M. Stoffels, B.J. Geurts, and T.H. van der Meer, A compact active grid for stirring pipe flow, *Experiments in Fluids*, 54(10):1594, **2013**. doi:10.1007/s00348-013-1594-3.
- [102] A.A. Verbeek, T.W.F.M. Bouten, G.G.M. Stoffels, B.J. Geurts, and T.H. van der Meer, Fractal turbulence enhancing low-swirl combustion, *Combustion and Flame (in press)*, **2014**. doi:10.1016/j.combustflame.2014.07.003.
- [103] D. Veynante, G. Lodato, P. Domingo, L. Vervisch, and E.R. Hawkes, Estimation of three-dimensional flame surface densities from planar images in turbulent premixed combustion, *Experiments in Fluids*, 49(1):267–278, **2010**. doi:10.1007/s00348-010-0851-y.
- [104] A. Warden. Fractal thinking. website, **retrieved on 11 october 2013**, [https://workspace.imperial.ac.uk/tmfc/Public/217-Christos\\_Vassilicos.pdf](https://workspace.imperial.ac.uk/tmfc/Public/217-Christos_Vassilicos.pdf).
- [105] P. Welch, The use of fast Fourier transform for the estimation of power spectra: A method based on time averaging over short, modified periodograms, *Audio and Electroacoustics, IEEE Transactions on*, 15(2):70–73, **1967**. doi:10.1109/tau.1967.1161901.
- [106] R. Winkler-Goldstein and A. Rastetter, Power to Gas: The final breakthrough for the hydrogen economy?, *Green*, 3(1):69–78, **2013**. doi:10.1515/green-2013-0001.
- [107] D. Yegian and R.K. Cheng, Development of a lean premixed low-swirl burner for low NOx practical applications, *Combustion Science and Technology*, 139(1):207–227, **1998**. doi:10.1080/00102209808952088.
- [108] H.W. Zheng, F.C.G.A. Nicolleau, and N. Qin, Assessment of des on the flow after a snow-flake orifice, In *Progress in Hybrid RANS-LES Modelling*, volume 111 of *Notes on Numerical Fluid Mechanics and Multidisciplinary Design*, pages 157–165, Springer Berlin Heidelberg, **2010**. ISBN 978-3-642-14167-6. doi:10.1007/978-3-642-14168-3\_13.

# Acknowledgement

At this point I would like to devote some words on the realization of this dissertation and to thank those who contributed to it either directly or indirectly.

While I was still working on my Master assignment there was a new research project in which a certain ‘strange’ turbulent flow phenomena would be employed to optimize combustion systems. I became enthusiasts because it consisted of an experimental and also a quite fundamental study in an interesting field; I could professionally play with fire. Therefore, I would like to thank Theo for offering me a PhD position in his group. Besides the interesting scientific research I was also happy to work in the ThW-group for its pleasant atmosphere. During my time in the group I enjoyed numerous activities and experienced that people find time to help each other. I think that Theo is to large extent responsible for this positive setting. If only because of spontaneously organizing ice-skating trips or the yearly diner at his residence.

Our weekly discussions together with Genie quickly lead to the development of a new experimental setup and the actual research could begin. During my PhD I received a lot of help from several Master students who I was able to make enthusiastic for the topic. First, Robbert assisted in building the setup and performed hot-wire measurements with the active grid. Then Willem came along and was occupied with the task of developing a post-processing method for the images Gerwin later on captured of the flame. To study alternative methods to generate turbulence Thijs started to experiment with fractal grids. As soon as it turned out that these grids were very helpful for combustion, the setup was expanded with a different burner geometry, which was the subject of Pieter’s Master assignment. About the results there were a lot of interesting discussions from which we both could benefit. It was good to be able to discuss the details of our work on a daily basis. I would very much like to thank all of these students for their valuable contributions to my PhD research and the pleasant cooperation.

During the four year there were several project meetings in which my colleague from Eindhoven, Thiago, and I presented our results. During these meetings Bernard always came up with critical questions, which made me scratch my head, but kept the research in the right direction. In the past year and a half we worked more closely together in order to write down the results. Tirelessly, he found time to carefully read my manuscripts and to provide me with helpful comments. Although he would probably be saying that it is just his job I would like to thank Bernard for his help and guidance.

Good colleagues are indispensable during a PhD. Either as sparring partner to solve scientific problem or as companion in a Friday afternoon experiment. I want to thank Marc and Timo for the including me in their enjoyable, messy and full

## ACKNOWLEDGEMENT

N213 office. We studied complex problems such as the travelling salesman problem or the optimal frequency to stimulate the Maizena-monster problem. We developed machines like a coffee grinder and an automated rotating grill for the ThW BBQ. Maybe not all as successful as they could have been, but these projects provided the necessary distraction from our PhD work. I am grateful that I ended up in an office with these two guys. After they left the group the gentlemen from the end of the hallway, Joost, Joris and Simon filled up the emptiness. Although I was the Nestor by then I had to succumb to their pressure and the office was rearranged and cleaned according to their standards. Luckily, by now things are settled and I enjoy their company and we have joyful and stimulating discussions.

I would like thank Henk-Jan for his assistance in the lab. I always found him willing to help me and to think along. I thank Genie for her help with setting up the laser-experiments and her input for the project. And I also thank Sally for the numerous times I asked her to help me.

My parent I would like to thank for always supporting me. They provided the environment in which I could grow up to become the person I am today and for which I am very grateful.

And last of all, Theuntje, most of thanks goes out to you for providing the most important. You make me happy and let me put things into perspective, and gave birth to our lovely daughter Guusje. When looking into her eyes, I realize there is no need to worry at all.

# Curriculum vitae

Anton Verbeek, born on June 12, 1985 in Zutphen, The Netherlands.

2014-current	Post-doc position in the Thermal Engineering group at University of Twente. <i>UP-THERM: Innovative high efficiency phase change fluid based heat engine</i>
2010-2014	PhD., Mechanical Engineering at University of Twente, Thermal Engineering group, PhD thesis: <i>Efficiently generated turbulence for an increased flame speed</i>
2006-2010	MSc., Mechanical Engineering at University of Twente, Thermal Engineering group, Master thesis title: <i>Synthesis gas production by Pulsed Compression Technology</i>
2003-2006	BSc., Mechanical Engineering at University of Twente

## Publications

- A.A. Verbeek, P.A. Willems, G.G.M. Stoffels, B.J. Geurts and T.H. van der Meer, Enhancement of turbulent flame speed of V-shaped flames in fractal-grid-generated turbulence (2014), *submitted to Combustion and Flame*.
- A.A. Verbeek, T.W.F.M. Bouten, G.G.M. Stoffels, B.J. Geurts and T.H. van der Meer, Fractal turbulence enhancing low-swirl combustion (2014), *Combustion and Flame (in press)*. doi:10.1016/j.combustflame.2014.07.003.
- A.A. Verbeek, R.C. Pos, G.G.M. Stoffels, B.J. Geurts and T.H. van der Meer, A compact active grid for stirring pipe flow (2013), in: *Experiments in Fluids*, 54:10(1594). doi:10.1007/s00348-013-1594-3.
- A.A. Verbeek, W. Jansen, G.G.M. Stoffels and T.H. van der Meer, Improved flame front curvature measurements for noisy OH-LIF images (2013), in: *8th World Conferences on Experimental Heat Transfer, Fluid Mechanics and Thermodynamics*, Lisbon, Portugal. URL <http://doc.utwente.nl/86288/>.

- A.A. Verbeek, R.C. Pos, G.G.M. Stoffels, B.J. Geurts and T.H. van der Meer, The Generation of Resonant Turbulence for a Premixed Burner (2012), in: *Engineering Turbulence Modelling and Measurements ETMM9*, Thessaloniki, Greece. URL <http://doc.utwente.nl/80622/>.
- T. Roestenberg, M.J. Glushenkov, A.E. Kronberg, A.A. Verbeek and T.H. van der Meer, Experimental study and simulation of syngas generation from methane in the Pulsed Compression Reactor (2011), in: *Fuel*, 90:2(1875-1883). doi:10.1016/j.fuel.2010.11.002
- A.A. Verbeek, G.G.M. Stoffels, R.J.M. Bastiaans and T.H. van der Meer, Optimization of Combustion in Gas Turbines by applying Resonant Turbulence (2011), in: *IGU Research Conference 2011*, Seoul, South Korea. URL <http://doc.utwente.nl/79377/>.
- A.A. Verbeek, R.C. Pos, G.G.M. Stoffels and T.H. van der Meer, Resonant Turbulence applied to a Low Swirl Burner (2011), in: *European Combustion Meeting 5*, Cardiff, UK. URL <http://doc.utwente.nl/77728/>.
- T. Roestenberg, M.J. Glushenkov, A.E. Kronberg, A.A. Verbeek and T.H. van der Meer, Partial Oxidation of Methane in the Pulsed Compression Reactor: Experiments and Simulation (2010), in: *World Academy of Science, Engineering and Technology*, 43(902). URL <http://doc.utwente.nl/89566/>.





